Adsorbents for Green Transportation

By

Nicholas R Stuckert

A dissertation submitted in partial fulfillment
of the requirements for the degree of
Doctor of Philosophy
(Chemical Engineering)
in the University of Michigan
2013

Doctoral Committee:

Professor Ralph T. Yang, Chair
Professor Erdogan Gulari
Professor Suljo Linic
Professor Xiaoqing Pan

Table of Contents

List of Figures

List of Tables

List of Appendices

Chapter 1: Characteristics of Hydrogen Storage by Spillover on Pt-doped Carbon and Catalyst-Bridged Metal Organic Framework

Introduction

Hydrogen spillover can be defined as the dissociative chemisorption of hydrogen on metal nanoparticles and subsequent migration of hydrogen atoms onto adjacent surfaces of a receptor via spillover and surface diffusion.[1-3] Evidence of atomic hydrogen spillover was first observed indirectly during studies of ethylene hydrogenation via heterogeneous catalysis.[4] Khoobiar reported room temperature formation of tungsten bronze upon exposure of the metal oxide to H_2 in the presence of alumina supported Pt.[5] The extensive work of Boudart and coworkers confirmed the effect with results obtained from hydrogen reduction of transition metal oxides mixed with Pt black[6] and studies of hydrogen uptake by transition metals on carbon supports.[7] Room temperature spillover for carbon supported Pt has been reported with evidence drawn from H_2 uptake and benzene hydrogenation experiments.[8] Recent studies have provided the direct evidence of atomic hydrogen spillover from Pt to carbon[9,10], from Pt to glass[11], and from Au nanoparticles to TiO_2 at room temperatures.[12]

To induce hydrogen spillover, two methods are commonly applied. One is direct doping of dissociation sources on the adsorbent. By using this method, various dissociation metals (Pt, Pd, Ru and Ni) have been successfully doped on the carbon and MOF supports, and enhanced storage capacities have been observed on the doped samples.[13-30] The other method is building bridges between the dissociation source and the adsorbent. Since the early discovery of the hydrogen spillover phenomenon, the enhancement effects of "bridges" were also observed. The known bridge molecules included water[31-33] and polynuclear aromatic hydrocarbons (e.g., perylene).[34] Although the bridging effects are not well understood, they have been exploited in the development of sorbents for hydrogen storage at ambient temperature,[35-37] and significant enhancements have been reported on the bridged-MOFs.[35-39] To date, over 30 different groups worldwide have reported in the literature significant enhancements in hydrogen storage by

spillover. Recently, there have been questions raised recently about the reproducibility of these results. While these results were obtained at a time before I was aware of the questioning it is important to point out that the hydrogen storage capacity is not relevant to whether or not spillover is occurring at room temperature. This work attempts to identify the question of how hydrogen spillover is occurring at room temperature, if it is occurring at all. Hydrogen adsorption measurements are used to compare larger adsorption for observed TPD peaks with larger adsorption, however this is supporting information and is likely not statistically significant.

Additionally I characterize the adsorption sites of Pt/C using temperature programmed desorption (TPD). Extensive research in the catalysis field has been devoted to understanding the dissociation of hydrogen using Pt and subsequent spillover.[40,41] Theoretical studies have recently identified steps, edges and the high energy Pt(110) surface as being the ideal locations for hydrogen dissociation.[40-43] These have been shown to have faster rates and predicted bonding energies lower than the activation energy of the rate-limiting step for spillover, as determined earlier.[44] Further studies have shown that the growth of Pt nanoparticles corresponds directly with the growth of (111) and (100) faces and loss of higher energy sites, which is to be avoided.[45] All of these studies can potentially lead to significant reductions in amount of platinum needed to perform fuel cell oxidation of hydrogen and potentially reduce the energy lost in fuel cell operation by serving as a secondary step between hydrogen release from hydrides and then use in the oxidation reaction. This work then significantly increases our understanding of this mechanism for the role of ultimately helping our understanding of hydrogen spillover at room temperature.

Experimental Section

Synthesis of Pt/AX-21. The superactivated carbon AX-21 (BET surface area = 2880 m^2/g) was obtained from Anderson Development Company. AX-21 was dried by degassing in vacuo at 393 K for 12 h before doping. There are a number of techniques for metal doping; the most common, the incipient wetness method, is used in this work.

Typically, the synthesis of 6 wt % Pt/AX-21 includes the following steps: (1) 200 mg of well-dried AX-21 carbon was dispersed in 20 mL of acetone and was stirred for 0.5 h in a 125 mL

Erlenmeyer flask at room temperature. A 2 mL acetone solution containing 26 mg H_2PtCl_6 (Aldrich, 99.9%) was added drop wise to the above solution (*very slowly*, *over at least 10 min*); (2) The Erlenmeyer flask containing the slurry was subjected to ultrasonication (100 W, 42 kHz) at room temperature for 1 h and was then magnetically stirred at room temperature for 24 h; (3) After being dried in an oven at 323 K overnight to evaporate most of the acetone solvent, the impregnated carbon sample was transferred to a quartz boat and placed in a horizontal quartz tube. The sample was further dried in He flow at 393 K for 2 h to remove the residual acetone and also the moisture adsorbed on the sample. The He flow was then switched to H_2 and the temperature was increased to 573 K at a heating rate of 1 K /min and held at 573 K for 2 h; (4) After slowly cooling to room temperature in H_2, the sample was purged with flowing He (for sample "passivation") for at least 5 h and was stored under He atmosphere before further measurements; (5) Prior to measurements, the sample was degassed in vacuum at 623 K for 12 h. The resulting Pt/AX-21 sample had a BET surface area of 2518 m^2/g, and uniformly dispersed Pt nanoparticles with 1-3 nm diameters.

The effects on spillover of commonly encountered deviations in sample preparation and measurements were studied in this work. These included:

1. Investigating the effects of the rate of drop wise addition of the H_2PtCl_6 solution into the AX-21/acetone slurry, during step (1), by adding the H_2PtCl_6 solution to the slurry of AX-21 with three different rates (1 min, 5 min, 10 min).

2. Investigating the passivation effects of He in step (4), after H_2 reduction at 573 K for 5 hours, by adjusting lengths of time (0, 0.5 and 5 hours) the sample was passivated in He flow at 20 cm^3/min.

3. Investigating the Pt particle size effects, by treating the as-synthesized Pt/AX-21 in He flow at 873 K for 60 hours to induce sintering of Pt particles to enlarge their sizes.

Synthesis of IRMOF-8. IRMOF-8 was synthesized according to the method of Huang et al.[46] (1) $Zn(NO_3)_2x6H_2O$ (1.19 g, 4 mmol, *freshly opened*) and 2,6-naphtalenedicarboxylic acid (0.43 g, 2 mmol, purchased from Aldrich) were dissolved in 40 ml of dimethylformamide (DMF) during vigorous stirring at room temperature; (2) Three drops of H_2O_2 aqueous solution (30 wt %) were added to the solution. Triethylamine (2.3 ml) was slowly added drop wise to the above solution

under vigorous agitation for 1 h; (3) The white product was collected by repeated filtering, and three thorough washings with DMF. The sample was degassed first at room temperature for 6 h, then heated to 453 K at a heating rate of 1 K/min and held at that temperature for 12 h, all under vacuum.

Preparation of Bridged Samples. (1) IRMOF-8 (200 mg), 5 wt % Pt/AC catalyst (25 mg), and sucrose (33.2 mg) were ground together with mortar and pestle for 1 h (to induce thorough mixing). (2) This mixture was transferred to a quartz boat that was placed in a tubular reactor. The mixture was heated in flowing helium (100 mL/min) at a heating rate of 1 K/min to 473 K and held at this temperature for 3 h (above the melting point of sucrose at 459 K). It is noted that the sample was piled in the quartz boat – not as a thin layer. (3) Subsequently the temperature was increased at 1 K /min to 523 K and held at 523 K for 12 h. The material was cooled to room temperature at 1 K /min in flowing helium. (4) The samples were stored in vacuum before being moved into the sample holder for high-pressure measurements. (5) Prior to measurements, the samples were degassed in vacuum at 473 K for 24 h.

Temperature Programmed Desorption (TPD). Initially a sample was degassed at 623 K for 8-48 hours until the pressure in the system was lower than 10^{-6} torr and contaminants (other than water and hydrogen) totaled less than 10^{-9} torr partial pressure; verified using a mass spectrometer. The sample was then cooled to either 298 K or 77 K and dosed with an equal mixture of D_2 and H_2. Exposure pressure was varied from 150 torr to 16 atm which encompasses the range of predominate adsorption by the metal particles to predominate adsorption by the carbon support. After a predetermined amount of time ranging from 30 seconds to 40 minutes the sample was quenched in liquid nitrogen. The system was then slowly degassed until the pressure in the system was lower than 10^{-6} torr and hydrogen levels were at background. Heating was then performed at 10 K/min from 77 K to 573 K, while the mass spectrometer analyzed m/z ratios from 1-6. Additionally experiments were done to reproduce and verify more accurately the results of Lachawiec and Yang[47] published earlier by following the same TPD procedure stated therein.

Isotopic Hydrogen Equilibrium. In order to differentiate hydrogen dissociation from adsorption, the equilibrium conversion was taken as a function of time over a sample exposed

to an equal mix of H_2 and D_2 at 16 atm. This high pressure was chosen due to the slow nature of adsorption (~40 minutes) and the slow dissociation that was easily measurable. The Pt/AX21 was degassed for 8 hours at 623 K before being exposed at 298 K to a mixture of hydrogen and deuterium that had equilibrated for 2 hours. The sample was then quenched in liquid N_2 at 77 K and the gas was sampled using a mass spectrometer. H_2, HD and D_2 were measured as a function of their concentration over time and their ratios gave the fraction of equilibration of the reaction, K_{eq} is ~3.5. Samples of the Pt/AX21 sample cooled to 77K prior to exposure, blank stainless steel tube, and degassed AX21 were measured as well.

Results and Discussion

Spillover on Pt-doped Carbon. In previous work[36], this group has shown that the storage capacity of AX-21 at room temperature and 10 MPa was enhanced to 1.2 wt % by doping with nanosized Pt metals (~ 2 nm). This represents an enhancement factor of 2. During the optimization of the storage capacity of Pt-doped AX-21, the following factors were investigated.

Catalyst Size Effect. In the synthesis procedure, the H_2PtCl_6 was dissolved in an acetone solution and then added to the slurry of AX-21 (see experimental section). It was found that the addition rate of H_2PtCl_6 into the slurry of AX-21 directly affected the dispersion of Pt metal on AX-21 and in turn the measured storage capacity of the doped sample. Figure 1 shows the hydrogen isotherms of three samples of Pt/AX-21 prepared by adding H_2PtCl_6 solution to AX-21 with three different rates, (1 min, 5 min, and 10 min). The storage capacities of Pt/AX-21 were affected by the addition or mixing rates of H_2PtCl_6 solution to AX-21 and ranged from no spillover observation (1 min) to full enhancement (10 min), which has a storage capacity of ~1.2 wt % at 10 MPa and 298 K. TEM results (see supporting information) showed the distribution of Pt metals was not even and particle sizes as large as 20 nm could be seen when the Pt solution was added to AX-21 quickly. Aggregates of over 120 nm were also shown to be prevalent. The particle size was reduced to 3 nm when the addition rate of Pt solution to AX-21 was decreased and aggregates diminished substantially. The slowest addition rate resulted in Pt particles as small as 1 nm (Figure 2) with extremely rare aggregation sites. These results indicated that slow addition rates favor the doping of Pt with small sizes and even dispersion. The slow addition of H_2PtCl_6 enables the carbon particles to have an even chance to interact and adsorb the Pt

precursor ions, thus leading to a high dispersion. The hydrogen storage capacities of the three samples indicate that uniform dispersion and small Pt particle size enhance spillover. Personal review of this data showed that the enhancement was due to an increase in helium displacement volume. In addition, three replicates of Pt/AX-21 samples prepared by Lifeng Wang had storage capacities that varied between a reported 1.14-1.23 wt %, showing the reproducibility of this method. Personal experience has shown that the instruments are not capable of this level of accuracy and most likely these values were exaggerated.

To isolate the Pt size effects on the storage capacity, a Pt/AX-21 sample with a measured storage capacity of 1.2 wt % was treated in helium atmosphere at 873 K to sinter the Pt nanoparticles. As shown in Figure 3, after sintering at 873 K for 60 h, the storage capacity of the Pt/AX-21 was reduced to 0.8 wt %. The treatment at 873 K resulted in severe sintering of Pt particles and the sizes of Pt particles range from several to tens of nanometers (Figure 4). These results indicate that the smaller Pt size shows a correlation to hydrogen storage capacity; however this is still outside statistical significance. If this is not coincidental, then the most obvious cause would be through effective utilization of the heavy Pt. Since radius linearly decreases the mass to surface area ratio, larger particles will be increasingly less effective, taking up more mass than needed. Another previously published work[47] shows that there is a limited area of influence for each particle due to diffusion resistance and lack of diffusion pathways. Thus particles with lower uneven dispersion do not affect the entire carbon support, and full spillover enhancement is not realized.

It is noted that these observations are also in agreement with previous studies. Tsao et al. found that impregnated Pt nanoparticles of ~1-2 nm in activated carbon can effectively enhance the hydrogen spillover effect and an enhancement factor of 3 was achieved.[20] Arenillas and coworkers measured the hydrogen adsorption on carbon nanospheres doped with different loadings of Ni and found that the storage capacity of doped carbon was enhanced by a factor of 1.4 to 2.3 when compared with the undoped carbon.[21] Carbon doped with 5 wt % Ni had the best nickel distribution and the highest storage capacity.[20] Catalyst size effects were also observed on Pd-doped carbon nanofibers. Sandi et al. reported that the storage capacity of Pd-doped carbon nanofibers was 4 times larger than the un-doped carbon and attributed the

enhancement to smaller Pd particle and the high Pd surface area.[21] Significant enhancement in hydrogen storage at room temperature was also observed on templated carbon after doping homogeneously with nanoparticles of Pd (2 nm in size).[49]

Ultrasound Effects. Ultrasound treatment was applied to optimize the Pt/AX-21. The main phenomena responsible for ultrasound actions are cavitations and acoustic streaming, although this phenomenon is not well understood. During the impregnation of metal particles, ultrasound helps to create more intimate contacts between the particles and the substrate.[50] During sonication of the impregnation slurry, a polyethylene bag is suggested.[47] The polyethylene bag possibly decreases the sonic wave attenuation that occurs when using laboratory glassware.

Passivation. After H_2 reduction at 573 K for 2 hours, the sample is "passivated" in flowing He for 5 hours. Upon exposure of the sample to the ambient air, a sample not passivated reacts vigorously, marked by sparks/glowing, which degrade the sample. Hydrogen isotherms showed equivalent storage capacity for non-passivated samples as AX-21. Helium flow time results were inconsistent with some samples completely passivated at 1 hour and others requiring 5 hours. The only trend observed was the visual cue of sparking and glowing, which occurred and sintered the sample, or did not occur and the sample showed an even dispersion. Isotherms for these samples are presented in the supporting information.

Sample Pretreatment. Prior to isotherm measurements, the Pt/AX-21 samples are reduced in H_2 at 573 K. Evacuation at 623 K (for 12 hours) was found to be adequate in our work. This is potentially due to full cleaning of the platinum and carbon surface, however residual pressure of the sample could not be measured. Pretreatment at 573 K may not be adequate (as in Stadie et al.).[51]

All the factors above are crucial for achieving high platinum dispersions and therefore potentially spillover. The missteps and pitfalls in sample preparation and treatment will lead to diminished or no spillover effects. These missteps have all been identified from members of our laboratory, which I have learned over time not to commit. In the published literature, a case in point is the recent work of Stadie et al.[51] They used overly concentrated Pt precursor solution combined with overly rapid mixing of the solution with the carbon slurry. This led to poor metal

dispersion in the sample (large Pt particle sizes and the very low isotherm knee below 1 atm pressure, shown in their Fig. 4 inset). As shown in this work, their use of excessive amounts of metal (12 wt %), short passivation times in flowing helium, and the low pretreatment degassing temperature (573 K) all diminished dispersion and any observable effects. These significant deviations in processes should account for their observation of essentially no spillover effects; as would be expected as this has happened by mistake in our laboratory. In addition, the work performed by Stadie et al.[51] had relatively large dead volumes (total volume of 50-80 mL compared with ~12mL in systems used in this work) and high leak rates (compared to the systems used in this work). All issues contribute to decreased measurement sensitivities and potentially increased errors that also could account for the significant differences in reported spillover results. In experiments it is best to halve the sample and measure it again to verify there were no leaks or other instrumental errors. I have been assured this has happened in our laboratory, and for the data provided by Lifeng Wang.

Spillover Observation. The interest in TPD spectra comes from the distinct peaks in temperature that different adsorption sites show.[48,52,53] The behavior of the peaks during different adsorption and desorption conditions also makes them unique from other peaks as well as providing details on their order and activation energy.[48,52,53] When the surface coverage of a given site increases, the peak will shift lower in temperature if the order is greater than one.[48] If the order is one then it will stay at the same location.[48] On complex mixes the peaks from TPD spectra can be compared with published TPD spectra, which gives a relatively good indication of what adsorption sites are prevalent. In the case of crystalline metals this data can be used to determine which faces or edges are prevalent.[48,52,53] In this wok, the TPD results show four distinct peaks between 120 K and 573 K, at least one of which appears hidden under any conditions (a blank of the AX-21 shows no peaks from 120 K - 573 K). While these peaks could be due to small variations in heating rate, the temperature profile, taken independently of the temperature controller, indicated a smooth heating rate and repeat tests confirmed that these peaks are reproducible under specific sets of conditions.

We attempted to initially isolate the Pt metal peaks by varying the adsorption temperature. At 77 K no spillover is known to occur,[9,10] thus the peaks I observed were assigned to Pt. With

the increase in temperature I see the growth of the first spillover (carbon based) peak shown in Figure 5. At 298 K a secondary spillover (carbon based) peak can be observed at a much higher temperature. Comparing the Pt peaks with literature[48,52,53] the initial conclusion is that the peaks correspond to the (110) face but with some uncertainty (it is also important to note that the (110) face has similar TPD peak temperatures and behaviors as edges and steps). [43] On a Pt (110) surface there are two known adsorption sites β_1 and β_2.[48] The β_1 site is of higher order kinetics and the β_2 site is of first order kinetics (seen by the shift in the β_1 peak over surface concentration change).[48] These characteristics are indicated in this wok as well. From Figure 5 the β_1 appears to move to lower temperatures as the coverage increases, indicating a higher order rate and β_2 appears stable, indicating a first order rate. Additional verification can be shown in Figure 6 by using a varying exposure of hydrogen pressure. At 150 torr little spillover is seen. The β_2 peak shows no shift in position while the β_1 lowers in temperature slightly with increasing pressure showing possible higher order kinetics. Unfortunately this system used much higher hydrogen exposure conditions than previous woks[48] and I cannot verify that the peaks are not already saturated at this point. However, I show that there are two Pt peaks that are at the same temperature and have similar characteristics as those from the (110) face. Most importantly, there are clear peaks for Pt adsorption different than carbon and that these peaks are similar to highly uncoordinated Pt, rather than stable low-energy surfaces. These uncoordinated sites are assumed to come from the small Pt nanoparticles that have them in significantly higher fractions than larger nanoparticles.

At this point, the β_2 and carbon peaks are still somewhat indistinguishable. To make sure the β_2 and carbon peaks are in fact different, Figure 7 shows the effects of varying H2 exposure time. While the β_1 peak is obscured throughout, the rise of the C peaks independent of the β_2 peak is clear, thus confirming the existence of all four independent peaks. Since the peaks called β_1 and β_2 align more closely with previously reported data for (110) than the (111), [52,53] (100) [53] or partially oxygenated variants[52,53] it appears the (110) face is the only active face for these nanoparticles. The possible explanations for the phenomena include masking of faces by binding to carbon, evolving gasses from the carbon or possibly significantly higher absorbance of hydrogen on the uncoordinated sites. However, TEM in Figure 2 shows the prevalence of the

(111) face and also in a slightly higher amount. Under these conditions almost full saturation of all Pt surfaces occurs.[48,52-55] Thus I assume there is an underlying cause for the lack of observation of (111) and (100) surface peaks that I are unable to explain.

In order to provide more definite evidence of reverse spillover previously proposed by this group[41] I reproduced our previous study using a sequential D_2/H_2 dosing experiment. The species were again found to desorb in the reverse order, with the inclusion of HD in between as shown in Figure 8. The formation of HD and presence in the second carbon peak shows that D_2 also spilt over and mixed with the adsorbed H_2, and clearly indicates that these adsorbents have catalytically activated adsorption sites. The reverse dosing procedure (D_2 then H_2) was not done but was published earlier.[47]

The carbon peaks observed are characterized by their isotopic susceptibility and independence from the Pt peaks as shown in Figure 5. Figure 5 also shows they do not occur for low temperature adsorption corresponding to trends previously observed by spillover.[9,47] The observation reported here closely aligns with other forms of direct observation of spillover.[10] Mitchell observed a very slow diffusion limited step that can take days to fully saturate the carbon support.[10] Published simulations show that H_2 dissociation and subsequent spillover from the Pt to the carbon occur quickly and the hopping from one adsorption site to another is the rate limiting step.[54] Other simulations show a strong preference for hydrogen dissociation at higher energy sites (edges, steps and (110) faces) [40-43], which correlates with what is observed here.

Catalysis of Hydrogen Isotopic Equilibrium vs. Adsorption. The time dependent measurement of the dissociation recombination reaction on Pt/C was measured and found to proceed very fast at the conditions stated above. This was compared to total uptake rates and was found that the rate of hydrogen dissociation and recombination (HDR) was equivalent to the rate for adsorption equilibrium (Li et al. [44]) as shown in Figure 9. However adsorption requires only 0.5% of the gas in the sample cell to reach completion while the HDR requires mixing with all the gas. Since the HDR step interacted with the equivalent amount as needed by adsorption in only a few minutes I observe that hydrogen dissociation is most likely not the rate limiting step.

Spillover on Catalyst-bridged MOF. Hydrogen spillover to MOFs can be achieved by building nanosized carbon bridges to a H_2 dissociation catalyst (Pt/C), or by direct doping of a dissociation metal. Spillover enhancement has also been seen by embedding nanoparticles of Pd (~2 nm) in MIL-100(Al) and Redox-Active MOFs and Pt on MOF-5.[28-30] By using these methods, enhanced storage capacities on MOFs via spillover have been observed near room temperature. However, it is noted that consistency of spillover storage on the bridged MOF samples is very difficult to achieve due to the empirical nature of bridge building. As shown in Figure 10, the storage capacity of the bridged IRMOF-8 varies from sample to sample, which is due to the different particle connectivities among each sample, and how thoroughly the catalyst and MOF particles are mixed (see 3.2.2.). The key factors in sample preparation that affect storage capacity are discussed below.

The theoretical saturation spillover storage capacities for different MOFs and COF-1 were calculated by Ganz and coworkers[55] using accurate *ab initio* quantum chemistry calculations (details given by Ganz and coworkers[55]). Their results show the theoretical capacities of 4.5wt% for IRMOF-1, 5.7 wt% for IRMOF-15 and IRMOF-16 (while IRMOF-8 was not included in their calculations). These results indicate that there is room for further optimization in sample synthesis.

MOF Quality and Particle Sizes. During our experiment, it is found that the starting zinc nitrate material affected the MOF quality. As shown in Figure 11, by using a freshly opened zinc nitrate, the surface area of IRMOF-8 was 620 m^2/g. By using the zinc nitrate after being opened for 1 month, the surface area of IRMOF-8 was reduced to 320 m^2/g. This was possibly due to the partial hydrolysis of zinc nitrate, the moisture of which could destroy the MOF structure. Huang et al.[46] also observed that the zinc nitrate shelved for a long time resulted in nonporous unknown phase.

For connecting the catalyst (Pt/C) and MOF, compatibility of particles sizes is important. Lifeng Wang synthesized the IRMOF-8 by using the direct mixing method (with H_2O_2 addition) as reported by Huang et al. [46] Triethylamine was used to deprotonate the acid to initiate fast polymerization. The fast polymerization resulted in the generation of a large amount of crystal nuclei in a short time. It was observed that the white product of IRMOF-8 appeared within 10

minutes after adding the triethylamine. These crystal nuclei grew into MOF particles of 100-200 nm in size, which is comparable to the size of the catalyst particles. (The MOF prepared without H_2O_2 addition would in fact yield a different material with smaller particle sizes.) It is noted and preferred that this size is much smaller than the large crystals (mm size) that were formed slowly by the solvothermal method (Rosi et al). [56] It is believed the significant spillover effect would not be observed if the large MOF crystals were used as extrapolated from the previous study with MOF-177[57]. This is logical since the nanosized MOF has more external surface area and more contacts with the dissociation source. Also, grinding the large particles of MOFs into small particles is a successful method that increases the external surface area of MOFs. Another, ball-mill, is a particularly good method to achieve this, but was difficult to reproduce. However, successful bridging results by ball-mill have been reported by Liu group and Tsao group.[37-39] It is noted that the external surface area of nanosized MOFs (100 nm) is 10^8 times that of micrometer sized MOFs (1 mm). This has a limit though, as very small particles are also not desired, with large differences in the particle sizes, the smaller particles tend to agglomerate leading to poor mixing.

Uniform Mixing and Optimized MOF/Catalyst/Sucrose Ratio. Uniform mixing of the three components Pt/C, sucrose and MOF is necessary for spillover of hydrogen and in turn enhanced storage capacity. This step was necessary to produce evenly distributed carbon precursors between the Pt/AC and MOF particles. Lifeng Wang used a mortar and pestle to thoroughly mix and form intimate contacts between the three-components. The ideal situation is where all the individual Pt/C and MOF particles are “bridged” with sucrose. Distribution differences between the three constituents after mixing may result in different connectivities between the particles and would account for some of the irreproducibility in the storage capacity results (as shown in Figure 10). According to lab experience, gentle mixing actions are preferred, while strong grinding actions lead to partial collapse of the MOF structure (observed by lowered BET surface area). Powered sucrose rather than crystalline sucrose is suggested before the mixing step. While Lifeng Wang was not able to perform this step under an inert atmosphere, it is suggested to do so. Continual degradation of samples is seen during this exposure to moisture.

The optimized ratio for MOF/Pt catalyst/Sucrose, as given previously,[35] was 8:1:1.33. Here, the catalyst was 5wt% Pt/AC. This ratio seemed to yield the highest spillover enhancements.

Melting and Carbonization of Sucros. To encourage the melted sucrose to spread evenly and to coalesce into the crevices between the particles (by minimizing surface tension), Lifeng Wang did not spread the mixed sample in a thin layer during carbonization. The mixture is best placed in deep piles. Some "carbonized sucrose" can be observed on the quartz tube if the sample spreads too thin and the ratio is then not as specified.

The thermal stability tests cited in the literature were performed by dynamic TGA/DTG experiments, i.e., at a constant heat rate of typically several degrees C/minute. For example, IRMOF-1 was cited as being stable at 573 K from DTG data.[46] In the carbonization step, constant heating at a fixed temperature for a long period of time (e.g. 12 hours) is needed. Moreover, the carbonization process for sucrose and glucose is exothermic (e.g., 237 cal/g for glucose). Lab experience is that when the carbonization temperature exceeded 523 K, the IRMOF-8 or IRMOF-1 structures began to collapse, as the BET surface area reduced severely.

Moisture Stability and Importance of Maintaining BET Surface Area/Pore Volume. To study the stability of IRMOF-8 upon H_2O adsorption, the as-synthesized sample was exposed to indoor ambient air at room temperature, at a relative humidity of 40 %. The XRD patterns of the sample changed significantly after being exposed to air for 3 days (Figure 12). These results indicated that the framework structure of IRMOF-8 was degraded by H_2O after exposure to ambient air, which is in agreement with previous observation.[57,58] A direct immersion of the IRMOF-8 sample into water for 10 min resulted in the loss of the surface area. To minimize decomposition of MOFs, the samples were immediately evacuated and measured in the low and high-pressure systems. Upon exposure to ambient air, MOFs adsorb moisture very quickly and some of the adsorbed water can not be desorbed by degassing at room temperature.[57,58] The adsorbed moisture quickly causes hydrolysis of the MOF sample and decreases surface area.

Upon successful bridging and sample activation, the BET surface area and pore volume of the sample typically dropped by 10-15%.[35] Larger decreases indicate collapse of microstructure

and/or pore blockage, and will lead to diminished hydrogen uptake. Thus, it is important to measure the BET surface area and micropore volume before and after sample preparation.

Sample Pretreatment/Activation Prior to H_2 Uptake Measurement. Prior to isotherm measurements, the bridged sample was degassed in vacuum at 473 K for 24 h. Higher temperatures are not used in order to avoid MOF structure damage. However, lab experience suggests temperatures significantly below 473 K are not adequate to enable spillover processes. Figure 13 shows the isotherms of Pt/C/IRMOF-8 after being degassed at 393 K and 473 K for 12 hours. The Pt/C/IRMOF-8 degassed at 473 K has a higher slope than the one degassed at 393 K. The isotherm slope is has been used as a direct indicator for spillover. It is found now that low pressure isotherms are unreliable due to high variability in free space measurements, however activation at 473K in vacuo for 24 hours was used in this work.[35]

As mentioned, by successful bridging and sample treatment/activation, Tsao et al.[37] were able to obtain high enhancements for IRMOF-1 and IRMOF-8. Miller et al.,[38] using samples from Tsao et al., obtained similar results as measured by Miller's gravimetric system. Interesting results on the relatively moisture-stable MIL-53(Al) and MIL-101 were obtained by Liu et al.[39] In the work of Liu et al., the H_2 uptake was increased from 0.05 wt% at 298K and 5 MPa (due to small surface area of <290 m^2/g) to 0.63wt% after successful bridging. While for MIL-101, the uptake increased from 0.38wt% to 1.14wt% at 298K and 5 MPa upon bridging. All of these show a strong promise for increased efforts to maximize the spillover of MOFs.

Conclusion

In this work, the different factors and problems associated with the synthesis and pretreatment of Pt-doped carbon and catalyst-bridged MOFs were studied and discussed with respect to their effects on hydrogen spillover. Even minor deviations in sample preparation and treatment may lead to diminished spillover effects. Predominantly those relating to the dispersion of the platinum, which is the novel finding here.

For Pt-doped carbon, (1) Highly dispersed Pt nanoparticles (i.e., ~2 nm diameters) enhances spillover. The Pt particle size is affected by the addition rate of H_2PtCl_6 solution into the AX-21/acetone slurry, the concentration of the H_2PtCl_6 solution, and the treatment temperature; (2) On this highly dispersed Pt, Pt(110) face and high energy edges/steps correlated to higher

spillover capacity; (3) Ultrasonication helps to create a higher dispersion of metal particles; (4) Full passivation after H_2 reduction is necessary to avoid degradation of the sample; (5) After reduction by H_2 at 573 K, sample pretreatment by degassing at higher temperatures (623 K) is needed to clean the sample surfaces.

For catalyst-bridged MOFs, (1) The MOFs quality and particle size are affected by the starting materials and the synthesis method. Nanosized MOFs are preferred because the nanosized MOFs have more external surface area and more contacts with the dissociation source; (2) Uniform mixing of the three components Pt/C, sucrose and MOF is most likley important for hydrogen spillover, which is affected by the sample amounts, compatibility in the particle sizes, and the grinding time and intensity. Batch-to-batch mixing issues must be reduced to decrease the large storage capacity variability presently observed with these spillover materials; (3) A carbonization temperature of 523 K is recommended (for IRMOF-8). Higher temperatures will degrade the MOF structure due to the exothermic carbonization process for sucrose or glucose; (4) It is crucial to minimize the exposure of MOFs to ambient air. The moisture in the air causes hydrolysis of the MOFs; (5) Prior to measurements and characterization, a high degassing temperature (473 K) is most likely necessary to fully prepare the sample.

The characterization of the adsorption sites on the Pt/C system show four individual peaks, two I assign to Pt and two to carbon. The two Pt peaks appear to be β_1 and β_2 for the (110) face and the carbon peaks most likely correspond to surface diffusion and surface recombination of the hydrogen atoms. The TEM images show (111) and (100) surfaces are also present but not in the TPD spectra and I suggest that they may be masked by other more strongly adsorbed species or by bonding with the carbon or groups on the carbon. This all leads me to suggest that increasing the surface area is not the sole contribution from smaller Pt nanoparticles, but also the decrease in the average coordination of the surface/edge atoms. This makes these particles more effective and also more disperse. I expect this trend to continue with other metal particles as well as observing the same two TPD carbon peaks without dependence on the choice of metal.

Reproduction of most of the previous work with Pt/C has shown that this adsorbent is readily replicated and leads to interesting spillover findings on the role of Pt. I identify more

evidence from this study that a diffusion step is rate limiting for adsorption, further indicating that spillover is occurring and is enhancing these adsorbents, however the significance of the capacity is unknown.

Acknowledgments. The authors acknowledge the funding provided by the U.S. Department of Energy's Office of Energy Efficiency and Renewable Energy within the Hydrogen Sorption Center of Excellence (HS CoE) as well as the funding from NSF.

References:

1. Robell, A. J.; Ballou, E. V.; Boudart, M. *J. Phys. Chem.* **1964**, *68*, 2748.
2. Conner, W. C. Jr.; Falconer, J. L. *Chem. Rev.* **1995**, *95*, 759
3. Wang, L.; Yang, R. T. *Energy Environ. Sci.* **2008**, *1*, 268.
4. Sinfelt, J. H.; Lucchesi, P. J. *J. Am. Chem. Soc.* **1963**, *85*, 3365.
5. Khoobiar, S. *J. Phys. Chem.* **1964**, *68*, 411.
6. Boudart, M.; Vannice, M. A.; Benson, J. E. Z. *Phys. Chem.* **1969**, *64*, 171.
7. Boudart, M.; Aldag, A. W.; Vannice, M. A. *J. Catal.* **1970**, *18*, 46.
8. Srinivas, S. T.; Rao, P. K. *J. Catal.* **1994**, *148*, 470.
9. Mitchell, P. C. H.; Ramirez-Cuesta, A. J.; Parker, S. F.; Tomkinson, J.; Thompsett, D. *J. Phys. Chem. B* **2003**, *107*, 6838.
10. Mitchell, P. C. H.; Ramirez-Cuesta, A. J.; Parker, S. F.; Tomkinson, J. *J. Mol. Struct.* **2003**, *651-653*, 781.
11. Zhan, D.; Velmurugan, J.; Mirkin, M.V. *J. Am. Chem. Soc.* **2009**, *131*, 14756.
12. Panayotov, D. A.; Yates, J. T. Jr. *J. Phys. Chem. C* **2007**, *111*, 2959.
13. Contescu, C. I.; Brown, C. M.; Liu, Y.; Bhat, V. V.; Gallego, N. C. *J. Phys. Chem. C* **2009**, *113*, 5886.
14. Saha, D.; Deng, S. *Langmuir* **2009**, *25*, 12550.
15. Zieliski, M.; Wojcieszak, R.; Monteverdi, S.; Mercy, M.; Bettahar, M. M. *Int. J. Hydrogen Energy* **2007**, *32*, 1024.
16. Zieliski, M.; Wojcieszak, R.; Monteverdi, S.; Mercy, M.; Bettahar, M. M. *Catal. Comm.* **2005**, *6*, 777.
17. Anson, A.;, Lafuente, E.; Urriolabeitia, E.; Navarro, R.; Benito, A. M.; Maser, W. K.; Martinez, M. T. *J. Phys. Chem. B* **2006**, *110*, 6643.
18. Li, Y. W.; Yang, R. T. *J. Phys. Chem. C* **2007**, *111*, 11086.
19. Tsao, C. S.; Tzeng, Y. R.; Yu, M. S.; Wang, C. Y.; Tseng, H. H.; Chung, T. Y.; Wu, H.nC.; Yamamoto, T.; Kaneko, K.; Chen, S. H. *J. Phys. Chem. Lett.* **2010**, *1*, 1060.
20. Zubizarreta, L.; Menndez, J. A.; Pis, J. J.; Arenillas, A. *Int. J. Hydrogen Energy* **2009**, *34*, 3070.
21. Back, C.; Sandi, G.; Prakash, J.; Hranisavljevic, J. *J. Phys. Chem. B* **2006**, *110*, 16225.
22. Kim, B. J.; Lee, Y. S.; Park, S. J. *Int. J. Hydrogen Energy* **2008**, *33*, 4112
23. Lupu, D.; Biris, A. R.; Misan, I.; Jianu, A.; Holzhuter, G.; Burkel, E. *Int. J. Hydrogen Energy* **2004**, *29*, 97
24. Lee, Y. S.; Kim, Y. H.; Hong, J. S.; Suh, J. K.; Cho, G. J. *Catal. Today* **2007**, *120*, 420.
25. Lueking, A. D.; Yang, R. T. *Appl. Catal. A* **2004**, *265*, 259.
26. Wang, L.; Yang, R. T. *J. Phys. Chem. C* **2008**, *112*, 12486
27. Nishihara, H., Hou, P. X., Li, L. X., Ito, M., Uchiyama, M., Kaburagi, T., Ikura, A., Katamura, J., Kawarada, T., Mizuuchi, K. and Kyotani, T. *J. Phys. Chem. C* **2009**, *113*, 3189.
28. Zlotea, C.; Campesi, R.; Cuevas, F.; Leroy, E.; Dibandjo, P.; Volkringer, C.; Loiseau, T.; Ferey, G.; Latroche, M. *J. Am. Chem. Soc.* 2010, DOI:10.1021/ja9084995.
29. Cheon, Y. E.; Suh, M. P. *Angew. Chem. Int. Ed.* **2009**, *48*, 2899.
30. Yang, S. J.; Cho, J. H.; Nahm, K. S.; Park, C. R. *Int. J. Hydrogen Energy* **2010**, 4, 66.
31. Benson, J. E.; Kohn, H. W. and Boudart, M. J. *Catal* **1966**, 5, 307.
32. Bonc, G. C.; Mallat, T. J. *Chem. Soc., Faraday Trans. I* **1981**, 77, 1473.

33. Keren, E.; Soffer, A. *J. Catal* **1977**, 50, 43.
34. Neikam, W. C. and Vannice, M. A. *Proc. 5th Intern. Congress on Catalysis* **1973**, 1, 40, 609-619
35. Li, Y.W.; Yang, R. T., *J. Am. Chem. Soc.* **2006**, 128, 8136.
36. Yang, R. T.; Li, Y.W.; Lachawiec. A. J., *2007 Annual Progress Report, DOE Hydrogen Program*, **2007**, IV.C.1b, 539-541.
37. Tsao, C.S.; Yu, M. S; Wang, C.Y.; Liao, P.Y.; Chen, H.L.; Jeng, U.S.; Tzeng, Y.R.; Chung, T.Y.; Wu, H.C. *J. Am. Chem. Soc*. **2009**, 131, 1404-1406.
38. Miller, M.A.; Wang, C.Y.; Merrill, G. N. *J. Phys. Chem. C.* **2009**, 113, 3222-3231.
39. Liu, Y.Y.; Zheng, J-L.; Zhang, J.; Xu. F.; Sun, L-X. *Intern. J. Hydrogen Energy* **2007**, 32, 4005-4010.
40. Zhou, C.; Wu, J.; Nie, A.; Forrey, R. C.; Tachibana, A.; Cheng, H. *J. Phys. Chem. C* **2007**, *111*, 12773.
41. Trens, P.; Durand, R.; Coq, B.; Coutanceau, C.; Rousseau, S.; Lamy, C. *Applied Catalysis B* **2009**, *92*, 280.
42. Cheng, H.; Chen ,L.; Cooper, A. C.; Sha, X.; Pez, G. P. *Energy Environ. Sci.* **2008**, *1*, 338.
43. Ludwig, J.; Vlachos, D. G., van Duin, A. C. T.; Goddard III, W. A. *J. Phys. Chem. B* **2006**, *110*, 4274.
44. Li, Y.; Yang, F.H.; Yang, R.T. *J. Phys. Chem. C* **2007**, *111*, 3405.
45. Lim, B., Jiang, M.; Camargo, P. H. C.; Cho, E. C.; Tao, J.; Lu, X.; Zhu, Y.; Xia, Y. *Science* **2009**, *324*, 1302.
46. Huang, L. M.; Wang, H. T.; Chen, J. X.; Wang, Z. B.; Sun, J. Y.; Zhao, D. Y.; Yan, Y. S. *Microporous Mesoporous Mater* **2003**, 58, 105.
47. Lachawiec, A. J., Jr. and Yang, R. T. *Langmuir* **2008**, 24, 6159.
48. Shern, C.S. *Surface Science* **1992**, 264, 171-176
49. Campesi, R.; Cuevas, F.; Gadiou, R.; Leroy, E.; Hirscher, M.; Vix-Guterl, C.; Latroche, *M. Carbon* **2008**, 46, 206.
50. Schueller, B. S. ; Yang, R. T. *Ind. Eng. Chem. Res.* **2001**, 40, 4912.
51. Stadie, N. P.; Purewal, J. J.; Ahn, C. C.; Fultz, B. *Langmuir* **2010**, Article ASAP
52. McCabe, R. W. ; Schmidt, L. D. *Surface Science*, **1976**, 60, 85-98.
53. McCabe, R. W. ; Schmidt, L. D. *Surface Science*, **1977**, 65, 189-209.
54. Han, S.S.; Mendoza-Cortes, J.L.; Goddard III, W.A. *Chem. Soc. Rev.* **2009**, 38, 1460–1476
55. Suri, M.; Dornfeld, M. and Ganz, E., *J. Chem. Phys*. **2009**, 131, 174703.
56. Rosi, N. L.; Eckert, J.; Eddaoudi, M.; Vodak, D. T.; Kim, J.; O'Keefee, M.; Yaghi, O. M. *Science* **2003**, 300, 1127
57. Li, Y.W.; Yang, R. T., *Langmuir*, **2007**, 23, 12937.
58. Nguyen, J. G.; Cohen, S. M. *J. Am. Chem. Soc.* **2010**, 132 (13), 4560–4561

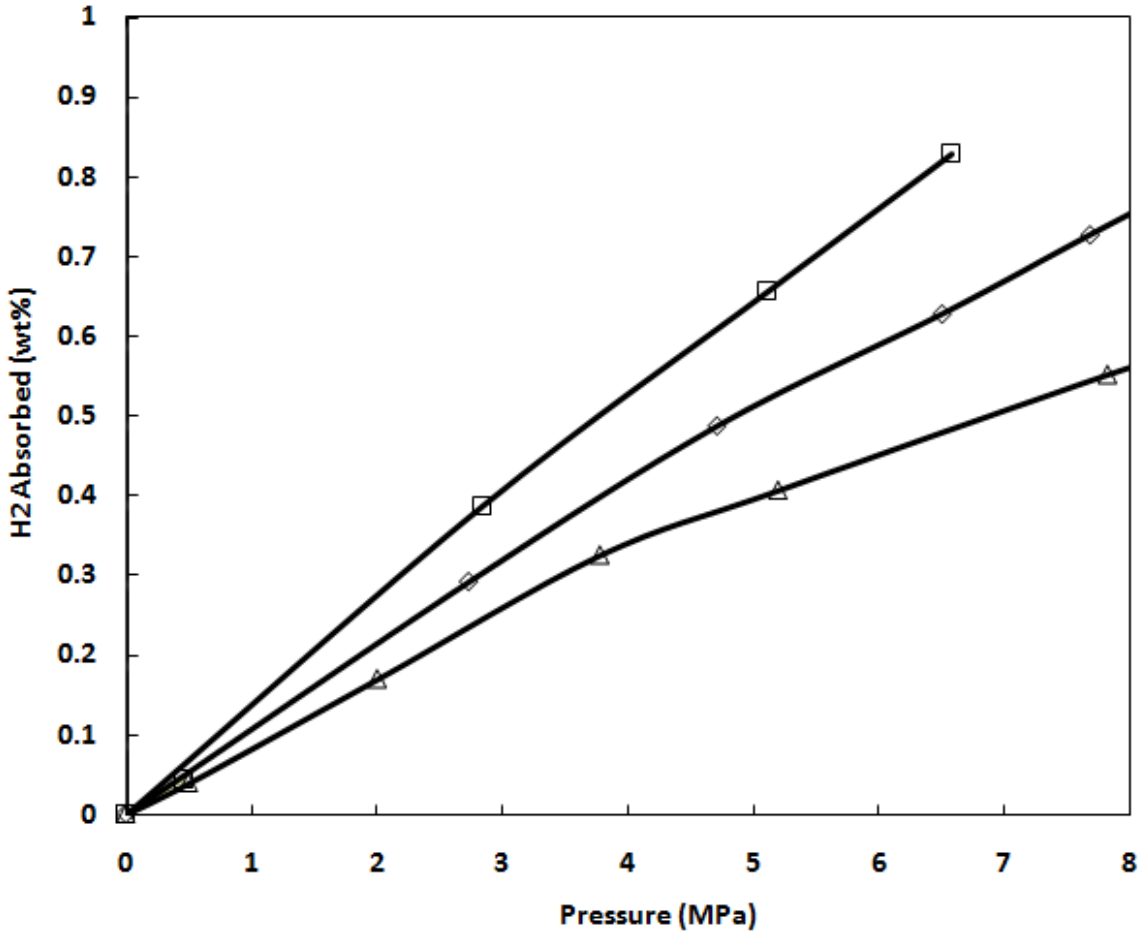

Figure 1. Hydrogen isotherms on Pt/AX-21 at 298K. Various doping rates of chloroplatinic acid during the synthesis of Pt/AX21 and subsequent results for spillover capacity. Elapsed times for addition were 10 min (□), 5 min (◇) and 1 min (△). Isotherms may not be statistically significant as noted in the appendix.

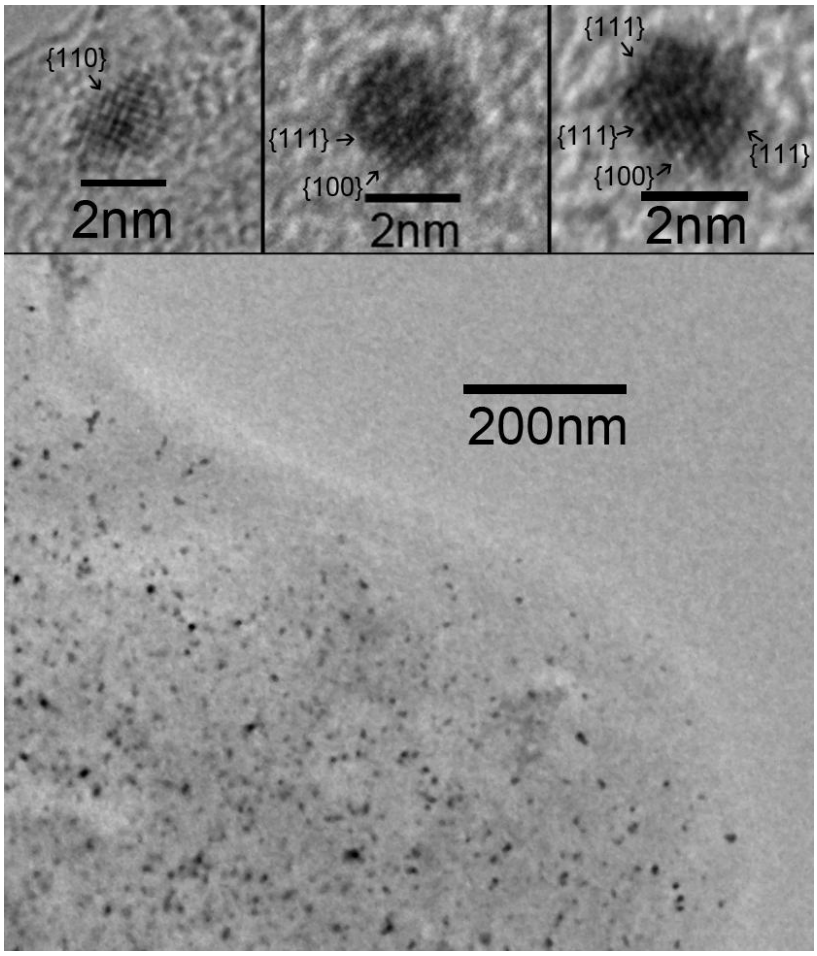

Figure 2. TEM of Pt nanoparticles (on Pt/AX-21) showing even and small dispersion with examples of some of the nanoparticles.

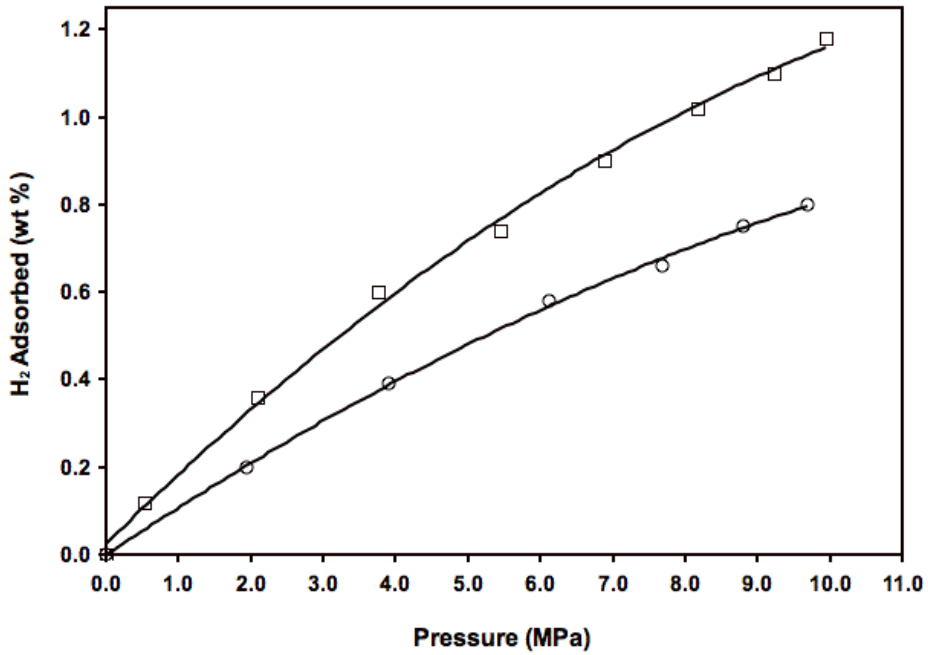

Figure 3. Hydrogen isotherm on Pt/AX-21 before (□) and after (○) sintering at 873 K for 60 hours. Obtained by Lifeng Wang.

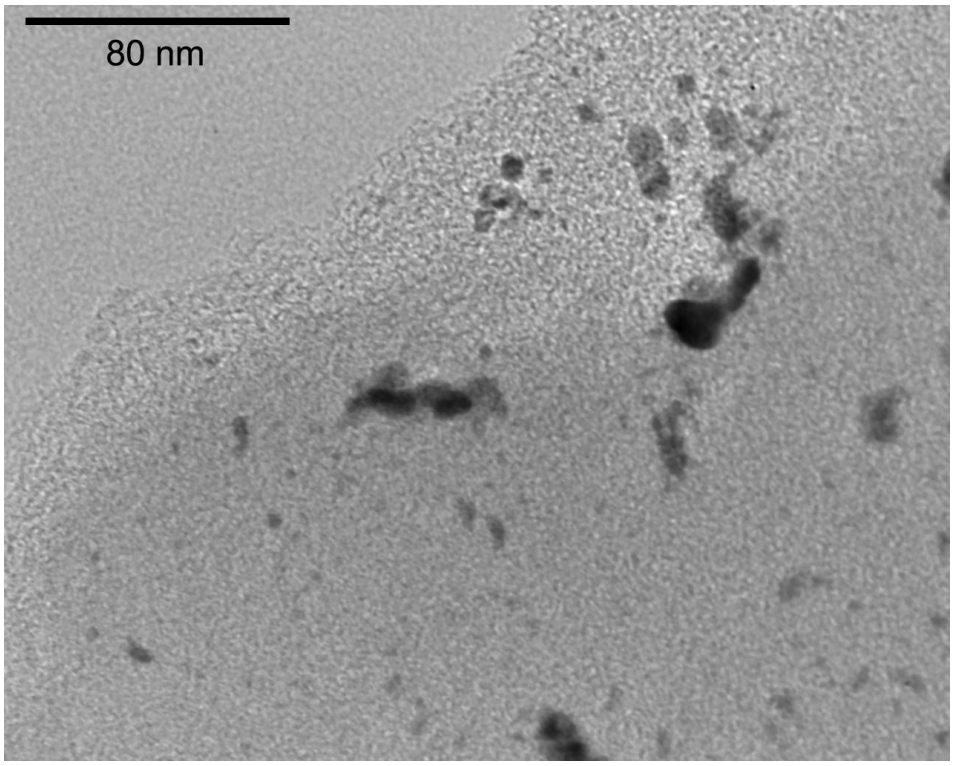

Figure 4. TEM of Pt/AX-21 sintered at 873 K for 60 hours

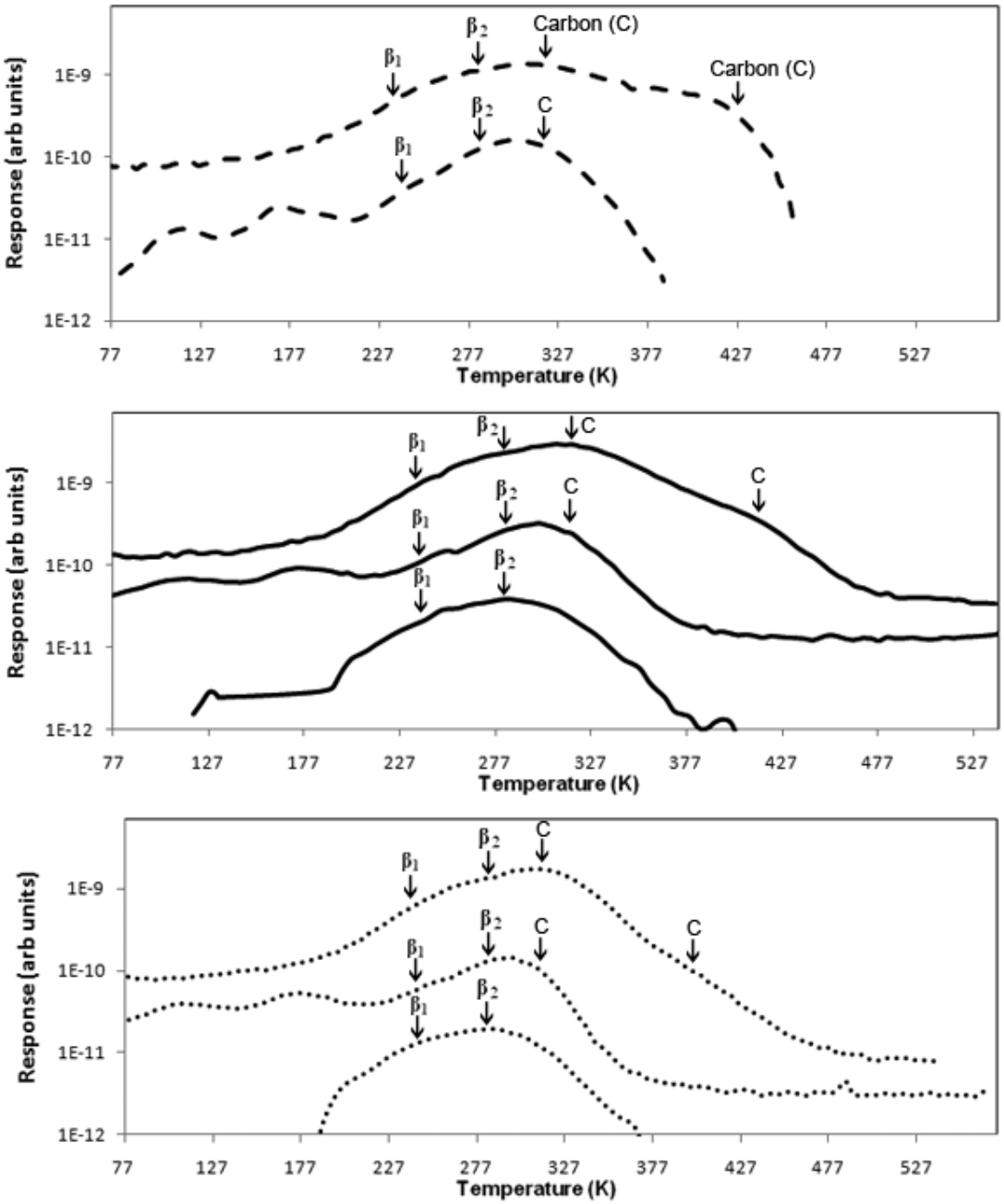

Figure 5. TPD of Pt/AX21 with a variation of temperature of Hydrogen exposure. Increased signal corresponds to increased doping temperatures that were held for 40 minutes. Temperatures dosed were 77K, 200K and 298K. The top spectra are of H2 (— —), middle of HD (———) and bottom of D2 (·····). The spectrum for H2 at 77K could not be obtained due to low signal to noise ratio. β_1 and β_2 refer to sites on Pt(110)[42]. The separation between the β_2 and Carbon peaks is shown while the β_1 becomes obscured.

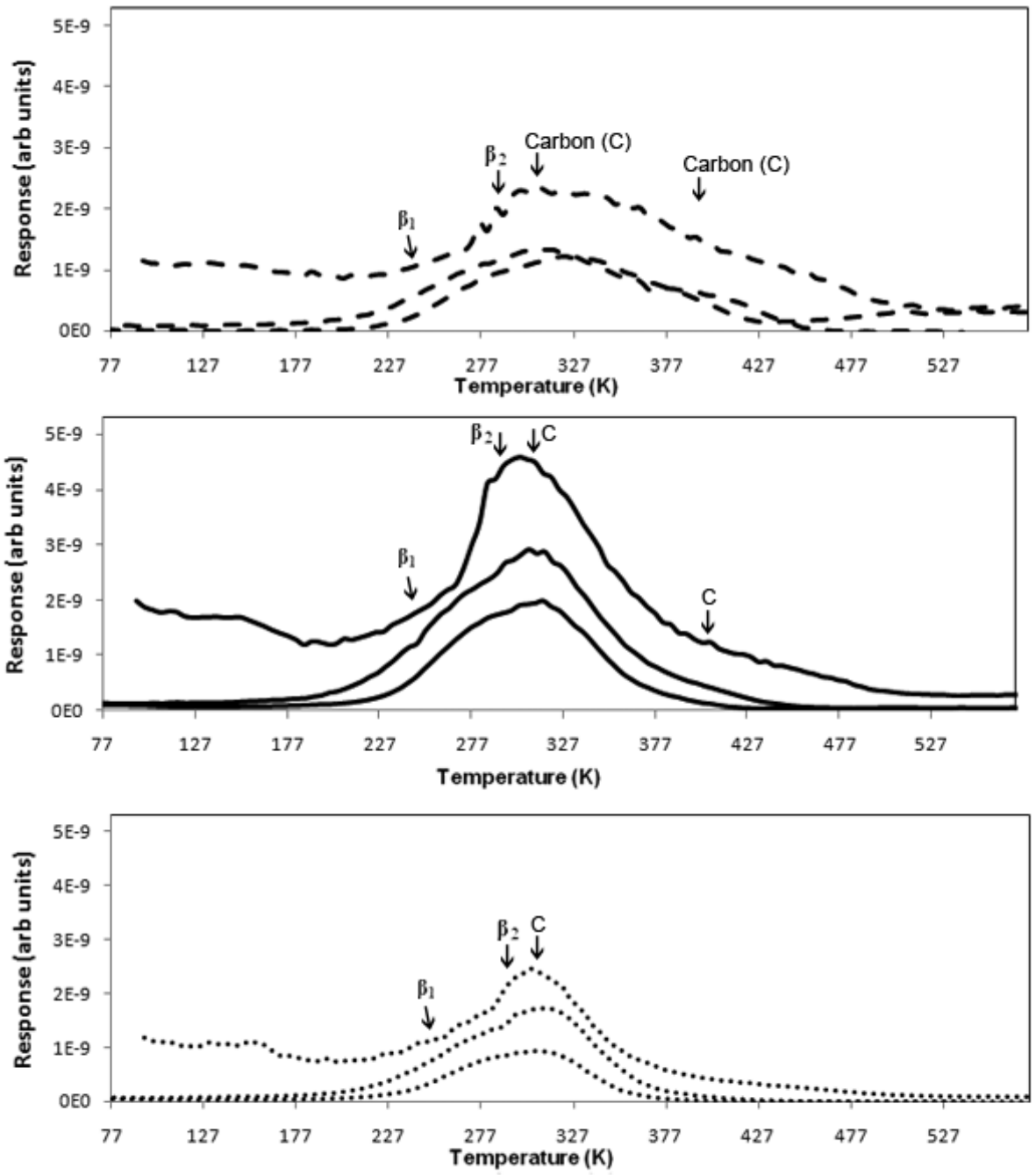

Figure 6. TPD of Pt/AX21 with a varying pressure of Hydrogen exposure. Increased signal corresponds to increased pressure (150 torr, 400 torr and 16 atm). The top spectra are of H2 (— —), middle of HD (——) and bottom of D2 (·····). β_1 and β_2 refer to sites on Pt(110)[42], while the β_2 is mostly obscured, the β_1 is clearly shown.

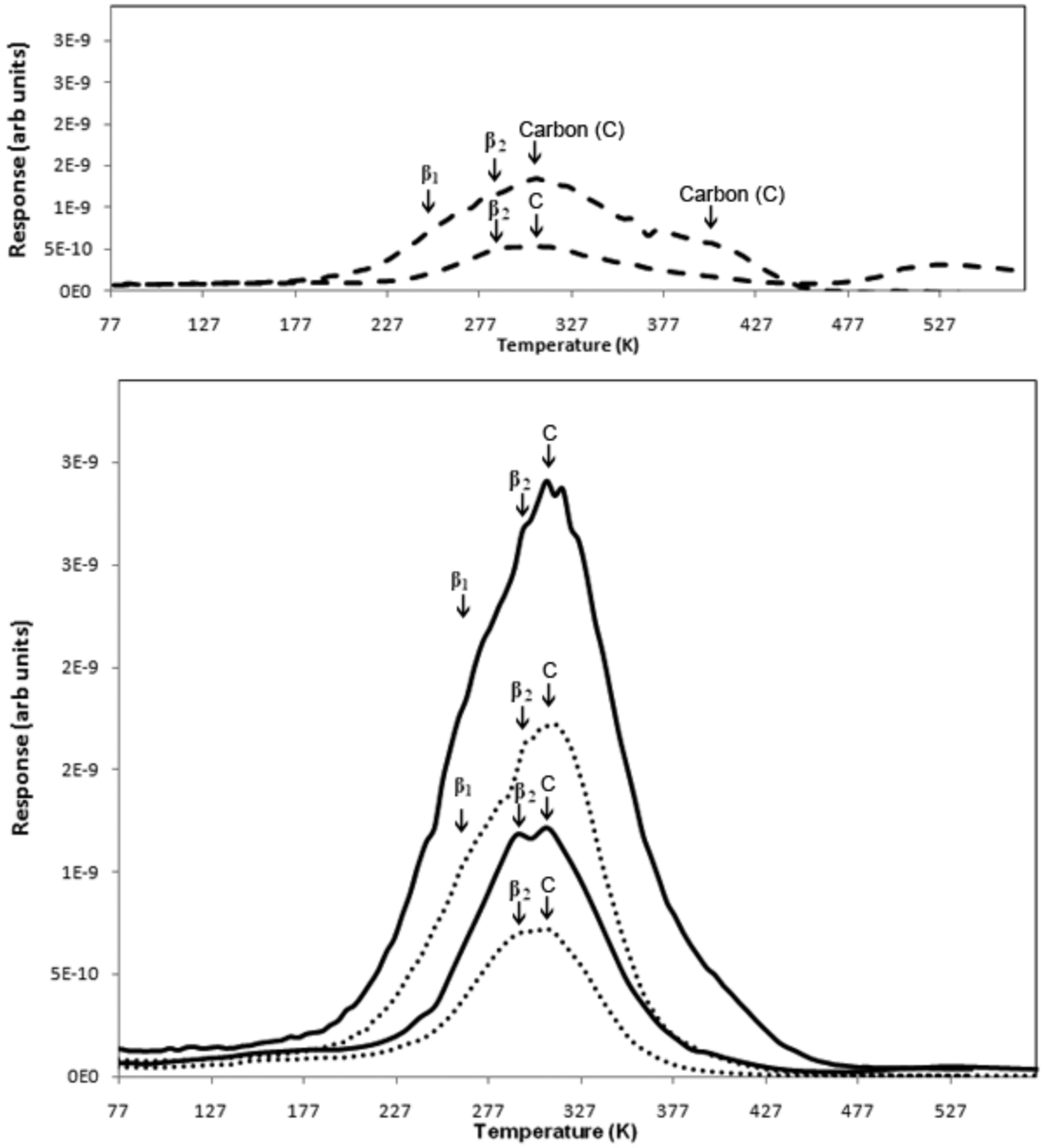

Figure 7. TPD of Pt/AX21 with a varying exposure time. The increased signal corresponds to increased exposure time from 4 min to 40 min. The top spectra are of H_2 (— —), middle of HD (——) and bottom of D_2 (·····). β_1 and β_2 refer to sites on Pt(110)[42]. The β_1 is mostly obscured and the β_2 and Carbon peaks blend together.

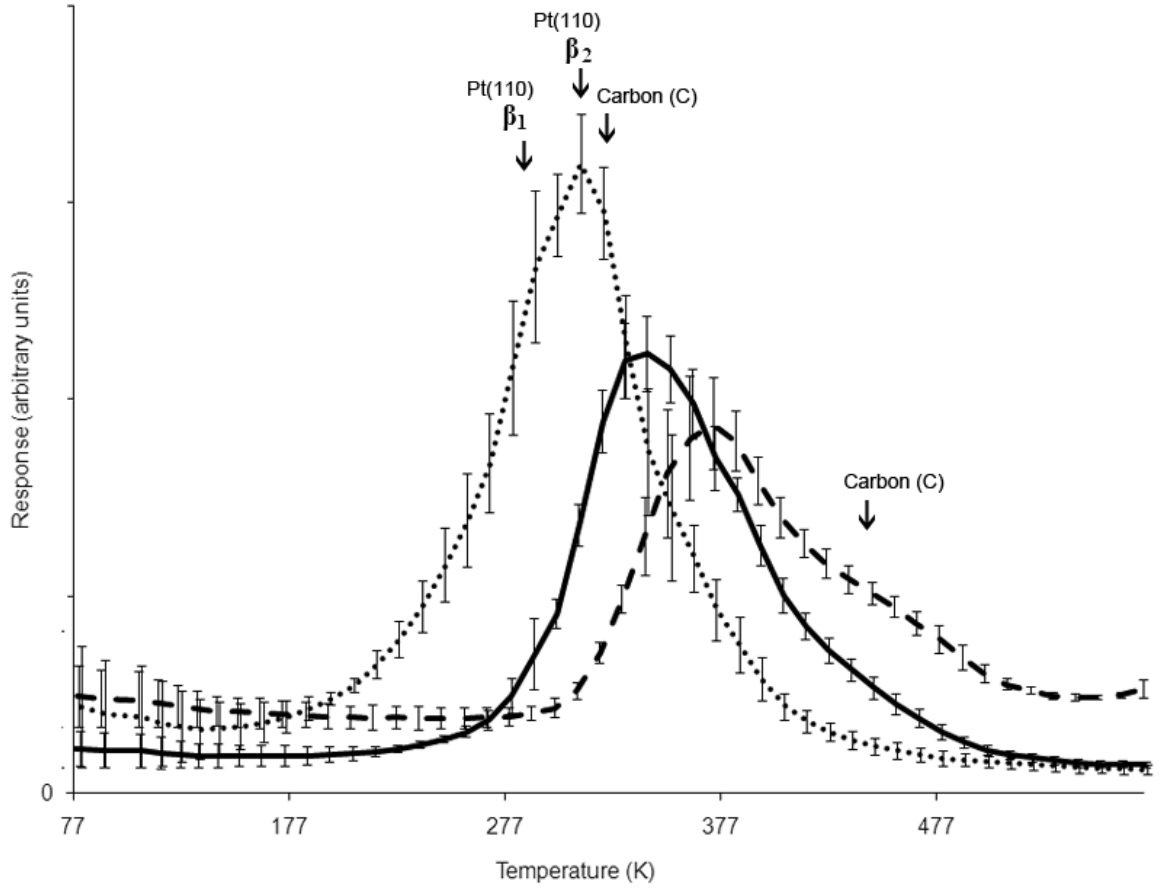

Figure 8. TPD Deuterium tracer results by dosing H2 first followed by D2. Results are the compilation of 4 experiments. D2(·····), HD(——) and H2(— —) are shown to come off in reverse dosing order. β_1 and β_2 refer to sites on Pt(110)[42] and are almost completely obscured.

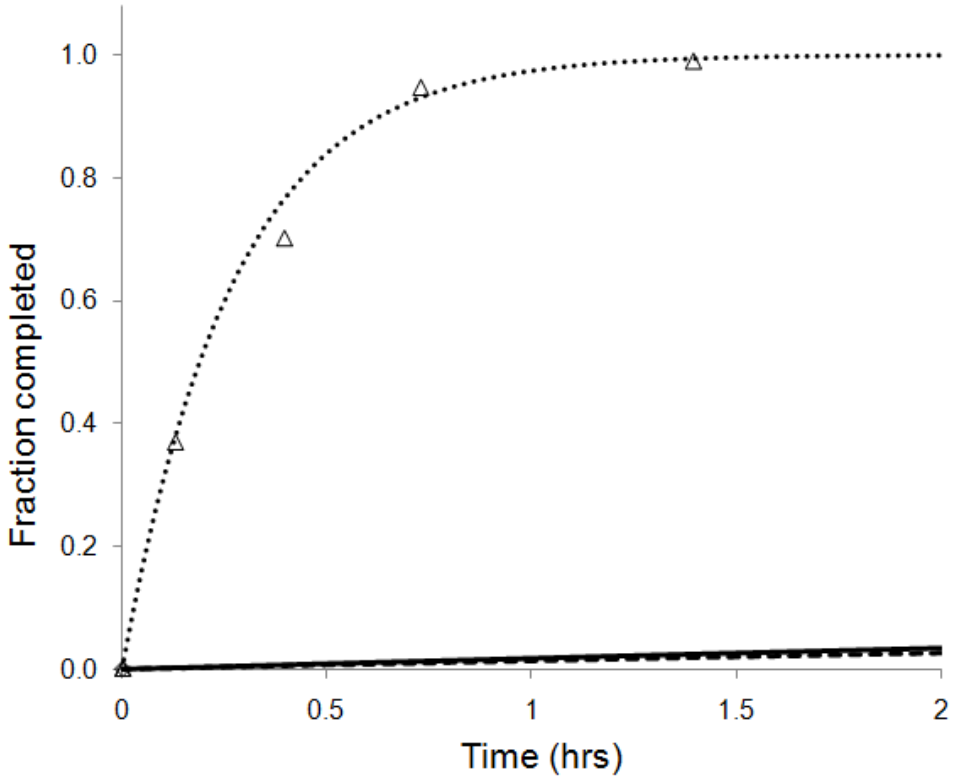

Figure 9. Rate of HD formation. Plain AX21 (— —) and a blank (——) are shown as a reference to the rate of dissociation and recombination by Pt/AX21 (△). A first order rate fit was observed (·····).

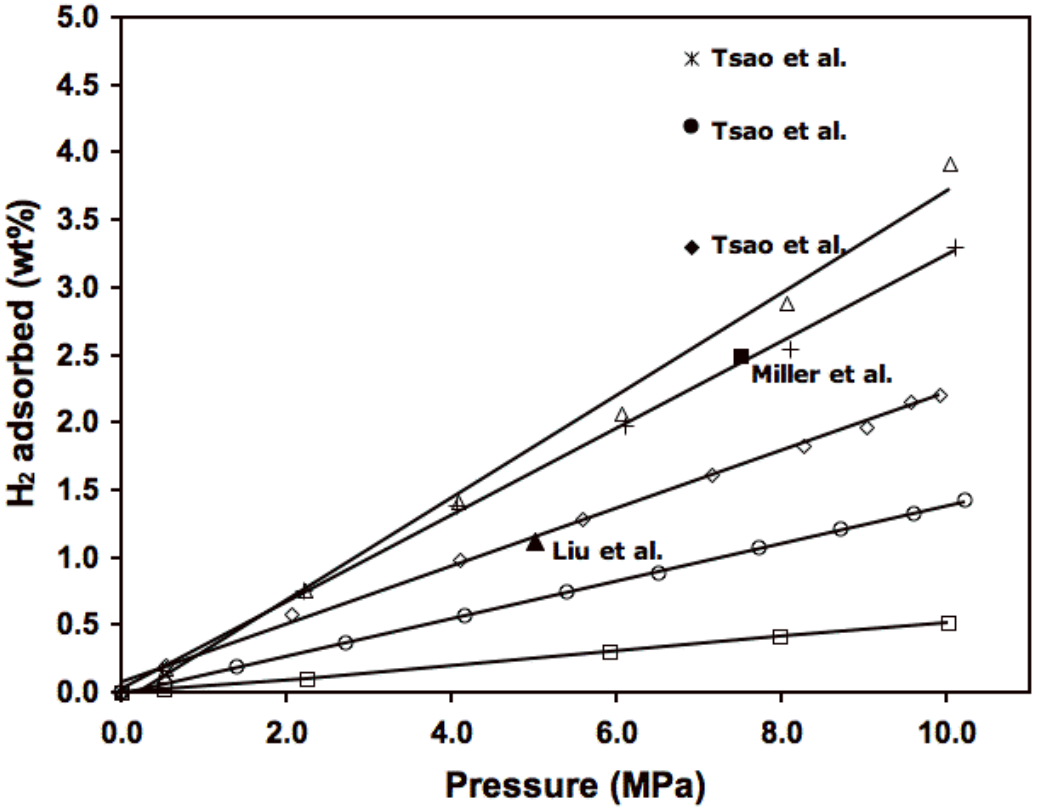

Figure 10. Storage capacities of various bridged IRMOF-8 samples and pure IRMOF-8 (□). Data points from the literature are also shown for comparison: Tsao et al. (Ref. 37) and Miller et al. (■ Ref. 38). The data point from Liu et al. (◢ Ref. 39) is for bridged MIL-101. See text for successful spillover on bridged MIL-53 and MIL-101. Obtained by Lifeng Wang.

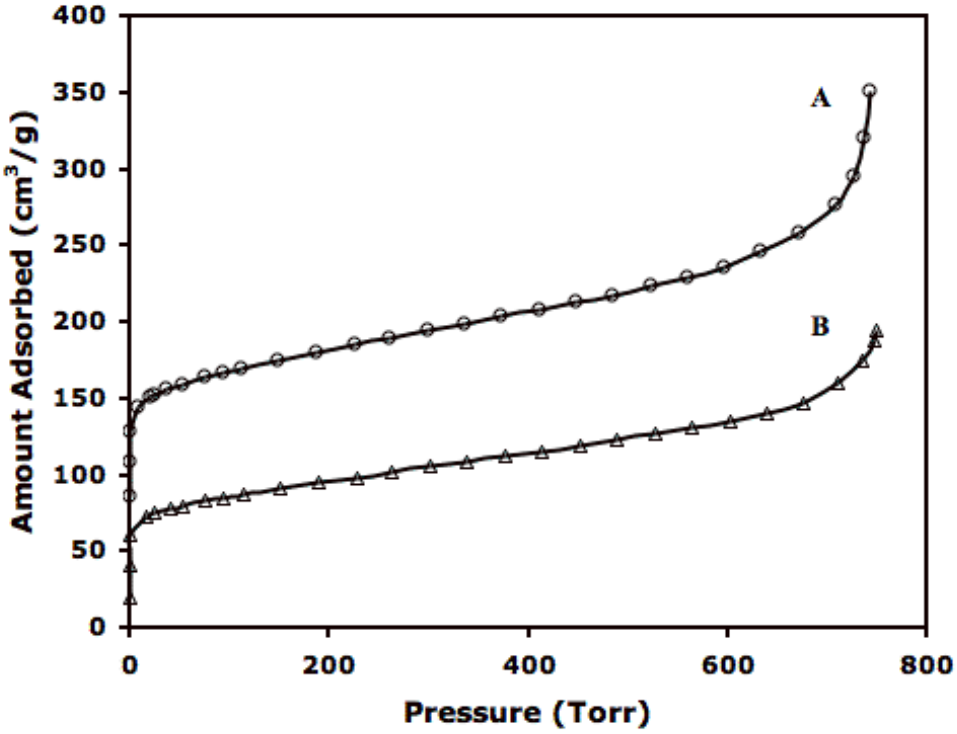

Figure 11. Nitrogen isotherms at 77K of IRMOF-8 synthesized from zinc nitrate (A) freshly opened and (B) opened for a month. Obtained by Lifeng Wang.

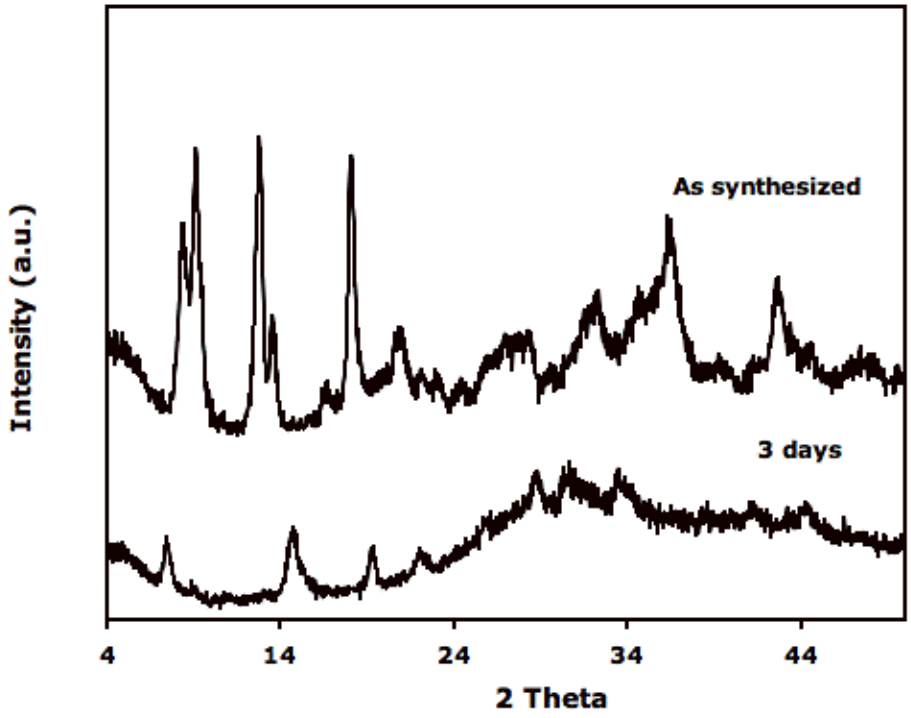

Figure 12. XRD patterns of as synthesized IRMOF-8 and IRMOF-8 exposed to air for 3 days. Obtained by Lifeng Wang.

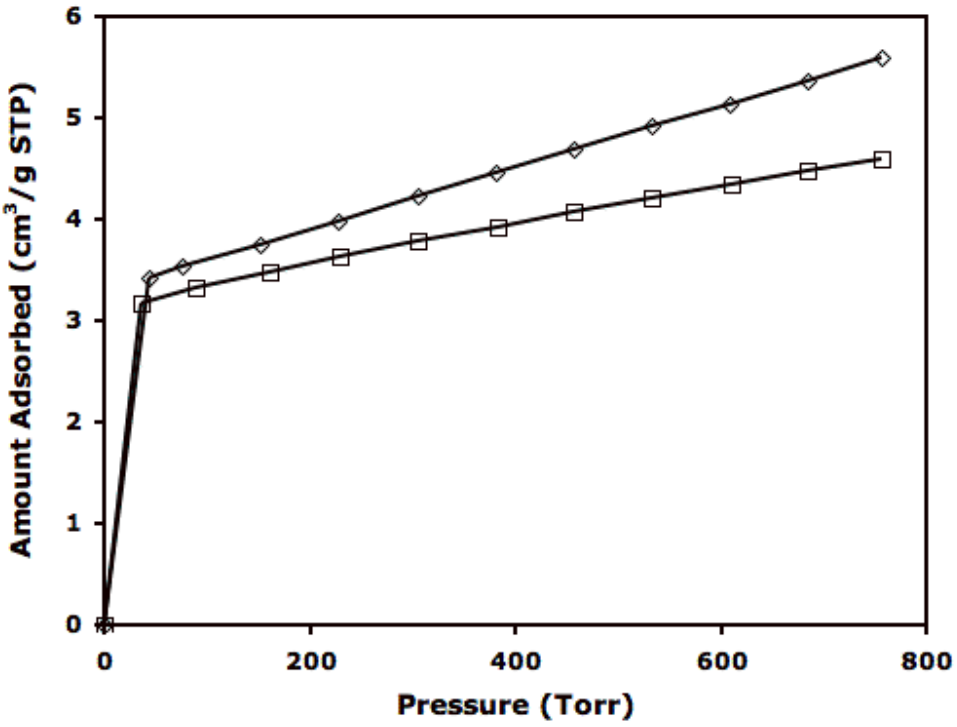

Figure 13. Hydrogen isotherms at 298 K for Pt/C/IRMOF-8 activated/degassed at 393 K (□) and 473 K (◇) for 12 hours, showing severely diminished spillover by inadequate activation. Equilibration for each data point was reached in <5 sec. Obtained by Lifeng Wang.

Chapter 2: Unique Hydrogen Adsorption Properties of Graphene

Introduction

Since the first isolation of graphene from graphite,[1] graphene has been synthesized by various routes[2-5] and has shown a wide variety of fascinating properties, such as the quantum Hall effect at room temperature, extremely high carrier mobility, ambipolar field-effect, and sensitive response to single molecules.[6,7] The recent theoretical calculation results indicate that graphene may also work as a sorbent for hydrogen storage.[8-10] Various nanostructured and microporous carbon-based materials including carbon nanotubes (CNTs), activated carbons (ACs), mesoporous carbons (MCs), templated carbons (TCs), and metal organic frameworks (MOFs), have been studied intensively due to their light weight, high surface areas, and relative chemical stabilities.[11-17] However, recent results showed that these carbon-based materials cannot store a sufficient amount of H_2 required for transportation applications merely by physical adsorption at ambient temperature. Novel storage sorbent materials and ways to further enhance the storage capacities need to be explored.

The promising results predicted for hydrogen storage on ideal graphene have stimulated experimental studies.[8-10] However, experimental studies have been limited to hydrogen adsorption on low-surface-area graphene-like materials[18-20] and the hydrogenation of supported graphene membrane by plasma exposure or the use of a hydrogen atom beam source.[21,22] An in-depth study of hydrogen adsorption on graphene and an understanding of the adsorption process are desired. In this work, Lifeng Wang studied the hydrogen adsorption properties of graphene with a high surface area of 2139 m^2/g and compared it with the most studied carbon materials (for H_2 storage). Among all the tested carbons, graphene showed a superior hydrogen storage capacity as well as displaying a uniquely slow hydrogen adsorption process, which cannot be statistically verified, but may be significant. I have also observed catalytic hydrogen dissociation on graphene for the first time and compared its similarities to metal doped carbons.

Experimental Section

Synthesis

The graphene was prepared by following a published solvothermal and sonication procedure.[4] Typically, 2 g of sodium and 5 mL of ethanol (molar ratio, 1:1) was sealed in a teflon-lined reactor vessel and heated at 220 ^{o}C for 72 h. After that, the reactor vessel was cooled to room temperature and a solid solvothermal product (graphene precursor) was obtained. This material was then transferred to a horizontal quartz tube in He atmosphere and rapidly pyrolyzed at 1050 ^{o}C for 2 min. The resulting black product was washed with copious amounts of deionized water and sonicated in ethanol. The final product was collected by filtration and dried in vacuo at 100 ^{o}C for 24 h.

Mesoporous carbon (MC), templated carbon 1 (TC-1), templated carbon 2 (TC-2), templated carbon 3 (TC-3), MOF-177 were prepared according to published procedures.[23-28] The superactivated carbons AX-21 and Maxsorb were obtained from Anderson Development Company and Tokyo Zairyo Co Ltd, respectively. CNT-1 was obtained from Shenzhen Nanotech Port Co. The storage capacity of CNT-2 was cited from previous literature.[29] 6 wt % Pt-doped AX-21 was synthesized according to previous literature.[30]

Characterization

Nitrogen adsorption isotherms and low-pressure H_2 adsorption isotherms (0-1 atm) were measured by using a Micromeritics ASAP 2020 Analyzer. Nitrogen adsorption isotherms were measured at -196 ^{o}C. Low-pressure H_2 adsorption isotherms were measured at 0, 25, and 50 ^{o}C. Circulating baths were used to maintain the sample at 25 or 50 ^{o}C. An ice-water filled dewar flask was used to maintain 0 ^{o}C, and liquid nitrogen was used for -196 ^{o}C. High-resolution transmission electron microscopy (HRTEM) images of the materials were obtained on a JEOL 3011 analytical electron microscope equipped with EDX analysis operated at 300 kV. The elemental ratio of graphene was approximately C: 93 %; O: 6.5 %; Na: 0.5 % as analyzed by a Kratos Axis ultra XPS spectrometer (Supporting Figure S1).

Hydrogen adsorption at 25 ^{o}C and pressures greater than 0.1 MPa and up to 10 MPa was measured using a static volumetric technique with a specially designed Sieverts-type apparatus. The apparatus was previously tested and shown to be leak-free and accurate through

calibration by using $LaNi_5$, AX-21 carbon, zeolites, and MOFs at 25 ^{o}C.[31] Accuracy here is +/- 0.6wt% at 100atm for a 200mg sample. As shown in lab previous work, the high pressure isotherms of the commercially available superactivated carbons (i.e., AX-21, GX-31, Maxsorb) are known and have been used as standard materials for testing of the measurements. For a superactivated carbon with a BET surface area of 2800 m^2/g, the isotherm at 298K should be slightly concave with an uptake of 0.6 wt% at 10 MPa.[31] 120-200 mg of sample was used for each high-pressure isotherm measurement. Analysis of evolved gases during TPD experiments was performed with an AeroVac 1200 Magnetic Sector mass spectrometer (VTI, Inc.).

H_2/D_2/HD isotope equilibrium reaction and temperature programmed desorption

The H_2/D_2/HD equilibrium on graphene was measured using a slightly modified procedure proposed by Ishikawa et al.[32] In this new procedure H_2 and D_2 were mixed in a 1:1 ratio at 4.3 MPa. This mixture was allowed to equilibrate for 2 h at room temperature before being exposed to the sample at 1.6 MPa. The small sample cell was then closed and allowed to react for a given amount of time before being quenched in liquid nitrogen. The gas in the sample cell was analyzed using mass spectrometer (MS) after 5 minutes from initial sample cell submersion in liquid nitrogen. The mass spectrometer was set in sweep mode to analyze (*m/z*) peaks 1-6 in order to fully differentiate hydrogen, deuterium hydride and deuterium. 20 mg samples of graphene, AX-21, and 6 wt % Pt-doped AX-21, were subjected to this treatment for a series of different reaction times and compared to the results obtained using a blank sample cell. All samples were degassed at 250 ^{o}C for 8 hours under vacuum, except Pt-doped AX-21, which was degassed at 350 ^{o}C and an annealed graphene degassed at 550 ^{o}C. A reaction rate constant was also obtained for the blank cell, which was made of stainless steel.

Temperature programmed desorption (TPD) was performed on the samples once all physi-sorbed hydrogen was removed (20 min) and the *m/z* 2 peak had fallen to baseline. Heating at 10 ^{o}C/min ($\pm$1 ^{o}C/min) was performed while analyzing (*m/z*) peaks 1-6 in order to determine total hydrogen species desorbed.

Results and Discussion

The published solvothermal and sonication procedure[4] was selected because the production of graphene can be in gram-quantities, which is beneficial for achieving accurate storage

measurements and for use in further applications. The TEM image of the products (Figure 14) clearly shows the wrinkled graphene sheets and overlap between different sheets, which are in agreement with previous literature. A N_2 isotherm at 77K on graphene showed an increase at a low relative pressure and a hysteresis loop at relative pressures from 0.4-0.95 MPa (Supporting Figure S2). The graphene had a BET surface area of 2139 m^2/g, which was less than the 2630 m^2/g for ideal single-layer graphene. This indicates some partial overlap of graphene sheets rather than completely separated single-layer graphene.

Hydrogen storage on graphene was investigated at 25 ^oC and up to 10 MPa. As shown in Figure 15, graphene exhibited a surprisingly high storage capacity of 0.90 wt %. The hydrogen storages of a series of carbon materials including CNT, AC, MC, TC and MOF were measured to compare with graphene. In Figure 16, there is a clear relationship between the storage capacity and the BET surface area for all other tested carbons (with surface areas ranging from 810-3840 m^2/g.), as expected for physical adsorption. This correlation is in agreement with previous reports.[11,13] However, the storage capacity of graphene was well above the correlation. The capacity of 0.90 wt % for graphene was the highest compared with all the other carbons (0.62 wt % for AX-21, 0.72 wt % for Maxsorb, 0.66 wt % for MOF-177, and 0.82 wt % for TC-3, etc.). Considering the correlation between the capacity and surface area and extrapolating, a carbon with a BET surface area of 2139 m^2/g should have a capacity of 0.56 wt % at 10 MPa. This showed that the storage capacity on graphene was higher by 60 %. The reversibility was assessed by measuring the desorption branch down to 1 atm. It can be seen from Figure 15 that the desorption branch nearly coincided with the adsorption branch although there appeared to be slight hysteresis. The next two adsorption branches were in agreement with the first adsorption branch indicating no observable loss in adsorption sites during adsorption-desorption cycles at 25 ^oC (Figure 17).

In order to evaluate the interactions between graphene and H_2, the isosteric heats of adsorption were calculated from the adsorption isotherms at different temperatures by using the Clausius-Clapeyron equation (Figure 18). The hydrogen adsorption isotherms were measured at 0, 25 and 50 ^oC and the heat of adsorption values were determined using the slope of a plot of ln (P) vs ($1/T$). The heats of adsorption were ~12 kJ/mol at low surface coverage and

leveled off to ~8 kJ/mol at higher surface coverages. The high values of heat of adsorption at low surface coverage can be attributed to the adsorption of H_2 on the more energetic sites on graphene. Defect sites and edge sites (i.e., armchair and zigzag edge sites) are strong sites for adsorption. The heat of adsorption (~8 kJ/mol) on graphene at high coverages is clearly higher than that of H_2 on microporous carbons such as activated carbon (~5 kJ/mol).[33]

To understand the high capacity of graphene and the adsorption mechanism, Lifeng Wang studied the adsorption kinetics on graphene and compared it with other carbons (super-activated carbons AX-21 and Maxsorb, templated carbon, and CNTs). The kinetics of uptake were studied by increasing the pressure in steps and following the fractional completion versus time during each step. Figure 19 shows the adsorption kinetics of hydrogen on graphene and other carbons at ~ 6 MPa final pressure and 25 ^{o}C. It is seen that the adsorption rates on graphene were clearly slower than on all other carbons. For all other carbons, the adsorption was completed within 10 min. While for graphene, the completion for total uptake took ~ 25 min. This indicates a unique hydrogen uptake process that occurs on graphene. A detailed comparison of adsorption kinetics on graphene and AX-21 carbon at various pressures was carried out further. As shown in Figure 20, the adsorption on AX-21 at all pressures was completed within 10 min. For graphene, the completion time ranged from 12 to more than 30 min, and the kinetics became slower with the increase in pressure. The difference between graphene and AX-21 is more clearly shown by comparing their fractional uptake completion during individual pressure steps (Figure 21). Within 0.5 min, over 90 % completion was accomplished on AX-21 while the remaining 10 % was completed in less than 10 min (these discrepancies from instant adsorption are also observed in a blank tube and are caused by expansive cooling and reheating in the apparatus as well as pressure gauge response time). This can be understood because the fast adsorption of H_2 on AX-21 was via van der Waals interactions. In 0.5 min, the adsorption on graphene had completion fractions of 76 % at 2.0 MPa, 53 % at 6.3 MPa and 33 % at 7.9 MPa. The slower adsorption rates on graphene compared with AX-21 and other carbons indicate that a chemical process may be involved in addition to physical adsorption.

Previous theoretical studies showed that the edge sites or structural vacancies on graphene could dissociate H_2 into H atoms.[34-37] Despite their activities, free edge sites (zigzag and armchair sites) and their joint corner sites could be stable enough to remain free (i.e. not hydrogenated) at ambient temperature.[38,39] In order to gain further insight into the activities of graphene, the $H_2/D_2/HD$ isotope equilibrium reaction was employed (as explained in section 2.3.). The reaction $H_2 + D_2 \rightarrow 2HD$ ($K_{eq} \sim 3.5$) was measured as a function of completion vs. time at RT and a correction was added to the time at RT to account for the cooling process. In Figure 22 a first order rate is shown for both the graphene and Pt-doped AX-21 dissociation rates. Given the highly increased dissociation rates compared with AX-21 and the blank cell it is clear that graphene and Pt-doped carbon have similar hydrogen dissociation capabilities. It is also clear that there is an additional hydrogen dissociation mechanism for graphene that was not observed by Ishikawa et al. for graphite.[32] To my knowledge, this is the first time this highly increased catalytic activity for graphene (as compared to all other carbons) has been observed experimentally. Graphene sample was provided by Lifeng Wang.

To gain insight into possible binding sites and the relation between adsorption and hydrogen dissociation, I also measured temperature programmed desorption (TPD) spectra for graphene (as explained in section 2.3.). These spectra were taken after time at RT of 0.5 min, 1.5 min and 2 h. As shown in Figure 23, TPD for time at RT of 2 h adsorption shows a clear peak with isotopic effects above RT (hydrogen comes out in higher concentration than is present in the system). At only 1.5 min at RT this peak disappears and a new peak (assumed to be hidden) becomes apparent at lower temperature. At 0.5 min at RT only the peaks due to physically adsorbed species seem to be present. Previous work on hydrogen spillover suggests that reverse spillover and surface recombination of H/D will be the two probable methods for hydrogen desorption.[41] I have assigned the peak at higher temperatures to surface recombination due to isotopic effects (i.e. the lightest species are in greatest concentration). A blank TPD and plain AX-21 showed no peaks except the typical rise in hydrogen when approaching the degas temperature (starting around 200 ^{o}C) and the physical adsorbed hydrogen during initial heating for AX-21. TPD for AX-21 is provided (Supporting Figure S3).

The recombination and subsequent desorption is inherently measured in the $H_2/D_2/HD$ experiment showing that the bond formed between these most active graphene dissociation sites and hydrogen is very weak. Further the reaction rate shown here for dissociation (Figure 22) is faster than the completion rate for hydrogen uptake. This shows that the sites responsible for hydrogen dissociation are not the only sites increasing the hydrogen storage. A degas temperature of 823 K also shows that effective sites are stable at high temperatures. Theoretical and experimental studies suggest that a functional on the graphene (the zig-zag edge) is the most reactive site and would be capable of dissociating hydrogen.[36,38] This may be able to explain the difference between adsorption and the hydrogen dissociation rates. Other studies suggesting direct dissociation on the basal plane may be able to explain the slow adsorption rates as an alternative to a possible spillover mechanism.[42] The lack of studies on other functional groups indicate they should not be ruled out, including the possibility of sodium implanted into the carbon lattice or as a salt with carboxylic groups on the edges. However, further experiments are warranted for understanding the hydrogen adsorption sites present on graphene, and the effect of oxygen and sodium.

Conclusions

In summary, hydrogen catalytic properties of graphene have been studied and compared with a diverse collection of carbon materials. Graphene shows a unique hydrogen dissociation process that could potentially lead to increased storage capacity. The dissociation of hydrogen on graphene has been observed experimentally for the first time. I have also shown that the hydrogen dissociation rate is significantly faster than the adsorption rate as observed by Lifeng Wang. This leads me to conclude that the most active sites for dissociation are not the only sites where the enhanced adsorption occurs. The slow adsorption rates and TPD results show adsorption mechanism differences in graphene compared to activated carbon and demonstrate the unique hydrogen catalytic capabilities of graphene.

Acknowledgment. This work was supported by funding from NSF under grant CBET-0753008.

References

1. Novoselov KS, Geim AK, Morozov SV, Jiang D, Zhang Y, Dubonos SV, Grigorieva IV, Firsov AA. Electric field effect in atomically thin carbon films. Science. 2004;306:666-669.
2. Stankovich S, Dikin DA, Dommett GHB, Kohlhaas KM, Zimney EJ, Stach EA, Piner RD, Nguyen ST, Ruoff RS. Graphene-based composite materials. Nature. 2006;442:282-286.
3. Kim KS, Zhao Y, Jang H, Lee SY, Kim JM, Kim KS, Ahn JH, Kim P, Choi JY, Hong BH. Large-scale pattern growth of graphene films for stretchable transparent electrodes. Nature. 2009;457:706-710.
4. Choucair M, Thordarson P, Stride JA. Gram-scale production of graphene based on solvothermal synthesis and sonication. Nature Nanotech. 2009;4:30-33.
5. Li XL, Wang XR, Zhang L, Lee SW, Dai HJ. Chemically derived, ultrasmooth graphene nanoribbon semiconductors. Science. 2008;319:1229-1232.
6. Geim AK, Novoselov KS. The rise of graphene. Nature Mater. 2007;6:183-191.
7. Zhang Y, Guo L, Wei S, He Y, Xia H, Chen Q, Sun HB, Xiao FS. Direct imprinting of microcircuits on graphene oxides film by femtosecond laser reduction. Nano Today. 2010;5:15-20.
8. Sofo JO, Chaudhari AS, Barber GD. Graphane: a two-dimensional hydrocarbon. Phys. Rev. B. 2007;75:153401.
9. Dimitrakakis GK, Tylianakis E, Froudakis GE. Pillared Graphene: A New 3-D Network Nanostructure for Enhanced Hydrogen Storage. Nano Lett. 2008;8:3166-3170.
10. Lin Y, Ding F, Yakobson BI. Hydrogen storage by spillover on graphene as a phase nucleation process. Phys. Rev. B. 2008;78:041402.
11. Xu WC, Takahashia K, Matsuoa Y, Hattoria Y, Kumagaia M, Ishiyamab S, Kanekoc K, Iijima S. Investigation of hydrogen storage capacity of various carbon materials. Int. J. Hydrogen Energy. 2007;32: 2504–2512.
12. Miller MA, Wang CY, Merrill GN. Experimental and Theoretical Investigation Into Hydrogen Storage via Spillover in IRMOF-8. J. Phys. Chem. C. 2009;113:3222-3231.
13. Zhao D, Yuan D, Zhou HC. The current status of hydrogen storage in metal–organic frameworks. Energy Environ. Sci. 2008;1:222–235.
14. Wang L, Yang RT. New sorbents for hydrogen storage by hydrogen spillover – a review. Energy Environ. Sci. 2008;1:268–279.
15. Frost H, Duren T, Snurr RQ. Effects of Surface Area, Free Volume, and Heat of Adsorption on Hydrogen Uptake in Metal–Organic Frameworks. J. Phys. Chem. B. 2006;110:9565-9570.
16. Frost H, Snurr RQ. Design Requirements for Metal-Organic Frameworks as Hydrogen Storage Materials. J. Phys. Chem. C. 2007;111:18794-18803.
17. Chung TCM, Jeong Y, Che Q, Kleinhammes A, Wu Y. Synthesis of Microporous Boron-Substituted Carbon (B/C) Materials Using Polymeric Precursors for Hydrogen Physisorption. J. Am. Chem. Soc. 2008;130:6668-6669.
18. Ma LP, Wu ZS, Li J, Wu ED, Ren WC, Cheng HM. Hydrogen adsorption behavior of graphene above critical temperature. Inter. J. Hydrogen Energy. 2009;349:2329-2332.
19. Ghosh A, Subrahmanyam KS, Krishna KS, Datta S, Govindaraj A, Pati SK, Rao CNR. Uptake of H_2 and CO_2 by Graphene. J. Phys. Chem. C. 2008;112:15704-15707.

20. Srinivas G, Zhu Y, Piner R, Skipper N, Ellerby M, Ruoff R. Synthesis of graphene-like nanosheets and their hydrogen adsorption capacity. Carbon, 2010;48:630-635.
21. Elias DC, Nair RR, Mohiuddin TMG, Morozov SV, Blake P, Halsall MP, Ferrari AC, Boukhvalov DW, Katsnelson MI, Geim AK, Novoselov KS. Control of Graphene's Properties by Reversible Hydrogenation: Evidence for Graphane. Scinece. 2009;323:610-613.
22. Balog R, Jorgensen B, Wells J, Lagsgaard E, Hofmann P, Besenbacher F, Hornekar L. Atomic Hydrogen Adsorbate Structures on Graphene. J. Am. Chem. Soc. 2009;131:8744-8745.
23. Jun S, Joo S. H, Ryoo R, Kruk M, Jaroniec M, Liu Z, Ohsuna T, Terasaki O. Synthesis of New, Nanoporous Carbon with Hexagonally Ordered Mesostructure. J. Am. Chem. Soc. 2000;122:10712-10713.
24. Ma Z, Kyotani T, Liu Z, Terasaki O, Tomita A. Very High Surface Area Microporous Carbon with a Three-Dimensional Nano-Array Structure: Synthesis and Its Molecular Structure. Chem. Mater. 2001;13:4413-4415.
25. Lachawiec J, Yang RT. Isotope Tracer Study of Hydrogen Spillover on Carbon-Based Adsorbents for Hydrogen Storage. Langmuir. 2008;24:6159-6165.
26. Gaslain FOM, Parmentier J, Valtchev VP, Patarin J. First zeolite carbon replica with a well resolved X-ray diffraction pattern. Chem. Commun. 2006;991-993.
27. Wang L, Yang RT. Hydrogen Storage Properties of Carbons Doped with Ruthenium, Platinum, and Nickel Nanoparticles. J. Phys. Chem. C. 2008;112:12486-12494.
28. Chae H, Siberio-Perez DY, Kim J, Go Y, Eddaoudi M, Matzger A, O'Keeffe M, Yaghi OM. A route to high surface area, porosity and inclusion of large molecules in crystals. Nature, 2004;427:523-527.
29. Haas MK, Zielinski JM, Dantsin G, Coe CG, Pez GP, Cooper AC. Tailoring singlewalled carbon nanotubes for hydrogen storage. J. Mater. Res. 2005;20:3214-3223.
30. Li Y, Yang RT. Hydrogen Storage on Platinum Nanoparticles Doped on Superactivated Carbon. J. Phys. Chem. C. 2007;111:11086-11094.
31. Lachawiec AJ, DiRamondo TR, Yang RT. A robust volumetric apparatus and method for measuring high pressure hydrogen storage properties of nanostructured materials. Rev. Sci. Instru. 2008;79:063906–063917.
32. Ishikawa Y, Austin LG, Brown DE, Walker Jr PL. Chemistry and Physics of Carbon (eds.: Walker PL, Thrower PA). Marcel Dekker, Inc. New York and Basel. 1975, p. 39-108.
33. Bénard P, Chahine R. Determination of the Adsorption Isotherms of Hydrogen on Activated Carbons above the Critical Temperature of the Adsorbate over Wide Temperature and Pressure Ranges. Langmuir. 2001;17:1950-1955.
34. Arboleda NB, Kasai H, Nakanishi H, Dino WA, Sugimot T. Scattering and dissociative adsorption of H_2 on the armchair and zigzag edges of graphite. J. Appl. Phys. 2004;96:6331-6336.
35. Sha X, Jackson B. The Location of Adsorbed Hydrogen in Graphite Nanostructures. J. Am. Chem. Soc. 2004;126:13095-13099.
36. Jiang DE, Sumpter BG, Dai S. Unique chemical reactivity of a graphene nanoribbon's zigzag edge. J. Chem. Phys. 2007;126:134701-134706.
37. Lei Y, Shevlin SA, Zhu W, Guo ZX, Hydrogen-induced magnetization and tunable hydrogen storage in graphitic structures. Phys. Rev. B. 2008;77:134114.

38. Radovic LR, Bockrath B. On the Chemical Nature of Graphene Edges: Origin of Stability and Potential for Magnetism in Carbon Materials. J. Am. Chem. Soc. 2005;127:5917-5927.
39. Radovic LR. Active Sites in Graphene and the Mechanism of CO_2 Formation in Carbon Oxidation. J. Am. Chem. Soc. 2009;131:17166-17175.
40. Stuckert NR, Wang L, Yang RT. Characteristics of Hydrogen Storage by Spillover on Pt-Doped Carbon and Catalyst-Bridged Metal Organic Framework. Langmuir. 2010;26:11963-11971.
41. Conner Jr WC, Falconer JL. Spillover in Heterogeneous Catalysis. Chem. Rev. 1995;95:759-788.
42. McKay H, Wales DJ, Jenkins SJ, Verges JA, de Andres PL. Hydrogen on graphene under stress: Molecular dissociation and gap opening. Physical Review B. 2010;81:075425.

Figure captions

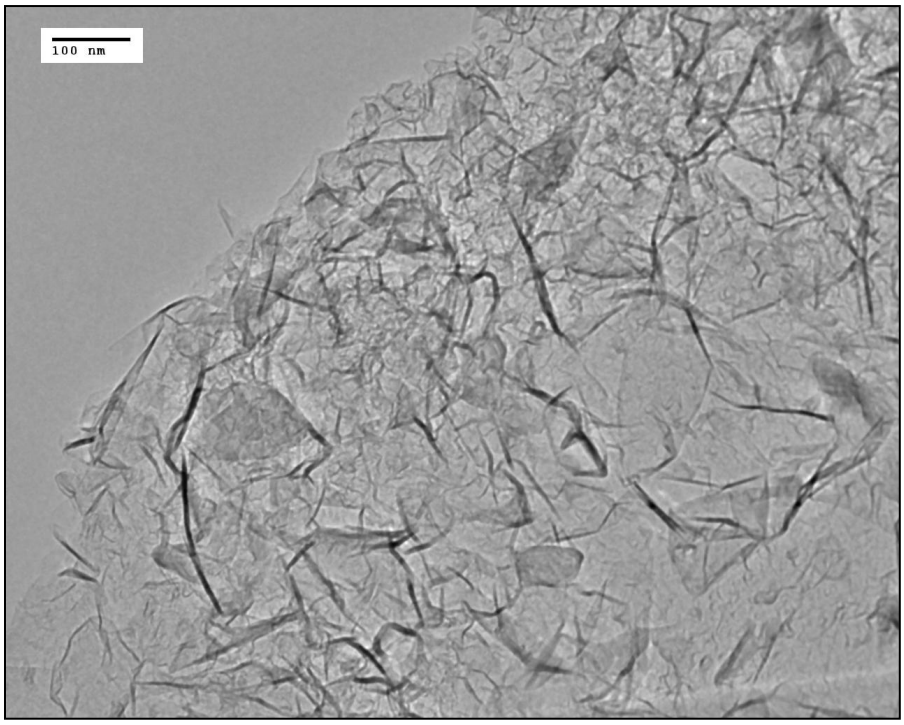

Figure 14. TEM image of graphene. Obtained by Lifeng Wang.

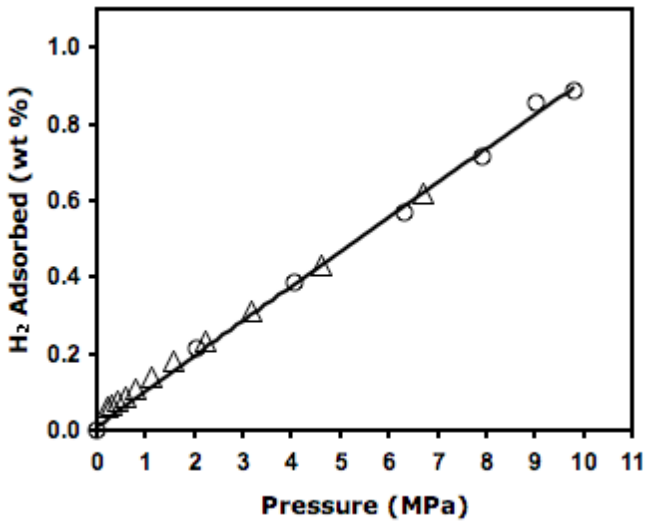

Figure 15. High-pressure hydrogen isotherms on graphene at 25 ^{o}C: adsorption (○) and desorption (△).Obtained by Lifeng Wang.

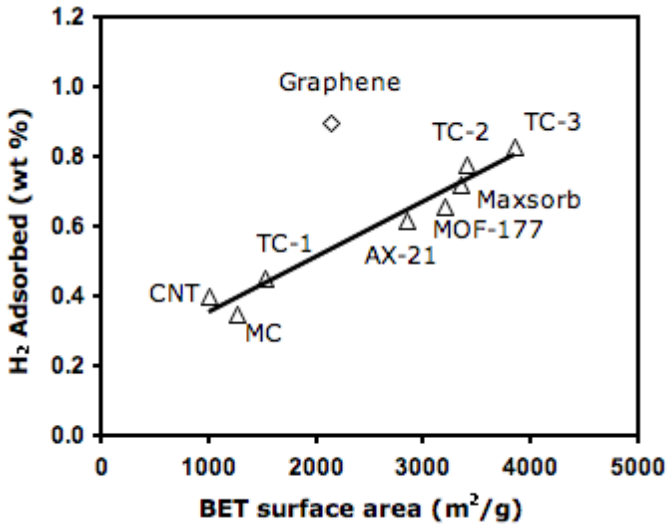

Figure 16. Relationship between the BET surface area of carbons and their storage capacities at 25 ^{o}C and 10 MPa. Obtained by Lifeng Wang.

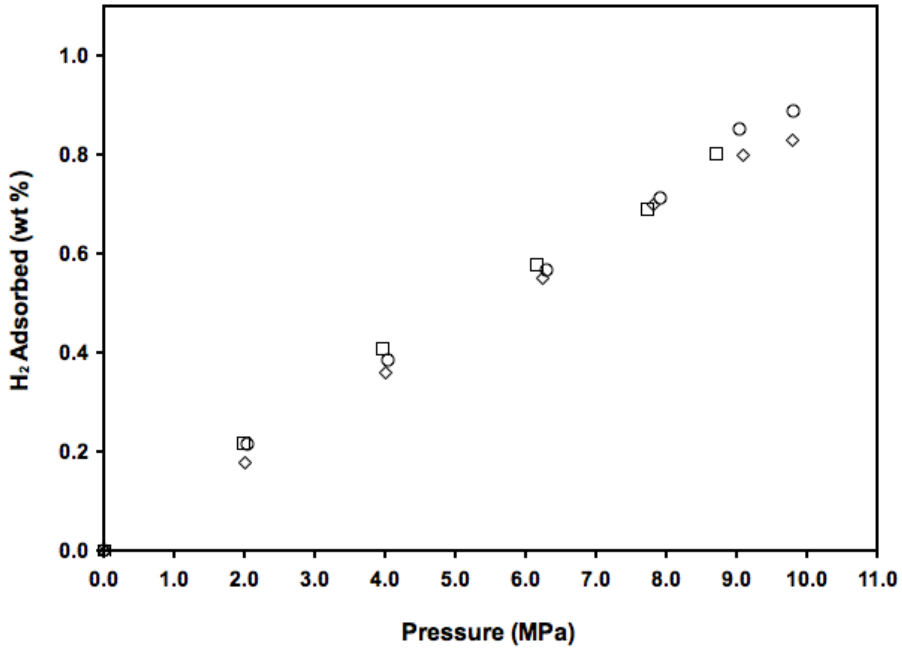

Figure 17. Three consecutive hydrogen adsorption isotherms on graphene in 3 adsorption-desorption cycles at 25 ^{o}C. Obtained by Lifeng Wang.

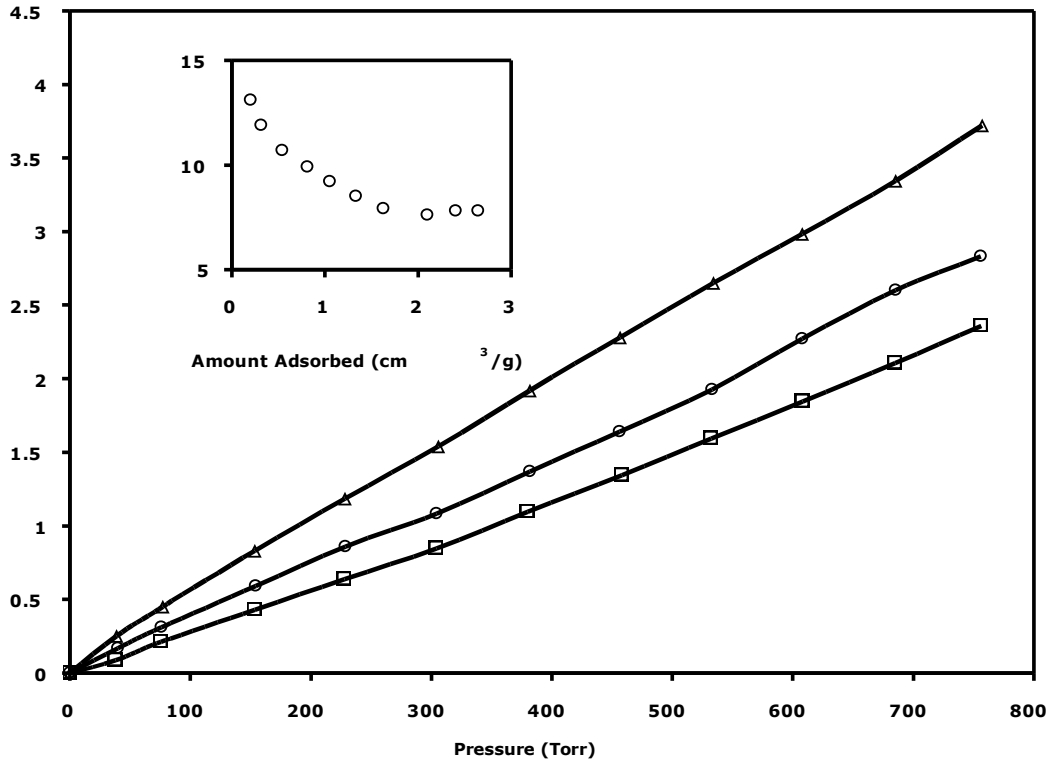

Figure 18. Hydrogen isotherms on graphene at 0 °C (△), 25 °C (○), 50 °C (□); Heats of adsorption (inset). Obtained by Lifeng Wang.

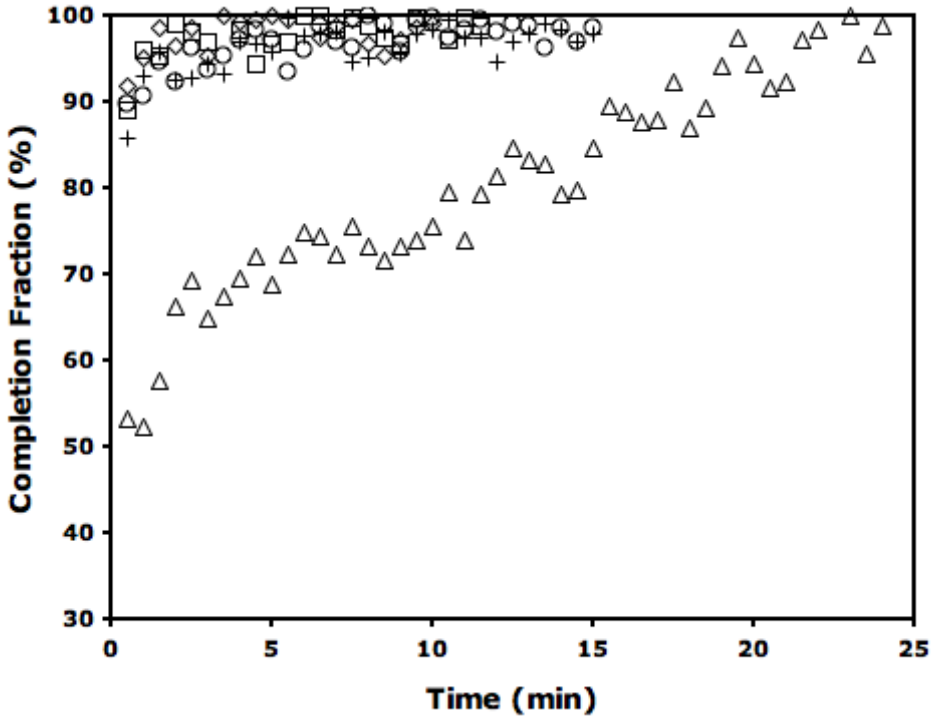

Figure 19. Fractional completion for hydrogen uptake at 25 ^{o}C on AX-21 (×), Maxsorb (○), CNT (□), templated carbon (+) and graphene (△) at ~ 6 MPa end pressure. Obtained by Lifeng Wang.

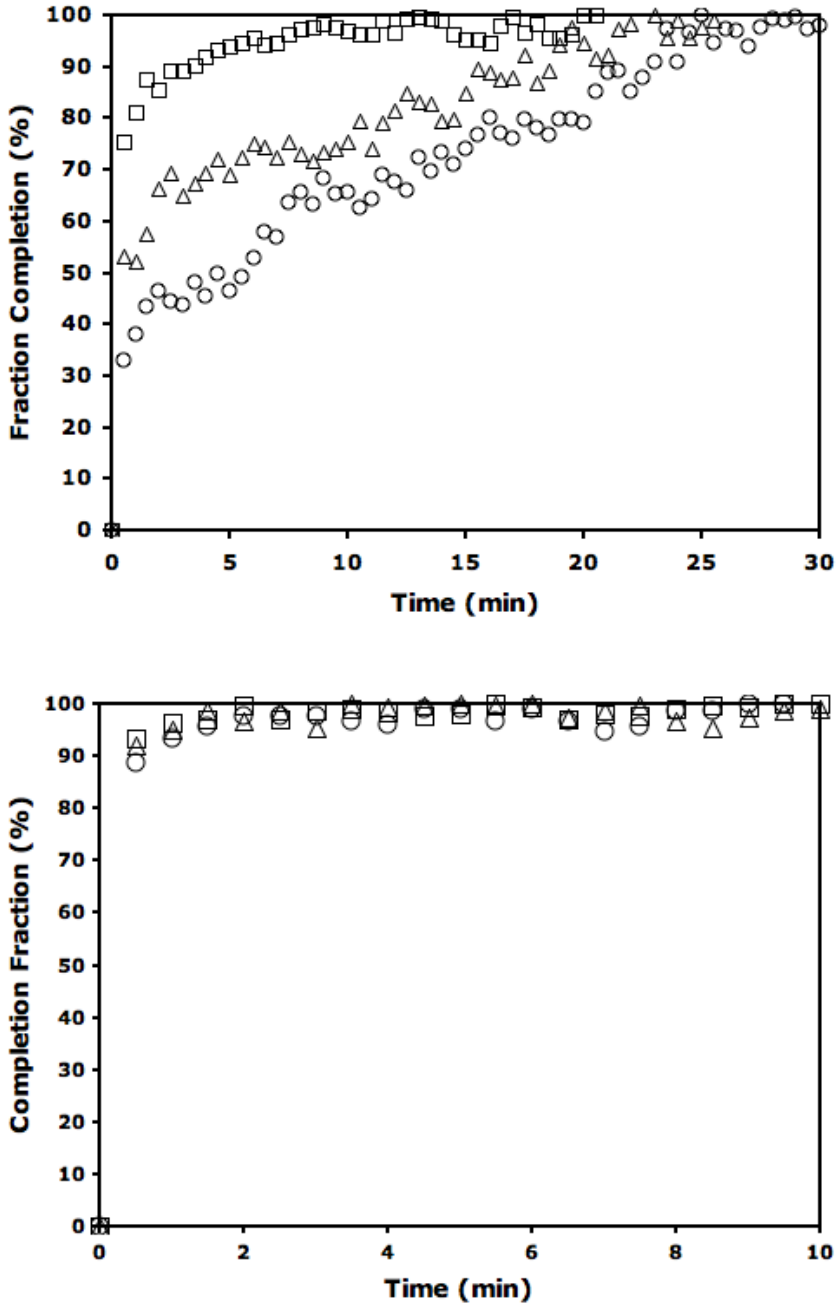

Figure 20. Adsorption fraction at 25 ^{o}C on graphene (A) and AX-21 carbon (B) during each pressure ramp step at final pressures of: ~2 MPa (□), 6.2 MPa (△) and 7.9 MPa (○). Obtained by Lifeng Wang.

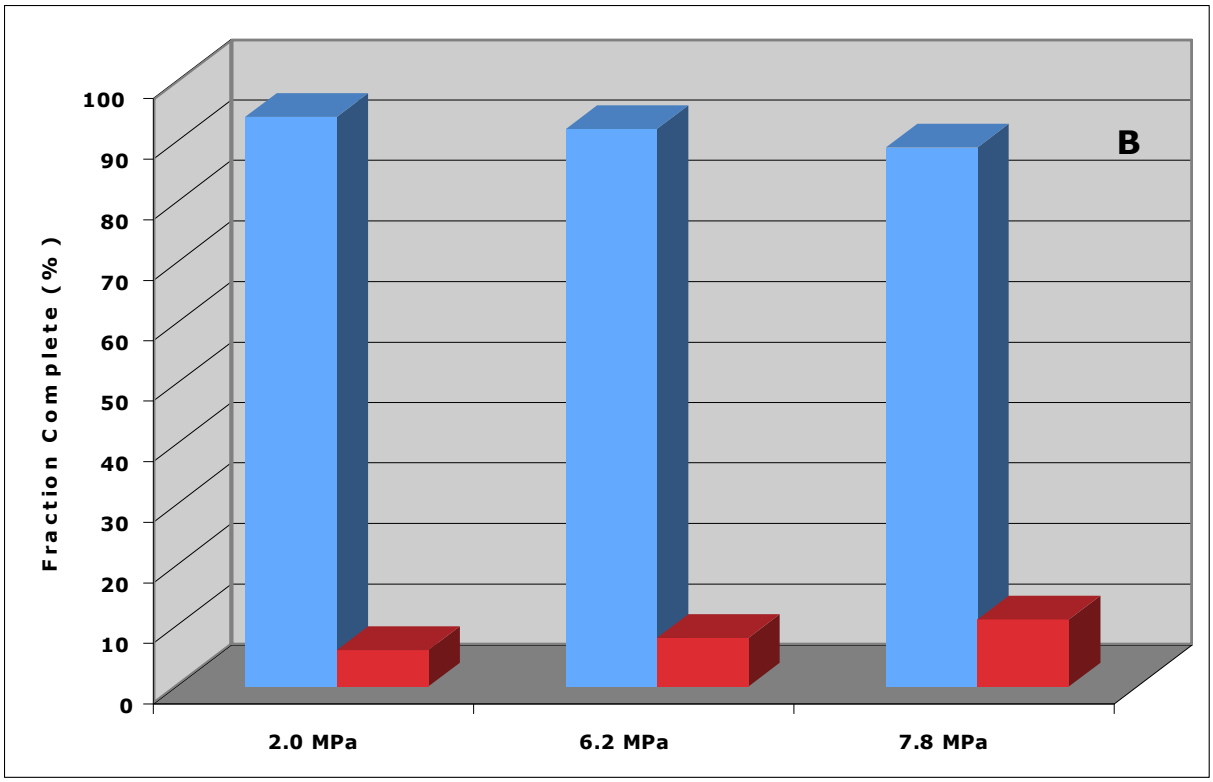

Figure 21. Fraction completion for adsorption on graphene (A) and AX-21 carbon (B) during each pressure ramp step at final pressures of 2, ~6.2 and ~7.9 MPa. Blue (left) column: Fraction completed within 0.5 min; Red (right) column: fraction completed after 0.5 min. Obtained by Lifeng Wang.

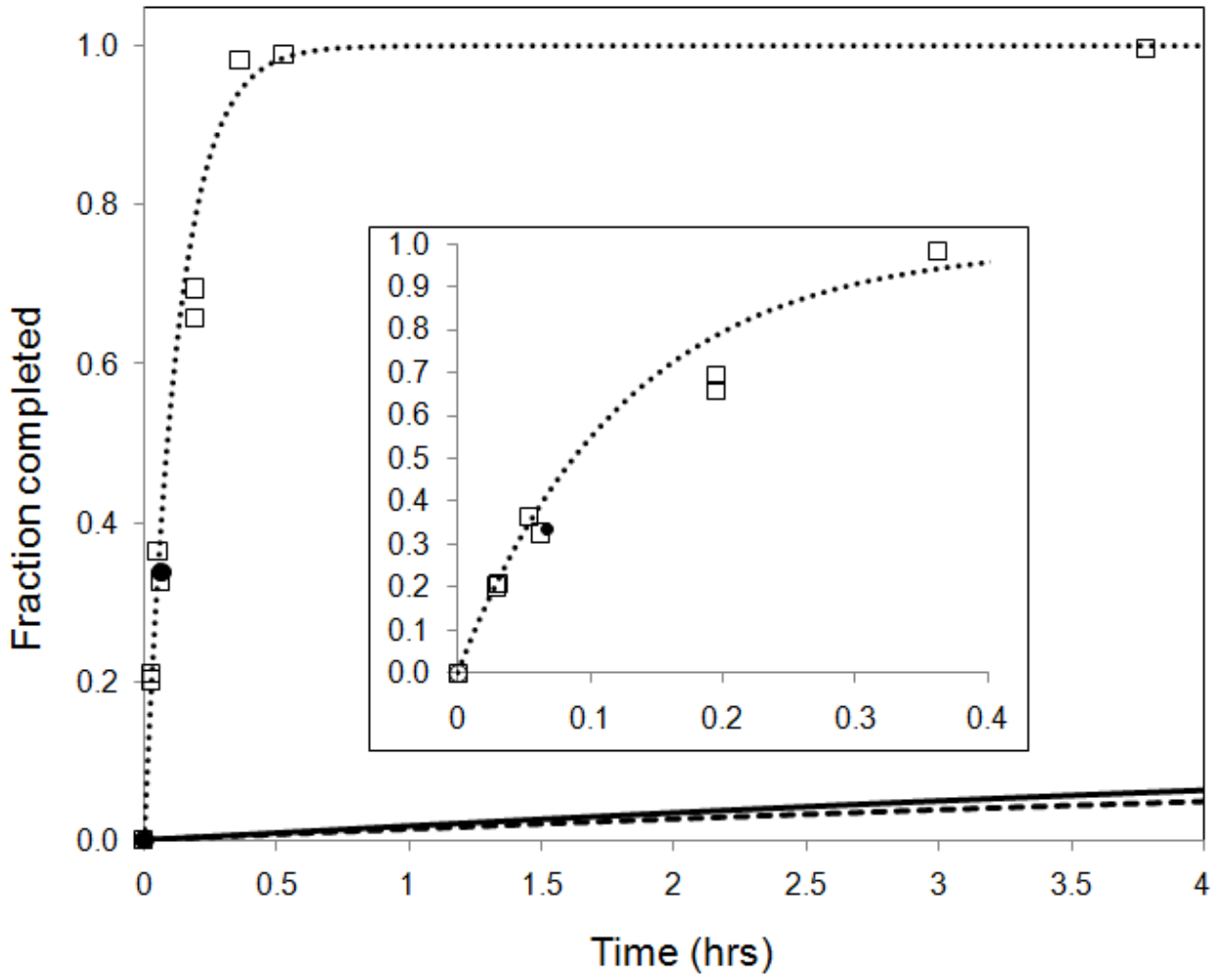

Figure 22. $H_2 + D_2 \rightarrow 2HD$ reaction rates at 25 °C. Graphene (□) (time at RT and extrapolated to account for cooling time), AX-21 (—), Graphene after pre-treatment at 550 °C (●), Pt/AX-21 (△), blank cell (– – –) and fit assuming reversible 1st order reaction rate(…).

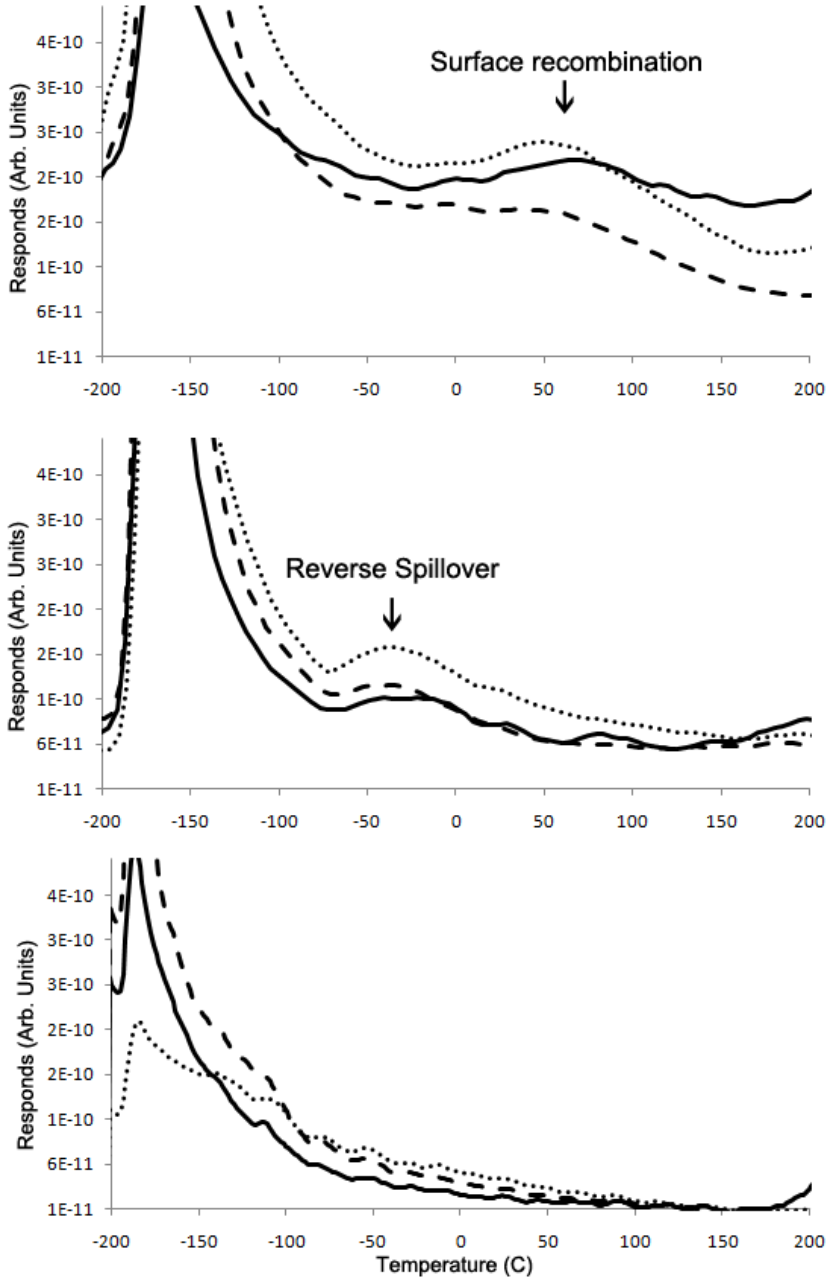

Figure 23. The TPD spectra for graphene are shown for 2 h (top), 1.5 min (middle) and 0.5 min (bottom) exposure time to a H_2/D_2 mix at 25 ^{o}C and 1.6 MPa. H_2 (—), D_2 (– – –) and HD (…) are shown for all spectra. Evolution of two different peaks can be seen (one possibly corresponding to reverse spillover and the other possibly to surface recombination of H atoms). High concentrations of physically adsorbed hydrogen are due to quenching while under high pressure.

Chapter 3: Effects of catalyst size on the hydrogen storage on Pt-doped IRMOF-8

Introduction

Storage is one of the key issues for the realization of fuel-cell powered vehicles using hydrogen as the energy carrier (1). Among candidate hydrogen storage adsorbents, metal-organic frameworks (MOFs), a class of porous materials constructed by coordinate bonds between multidentate ligands and metal atoms or small metal-containing clusters, have attracted increasing attentions due to their lightweight, high surface area and porosities, and adjustable structures (2-7). Significant storages on MOFs with high surface area have been reported. For example, MOF-177 with a high Langmuir surface area of 5640 m^2/g can store the highest 7.5 wt % H_2 at 77 K and 7 MPa (8,9). The storage capacities of fully activated MIL-101 (Langmuir surface area 5900 m^2/g) at 77 K are 3.75 wt % at 2 MPa and 6.1 wt % at 8 MPa (10,11). It is noted that, these significant storage capacities on MOFs were achieved at 77 K. When the temperature was room temperature, the storage capacities were much lower. This can be understood that the hydrogen adsorption on MOFs is mostly due to weak van der Waals interactions. However, for practical application, high storage capacity at room temperature is desired.

To improve the hydrogen storage on adsorbents at room temperature, one effective way is using hydrogen dissociation followed by spillover. Presently, more than 100 papers published by ~ 40 groups have reported enhancements in hydrogen adsorption by spillover at ambient temperatures demonstrating this technique (12). Hydrogen spillover can be defined as the dissociative chemisorption of hydrogen on metal nanoparticles, and subsequent migration of hydrogen atoms onto adjacent surfaces of a receptor via spillover and surface diffusion (13-18). Evidence of atomic hydrogen spillover was first observed during studies of ethylene hydrogenation (19) and later observed in the reduction of transition metal oxide with Pt catalyst and hydrogen uptake on transition metals supported on carbon by Khoobiar and Boudart (13,20,21). Direct evidence of spillover of atomic hydrogen from Pt to carbon (22,23), from Pt to glass (24) and from Au to TiO_2 (25) at room temperature has been recently reported.

Theoretical studies have illustrated the facile pathway for spillover from a Pt particle onto a graphene basal plane is via physisorption of H atoms (26,27) and thermodynamically spillover can occur from both the free-standing metal clusters and from the receptor-supported metal clusters (28,29). The spillover storage capacities for different MOFs and COF-1 have been calculated by Ganz and coworkers (30).

Hydrogen spillover on MOFs can be induced by building carbon bridges between the dissociation source (Pt/AC catalyst) and MOFs (31-36), catalyst encapsulation (37) or direct doping of dissociation metals (Pt, Pd, Ni) on MOFs (38-41). The factors that affect hydrogen spillover on MOFs by bridge building have been discussed (42). It is suggested that the ideal situation for hydrogen spillover on bridged-MOFs is where all the individual catalyst and MOF receptor particles were "bridged". Direct doping of dissociation metals on MOFs was recently developed. Enhanced hydrogen storages at room temperature have been observed on Pd-doped MIL-100 (38), Pd-doped Redox-active MOF (39), Pt-doped MOF-177 (40) and Ni-doped MIL-101 (41). It is known that direct doping resulted in the dispersion of metal particles on MOFs, and physical and energy barriers for transfer of hydrogen atoms from one material to another exist during spillover. Thus the dispersion and the particle size of the metal on MOFs will affect the spillover and thereby the hydrogen storage on MOFs. To our knowledge, the studies of catalyst dispersion and particle size effects on hydrogen storage on MOFs have not been reported. In this work, Lifeng Wang synthesized a series of Pt-doped IRMOF-8 samples through the metal organic chemical vapor deposition and I studied the Pt dispersion and particle size effects on the hydrogen spillover mechanism.

Experimental Methods

Synthesis

(1) Synthesis of IRMOF-8: Typically, 1.19 g of $Zn(NO_3)_2{\cdot}6H_2O$ (freshly opened) and 0.43 g of 2,6-naphtalenedicarboxylic acid were dissolved in 40 mL of diethylformamide (DEF) during vigorous stirring at room temperature (Yaghi and Tsao 43,44). The DEF solution was heated to 393 K for 20 hours and then cooled to room temperature. The white product was collected by filtering and four thorough washings with DMF (DEF?). The product was exchanged by $CHCl_3$ 4 times, and then degassed at 423 K for 12 h.

(2) Synthesis of Pt-doped IRMOF-8 via chemical vapor deposition (CVD). Pt was doped on IRMOF-8 by chemical vapor deposition of a volatile platinum precursor (Trimethyl)methylcyclopentadienyl platinum (IV). The MOF crystals were ground for 0.5 hr before CVD. The grounded MOFs and platinum precursor were placed in a tube separated by a glass frit and degassed to a vacuum of < 10 μmHg at 273 K. After that, the degassing was stopped and the temperature was increased to 303 K and kept at 303 K for 1 hr. The vacuum of this system was renewed each hour for 6 cycles then stayed for another 6 hrs. During this procedure, an off-white composite was yielded and designated as Pt/IRMOF-8-1. For Pt/IRMOF-8-2 sample, the temperature was kept at 308 K and the vacuum was renewed each hour for 4 cycles then stayed for another 8 h. For Pt/IRMOF-8-3 sample, the temperature was kept at 318 K and the vacuum was renewed for 1 cycle then stayed 11 hrs. These three samples were reduced in a hydrogen atmosphere at 423 K overnight, and then purged with flowing helium.

Characterization

Powder X-ray diffraction (XRD) data were recorded on a Rigaku Miniflex diffractometer at 30 kV, 15 mA for Cu Kα (λ = 0.1543 nm) radiation, with a step size of 0.02° in 2θ. X-ray photoelectron spectroscopy was recorded on a Kratos Axis ultra XPS spectrometer. Nitrogen adsorption and low-pressure H_2 adsorption isotherms (0-1 atm) were measured with a standard static volumetric technique (Micromeritics ASAP 2020). Hydrogen adsorption at 298 K and pressures greater than 0.1 MPa and up to 10 MPa was measured using a static volumetric technique with a specially designed Sieverts-type apparatus. The apparatus was previously tested and proven to be accurate through calibration by using $LaNi_5$, AX-21, zeolites, and MOFs at 298 K (45). Accuracy is determined here to be 0.6wt% at 100atm for a 200mg sample. 120-200 mg of sample was used for each high-pressure isotherm measurement in this study. Temperature Programmed Desorption (TPD) was used to identify high energy binding. A 100mg sample was dosed with hydrogen for a period of time and cooled to 77K under pressure. Excess gas was vacuumed off and the sample was heated at a constant rate while the evolved gas was monitored with a mass spectrometer (MS).

Results and Discussion

Powder X-ray diffraction patterns of IRMOF-8 and Pt/IRMOF-8 samples are shown in Figure 24. The plain IRMOF-8 (Fig. 1D) shows typical peaks at 2θ = 6.3°, in good agreement with previous reports (shall I put reference here?). After doping with Pt, the XRD patterns of Pt/IRMOF-8-1, Pt/IRMOF-8-2 and Pt/IRMOF-8-3 samples all exhibit the same peaks as those of plain IRMOF-8 although the peak intensity slightly decreases. This indicates that the microstructure of IRMOF-8 was retained after the doping treatments. Furthermore, the Pt/IRMOF-8 samples all show two peaks at ca. 40° (111) and 46 ° (200) characteristic of the metallic platinum metal. These results confirm that Pt metals have been successfully doped on IRMOF-8 by applying the CVD method. It is noted that the peaks corresponding to Pt became narrower from Pt/IRMOF-8-1 to Pt/IRMOF-8-2 and Pt/IRMOF-8-3. This indicates the Pt size increased with the order of Pt/IRMOF-8-1, Pt/IRMOF-8-2 and Pt/IRMOF-8-3.

Nitrogen adsorption was further employed to evaluate the porosity of plain IRMOF-8 and the doped samples. As shown in Figure 25, the isotherms of IRMOF-8 and Pt/IRMOF-8 samples all exhibit the typical s curve, thus revealing the presence of microporosity in the samples. The BET surface area and pore volume of plain IRMOF-8 are 1430 m^2/g and 0.69 cm^3/g, respectively. These textural properties are in agreement with previous report.[36,37] After doping Pt on IRMOF-8, the BET surface areas and pore volumes of Pt/IRMOF-8-1, Pt/IRMOF-8-2 and Pt/IRMOF-8-3 samples were reduced to 1175, 1071, 1014 m^2/g, 0.59, 0.53 and 0.55 cm^3/g, respectively. The BET surface area and pore volume of Pt/IRMOF-8-1, Pt/IRMOF-8-2 and Pt/IRMOF-8-3 are lower than that of plain IRMOF-8. This is most likely due to the increased weight and micropore blocking caused by the doped Pt particles.

High-pressure hydrogen isotherms at 298 K for plain IRMOF-8, Pt/IRMOF-8-1, Pt/IRMOF-8-2 and Pt/IRMOF-8-3 samples are presented in Figure 26. As shown in Figure 26, IRMOF-8 has a hydrogen storage capacity of ~0.44 wt% at 298 K and 10 MPa. After doping Pt on IRMOF-8, the hydrogen uptakes on Pt/IRMOF-8-1, Pt/IRMOF-8-2 and Pt/IRMOF-8-3 at 10 MPa were enhanced to 0.85, 0.67 and 0.49 wt %, respectively. It can be seen that all the Pt/IRMOF-8 samples exhibit higher hydrogen adsorption capacities than the plain IRMOF-8 sample up to 10 MPa. The enhanced hydrogen storage capacity should not be attributed to the differences in surface area because the Pt/IRMOF-8 samples have lower surface areas than that of plain

IRMOF-8, as evident from nitrogen adsorption results. The enhancement of hydrogen storage is due to the spillover of atomic hydrogen from Pt particle to IRMOF-8. The Ru, Pt, Pd and Ni metals are known as hydrogen dissociation sources, and the enhanced hydrogen storage on various supports by doping these metals have been well observed (shall I put references here?).

It is noted that, in our case, the hydrogen storage capacities follow the order of Pt/IRMOF-8-1 > Pt/IRMOF-8-2 > Pt/IRMOF-8-3. The maximum hydrogen uptake reached 0.85 wt % at 10 MPa on Pt/IRMOF-8-1. The reversibility on Pt/IRMOF-8-1 was also evaluated by measuring the desorption branch down to 1 atm. It can be seen the desorption branch nearly followed the adsorption branch, although there appeared to be a slight hysteresis. After evacuation to a pressure of 1 Pa for 12 h at 298 K, and total desorption occurred. The second adsorption isotherm was nearly in agreement with the first adsorption isotherm. In comparison with plain IRMOF-8, it is remarkable that the hydrogen adsorption amount of Pt/IRMOF-8-1 has been enhanced by a factor of 1.9. However, the enhancement factors are only 1.5 for Pt/IRMOF-8-2 and 1.1 for Pt/IRMOF-8-3.

The variation in the storage capacities of Pt/IRMOF-8 samples indicates the difference existing in the samples. The Pt/IRMOF-8 samples were characterized by TEM and chemisorption analysis. TEM images of Pt/IRMOF-8-1, Pt/IRMOF-8-2 and Pt/IRMOF-8-3 samples are shown in Figure 27. For each sample, the black spots of Pt particles can be observed on the surface of IRMOF-8. These results further confirm Pt has been successfully doped on MOF support. The Pt particle size of Pt/IRMOF-8-1 and Pt/IRMOF-8-2 is smaller than that of Pt/IRMOF-8-3. As TEM only gives limited information of the Pt dispersion on the whole sample, hydrogen chemisorption was further used. It is known that the Benson–Boudart method is a good assessment for the dispersion of metals on supports. From the adsorbed amount of hydrogen extrapolated to zero pressure, the dispersion of Pt metal on IRMOF-8 can be calculated. Figure 28 shows the H_2 adsorption isotherms on Pt/IRMOF-8-1, Pt/IRMOF-8-2, and Pt/IRMOF-8-3 at 298 K. It is obvious that the dispersion of Pt on MOF follows the order of Pt/IRMOF-8-1 > Pt/IRMOF-8-2 > Pt/IRMOF-8-3. These results indicate high dispersion and small size of Pt particles facilitate spillover on MOFs and in turn the storage capacity. This is in agreement with the XRD and TEM results. It is noted that the effects on spillover storage on MOF also agree

with the previous studies on carbon receptors. Tsao et al. impregnated activated carbon with Pt particles of ~1-2 nm and achieved an enhancement factor of 3 (46). Arenillas et al. measured the hydrogen adsorption on carbon nanospheres doped with different loadings of Ni and found that the storage capacity of doped carbon was enhanced by a factor of 1.4 to 2.3 (47). The highest storage capacity was obtained on Ni-doped carbon nanophere with the best Ni distribution and smaller Ni particle (5 nm). Tsai group found the uniformly distributed Ni nanoparticles (2.3 nm) tripled the hydrogen uptake on CNTs (48). Back et al. reported the hydrogen uptake on Pd-doped carbon nanofibers was 4 times larger than that on the un-doped carbon and attributed the enhancement to the smaller Pd particle (49). By considering the carbon nature of the linker of MOFs, it is reasonable to observe the similar effects of Pt size and dispersion on the storage capacity of MOF sample. Lab previous studies (50) showed that there is a limited area of influence for each particle due to diffusion resistance and lack of diffusion pathways. Thus particles with lower uneven dispersion can not affect the entire MOF support, and result in the dismissed spillover enhancement. The high dispersion and small size of Pt particles contribute to increased contacts with the MOF receptor

It is noted that the size of the doped metal is affected by many factors, including the type of metal, the doping/addition rate and loading amount of the metal precursor, and the treatment temperature and metal reduction method. In our case, for doping Pt via CVD method, the lower temperature provided a lower Pt precursor vapor concentration and more vacuum and doping cycles are favorable for the uniform interactions between precursor and MOFs. The highest doping temperature and only one vacuum and doping cycle resulted in the largest Pt size. This is similar to the effects of addition rate and concentration of H_2PtCl_6 on Pt dispersion on AX-21. However, further optimizing the doping conditions is still needed for a significant enhancement.

The TPD spectra detailed in Figure 29 show the spillover of hydrogen as previously observed on other metal doped supports[50,51], and additionally on our other work on templated carbon[49], activated carbon [41] and graphene (which does not need a metal dissociation source) [52]. In this figure, I show that if hydrogen is dosed then followed by dosing deuterium, then deuterium is desorbed first followed by hydrogen. I also took the time to reverse the procedure and show that this is independent of isotope.

One of the interesting features of the spectra in Figure 29 is the presence of a physically adsorbed peak at 135K (present on plain IRMOF-8 as shown in supporting figure ?) which seems to have a knee at 181K. I examined this further in Figure 30, where I lowered the dosing pressure to 25 torr and exposed only deuterium for 5 min (the figure shows both CVD doped IRMOF-8 and plain IRMOF-8). This illuminated 3 separate peaks. The first at 135K (the one responsible for the knee in Figure 29), saturates at very low pressure, indicating strong chemisorption and is not present on plain IRMOF-8. I infer this is also a binding site on the doped platinum. The second peak at 165K also saturates at very low pressure and is also not present on plain IRMOF-8. I can conclude that this peak is not spillover and is therefore a binding site on the doped platinum. The third and last peak seen at 200K decreases with dosing pressure and is also present on plain IRMOF-8, this is most likely the hydrogen adsorption site corresponding to the ZnO center of the IRMOF-8 structure. The interesting tail observed on the platinum doped sample is also of interest again. When a difference is taken, Figure 30 (C) shows the appearance of more platinum peaks.

We then compare these platinum peaks across single crystal spectra for platinum. TPD spectra from the (111)[53], (100)[54] and (110)[55] faces show that the most likely configuration is the (111) and (110) faces. Information gained from spectra of the (210) and (211) faces[56] show that while these are not responsible for the observed peaks, stepping and edging creates very different binding sites, that may contribute to the other partially obscured peaks. From the TEM observations, I can see that the particles (which are ~2nm) have the characteristics observed in our last paper [41], of containing both (111) and (110) faces. Here however, the lattice constant of IRMOF-8 does not match with the (111) surface, leaving it exposed. Building off our previous publication, I can start to see that unsaturated platinum surfaces (edges, corners, defects, etc.) are present in successful spillover adsorbents[41] and from other papers I can see that they are not present in unsuccessful spillover adsorbents[57]. While the dispersion of the metal still influences the storage capacity based purely on more efficient metal utilization and greater area of influence, the unsaturated sites are necessary to perform the spillover. This should align well with previous criticisms that observe the binding

energy from a single hydrogen atom on planar platinum is very strong, and supporting observations that smaller platinum is necessary to see any spillover amount[58].

Conclusions

In this work, a series of Pt-doped IRMOF-8 samples have been prepared via metal organic chemical vapor deposition. The catalyst size (Pt) was affected by the doping temperatures and doping cycles. The hydrogen storage studies showed the storage capacities via hydrogen spillover on Pt-doped IRMOF-8 samples have been enhanced by a factor 1.1 – 1.9 when compared to undoped IRMOF-8. Unfortunately, these results are statistical insignificant.

What is significant is the TPD results can confirm the existence of reverse spillover on the doped IRMOF-8. The comparison to other platinum surfaces from platinum isolated TPD peaks shows that smaller particles are necessary to create higher energy sites which are needed to perform spillover. This supports information originally uncovered by Konvalinka and Scholten on Pd/Carbon[51]. This contribution to the understanding of spillover is critical however and where applicable to hydrogen storage is irrelevant.

Acknowledgements. Department of Energy (DOE), A Multiyear Plan for the Hydrogen R&D Program, Office of Power Delivery, Office of Power Technologies, Energy Efficiency and Renewable Energy, USA, 1999.

References

1 Seayad, A.M.; Antonelli, D.M. Recent Advances in Hydrogen Storage in Metal-Containing Inorganic Nanostructures and Related Materials. Adv. Mater, 2004, 16(9), 765-777.

2 Frost, H.; Snurr, R.Q. Design Requirements for Metal-Organic Frameworks as Hydrogen Storage Materials. J. Phys. Chem. C 2007, 111(50), 18794-18803.

3 Roswell, J.; Yaghi, O.M. Strategies for Hydrogen Storage in Metal-Organic Frameworks. Angew. Chem., Int. Ed. 2005, 44(30), 4670-4679.

4 Murray, L.J.; Dinca, M.; Long, J.R. Hydrogen storage in metal–organic frameworks. Chem. Soc. Rev. 2009, 38, 1294-1314.

5 Collins, D.J.; Zhou, H.-C. Hydrogen storage in metal–organic frameworks. J. Mater. Chem. 2007, 30, 3154-3160.

6 Zhao, D.; Yuan, D.; Zhou, H.-C. The current status of hydrogen storage in metal–organic frameworks. Energy Environ. Sci. 2008, 1, 222-235.

7 Chae, H.; Siberio-Perez, D.Y.; Kim, J.; Go, Y.; Eddaoudi, M.; Matzger, A.; O'Keeffe, M.; Yaghi, O.M. A route to high surface area, porosity and inclusion of large molecules in crystals. Nature, 2004, 427, 523-527.

8 Furukawa, H.; Miller, M.; Yaghi, O.M. Independent verification of the saturation hydrogen uptake in MOF-177 and establishment of a benchmark for hydrogen adsorption in metal–organic frameworks. J. Mater. Chem., 2007, 17, 3197-3204.

9 Ferey, G.; Mellot-Draznieks, C.; Serre, C.; Millange, F.; Dutour, J.; Surble, S.; Margiolaki, I. A Chromium Terephthalate-Based Solid with Unusually Large Pore Volumes and Surface Area. Science, 2005, 309(5743), 2040-2042.

10 Latroche, M.; Surblé, S.; Serre, C.; Mellot-Draznieks, C.; Llewellyn, P.L.; Lee, J.-H.; Chang, J.-S.; Jhung, S. H.; Férey, G. Hydrogen Storage in the Giant-Pore Metal-Organic Frameworks MIL-100 and MIL-101 Angew. Chem., Int. Ed., 2006, 45(48), 8227-8231.

11 L. Wang, R. T. Yang. Catal. Rev. – Sci. Eng. (2010), CR/2010/00152.

12 Robell, A. J., Ballou, E. V., and Boudart, M. J. Phys. Chem. 1964, 68, 2748

13 Srinivas, S. T. and Rao, P. K. J. Catal. 1994, 148, 470

14 Conner, W. C., Jr. and Falconer, J. L. Chem. Rev. 1995, 95, 759

15 Pajonk, G.M. Contribution of spillover effects to heterogeneous catalysis. Appl. Catal. A, 2000, 202(2), 157-169.

16 Bond, G.C. in: Twigg M.V.; Spencer M. S. (Eds.), Metal-Catalyzed Reactions of Hydrocarbons, Springer. New York, 2005, p. 118.

17 Wang, L. and Yang, R. T. Energy Environ. Sci. 2008, 1, 268.

18 Sinfelt, J.H.; Lucchesi, P.J. Kinetic Evidence for the Migration of Reactive Intermediates in Surface Catalysis. J. Am. Chem. Soc., 1963, 85(21), 3365-3367.

19 Khoobiar, S. Particle to Particle Migration of Hydrogen Atoms on Platinum—Alumina Catalysts from Particle to Neighboring Particles. J. Phys. Chem. 1964, 68(2), 411-412.

20 Boudart, M.; Aldag, A.W.; Vannice, M.A. On the slow uptake of hydrogen by platinized carbon. J. Catal. 1970, 18(1), 46-51.

21 Mitchell, P.C.H.; Ramirez-Cuesta, A.J.; Parker, S.F.; Tomkinson, J.; Thompsett, D. Hydrogen Spillover on Carbon-Supported Metal Catalysts Studied by Inelastic Neutron Scattering. Surface Vibrational States and Hydrogen Riding Modes. J. Phys. Chem. B, 2003, 107(28), 6838-6845.

22 Mitchell, P.C.H.; Ramirez-Cuesta, A.J.; Parker, S.F.; Tomkinson, J. Inelastic neutron scattering in spectroscopic studies of hydrogen on carbon-supported catalytsts-experimental spectra and computed spectra of model systems. J. Mol. Struct., 2003, 651-653, 781-785.
23 Zhan, D.; Velmurugan, J.; Mirkin, M.V. Adsorption/Desorption of Hydrogen on Pt Nanoelectrodes: Evidence of Surface Diffusion and Spillover. J. Am. Chem. Soc. 2009, 131(41), 14756-14760.
24 Panayotov D.A.; Yates Jr., J.T. Spectroscopic Detection of Hydrogen Atom Spillover from Au Nanoparticles Supported on TiO_2: Use of Conduction Band Electrons. J. Phys. Chem. C, 2007, 111(7), 2959-2964.
25 Chen, L.; Cooper, A.C.; Pez, G.P.; Cheng, H.S. Mechanistic Study on Hydrogen Spillover onto Graphitic Carbon Materials. J. Phys. Chem. C, 2007, 111(51), 18995-19000.
26 Sha, X.; Knippenberg, M.T.; Cooper, A.C.; Pez, G.P.; Cheng, H.S. Dynamics of hydrogen spillover on carbon-based materials. J. Phys. Chem. C, 2008, 112(44), 17465-17470.
27 Singh, A.K.; Ribas, M.A.; Yakobson, B.I. H-Spillover through the Catalyst Saturation: An Ab Initio Thermodynamics Study. ACS Nano 2009, 3, 1657-1662.
28 Y. Lin, F. Ding, B.I. Yakobson, Phys. Rev. B: Condens Matter 78 (2008), pp. 041402-1–04102-4
29 Suri, M.; Dornfeld, M.; Ganz, E. Calculation of hydrogen storage capacity of metal-organic and covalent-organic frameworks by spillover. J. Chem. Phys. 2009, 131, 174703-174706.
30 Li, Y.; Yang, R.T. Hydrogen storage in metal-organic frameworks by bridged hydrogen spillover. J. Am. Chem. Soc., 2006, 128(25), 8136–8137.
31 Yang, R. T.; Li, Y. W.; Lachawiec. A. J. 2007 Annual Progress Report, DOE Hydrogen Program; U. S. Department of Energy: Washington, DC, 2007; IV. C.1b, 539-541.
32 Wang, C.-Y.; Tsao, C.-S.; Yu, M.-S.; Liao, P.-Y.; Chung, T.-Y.; Wu, H.-C.; Miller, M.A.; Tzeng, Y.-R. Hydrogen storage measurement, synthesis and characterization of metal-organic frameworks via bridged spillover. J. Alloys Comp. 2010, 492(1-2), 88–94.
33 Miller, M.A.; Wang, C.-Y.; Merrill, G.N. Experimental and theoretical investigation into hydrogen storage via spillover in IRMOF-8. J. Phys. Chem. C, 2009, 113(8), 3222–3231.
34 Tsao, C.-S.; Yu, M.-S.; Wang, C.-Y.; Liao, P.-Y.; Chen, H.-L.; Jeng, U-S.; Tzeng, Y.-R.; Chung, T.-Y.; Wu, H.-C. Nanostructure and hydrogen spillover of bridged metal-organic frameworks. J. Am. Chem. Soc., 2009, 131(4), 1404–1406.
35 Liu, Y.-Y.; Zeng, J.-L.; Zhang, J.; Xu, F.; Sun, L.-X. Improved hydrogen storage in the modified metal-organic frameworks by hydrogen spillover effect. Inter. J. Hydrogen Energy, 2007, 32(16), 4005–4010.
36 S. J. Yang, J. H. Cho, K. S. Nahm, C. R. Park, Int. J. Hydrogen Energy, doi:10.1016/j.ijhydene.2010.04.066.
37 Zlotea, C.; Campesi, R.; Cuevas, F.; Leroy, E.; Dibandjo, P.; Volkringer, C.; Loiseau, T.; Ferey, G.; Latroche, M. Pd nanoparticles embedded into a metal-organic framework: synthesis, structural characteristics, and hydrogen sorption properties. J. Am. Chem. Soc., 2010, 132(9), 2991–2997.
38 Cheon, Y.E.; Suh, M.P. Enhanced hydrogen storage by palladium nanoparticles fabricated in a redox-active metal–organic framework. Angew. Chem. Int. Ed., 2009, 48(16), 2899–2903.

39 Proch, S.; Herrmannsdofer, J.; Kempe, R.; Kern, C.; Jess, A.; Seyfarth, L.; Senker, J. Pt@MOF-177: synthesis, room-temperature hydrogen storage and oxidation catalysis. Chem. Eur. J., 2008, 14, 8204–8212.
40 Liu, Y.Y.; Zhang, J.; Zeng, J.L.; Chu, H.L.; Xu, F.; Sun, L.X. Hydrogen storage capacity of nickel supported on a metal-organic framework compound under mild conditions Chin. J. Catal., 2008, 29(7), 655-659.
41 Stuckert, NR; Wang, LF; Yang, RT. Langmuir, 2010, 26, 11963.
42 Yaghi, O. M., Eddaoudi, M., Li, H., Kim, J., and Rosi, N. U.S. Patent No. 6,930,193 B2, 2005.
43 Tsao, C. S., Yu, M. S., Chung, T. Y., Wu, H. C., Wang, C. Y., Chang, K. S., and Chen, H. L. J. Am. Chem. Soc. 2007 129 15997 16004
44 A.J. Lachawiec Jr., T.R. DiRaimondo and R.T. Yang, Rev. Sci. Instrum. 79 (2008), pp. 063906–063917.
45 Tsao, C.S.; Tzeng, Y.R.; Yu, M.S.; Wang, C.Y.; Tseng, H.H.; Chung, T.Y.; Wu, H.C.; Yamamoto, T.; Kaneko, K.; Chen, S.H. J. Phys. Chem. Lett., 2010, 1(7), 1060–1063.
46 Zubizarreta, L.; Menndez, J.A.; Pis, J.J.; Arenillas, A. Improving hydrogen storage in Ni-doped carbon nanospheres. Int. J. Hydrogen Energy, 2009, 34(7), 3070-3076.
47 Lin, K.-Y.; Tsai, W.-T.; Yang, T.-J. Effect of Ni nanoparticle distribution on hydrogen uptake in carbon nanotubes. J. Power Sources, doi:10.1016/j.jpowsour.2010.04.026.
48 Back, C.-K.; Sandi, G.; Prakash, J.; Hranisavljevic, J. Hydrogen sorption on palladium-doped sepiolite-derived carbon nanofibers. J. Phys. Chem. B, 2009, 110(33), 16225–16231.
49 Lachawiec, A. J., Jr. and Yang, R. T. Langmuir 2008, 24, 6159.
50 Benson, J. E.; Kohn, H. W.; Boudart, M. *Journal of Catalysis*, 1966, 5, 307.
51 Konvalinka, J. A.; Scholten, J. J. F. *Journal of Catalysis*, 1977, 48, 374-385.
52 Lei, Y.; Shevlin, S. A.; Zhu, W.; Guo, Z. X. *Phys. Rev. B* 2008, 77, 134114.
53 McCabe, R. W. ; Schmidt, L. D. *Surface Science*, 1976, 60, 85-98.
54 McCabe, R. W. ; Schmidt, L. D. *Surface Science*, 1977, 65, 189-209.
55 Shern, C.S. *Surface Science* 1992, 264, 171-176
56 McCabe, R. W. ; Schmidt, L. D. *Surface Science*, 1977, 66, 101-124.
57 Stadie, N. P.; Purewal, J. J.; Ahn, C. C.; Fultz, B. *Langmuir* 2010, Article ASAP
58 McKay, H.; Wales, D. J.; Jenkins, S. J.; Verges, J. A.; de Andres P. L. *Physical Review B* 2010, 81, 075425.

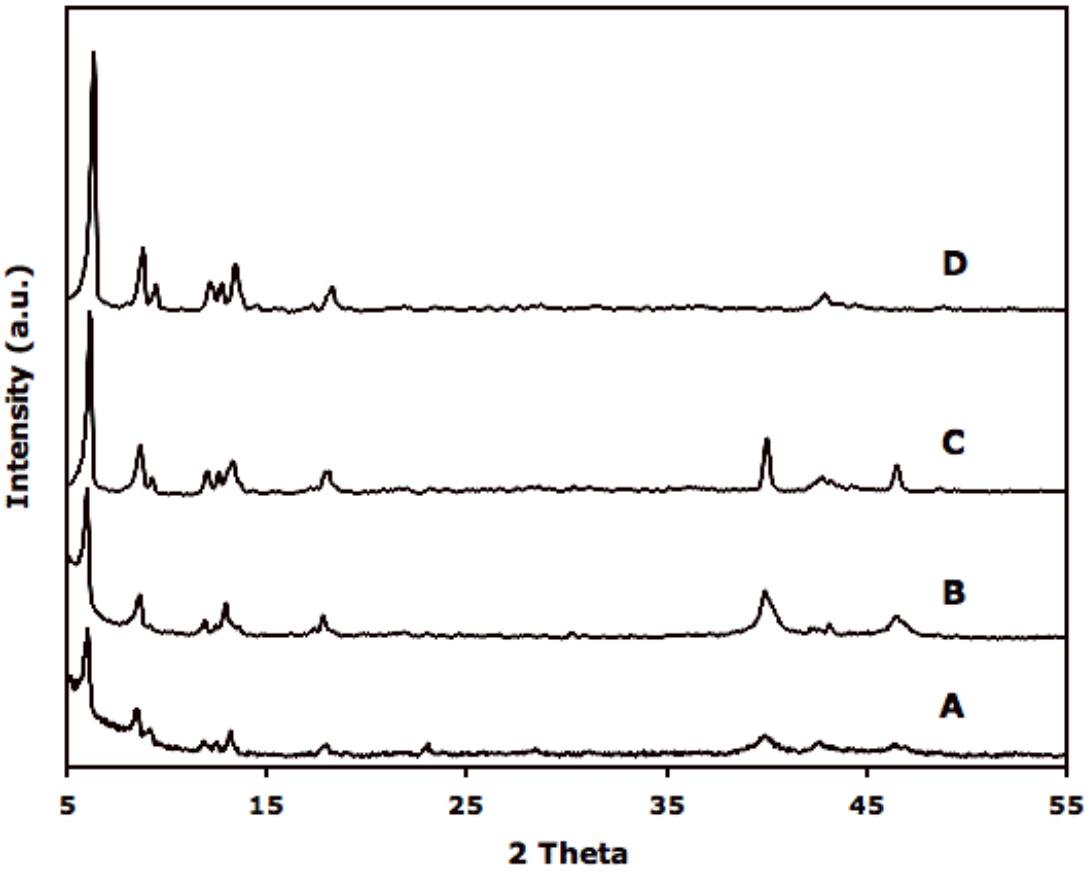

Figure 24. XRD patterns of Pt/IRMOF-8-1 (A), Pt/IRMOF-8-2 (B), Pt/IRMOF-8-3 (C) and pure IRMOF-8 (D). Obtained by Lifeng Wang.

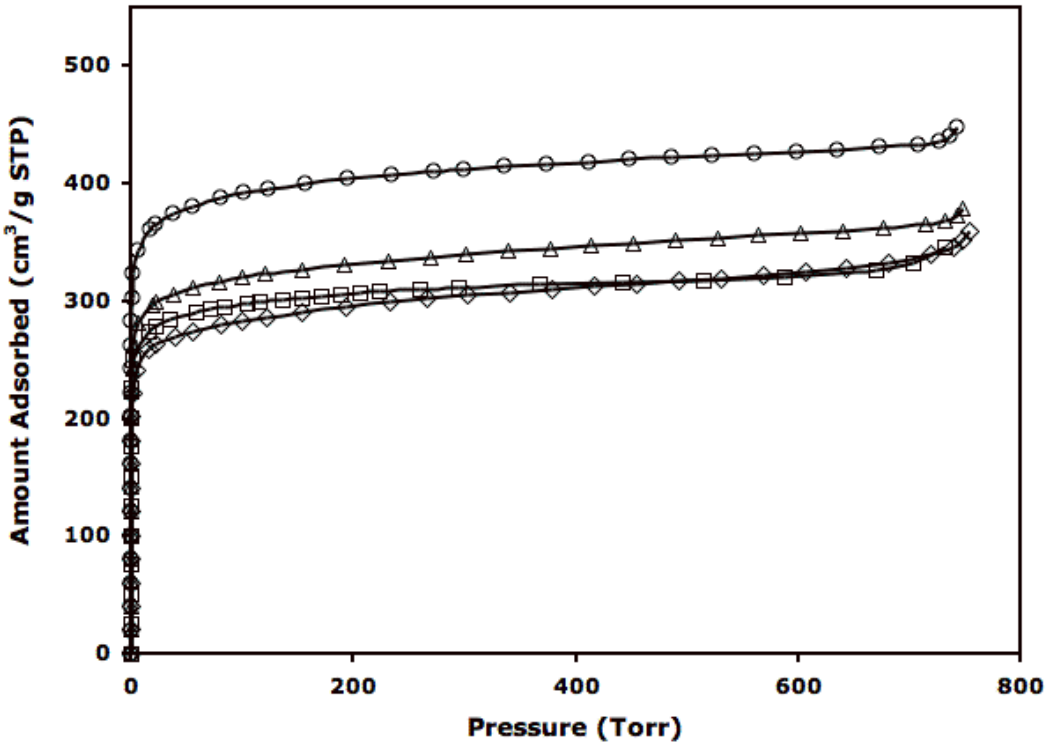

Figure 25. Nitrogen isotherms of Pt/IRMOF-8-1 (△), Pt/IRMOF-8-2 (□), Pt/IRMOF-8-3 (◇) and pure IRMOF-8 (○).Obtained by Lifeng Wang.

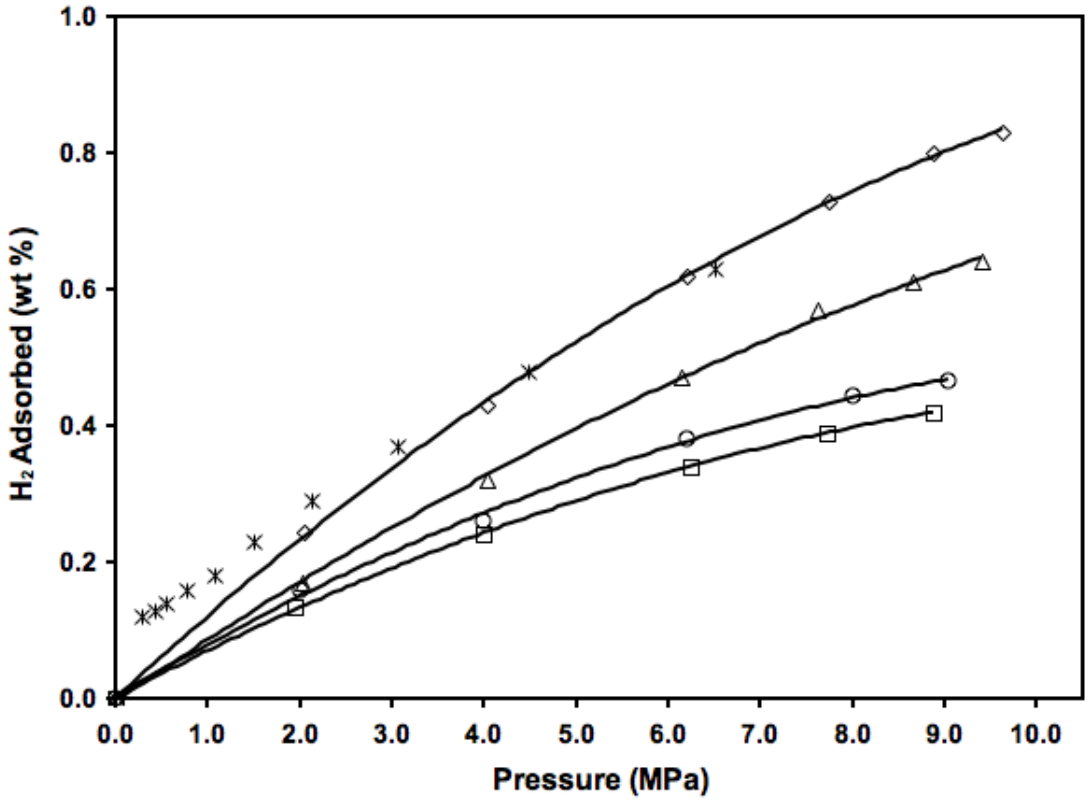

Figure 26. High-pressure hydrogen isotherms at 298 K for plain IRMOF-8 (□), Pt/IRMOF-8-1 (◇), Pt/IRMOF-8-2 (△) and Pt/IRMOF-8-3 (○) samples. Stars * mean desorption. Obtained by Lifeng Wang.

A)

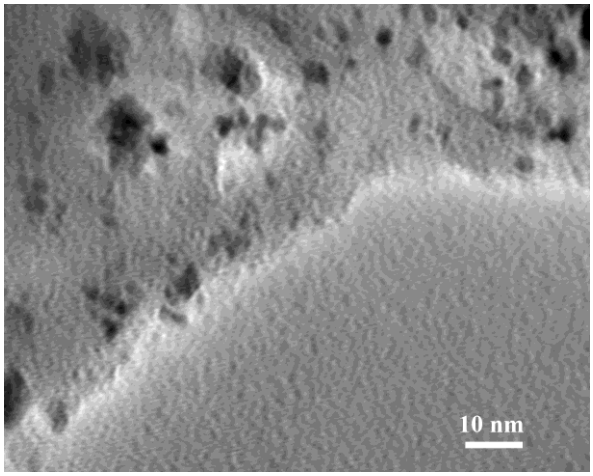

B)

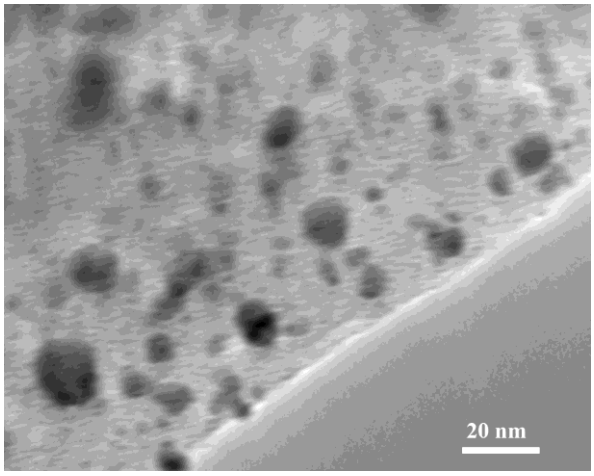

C)

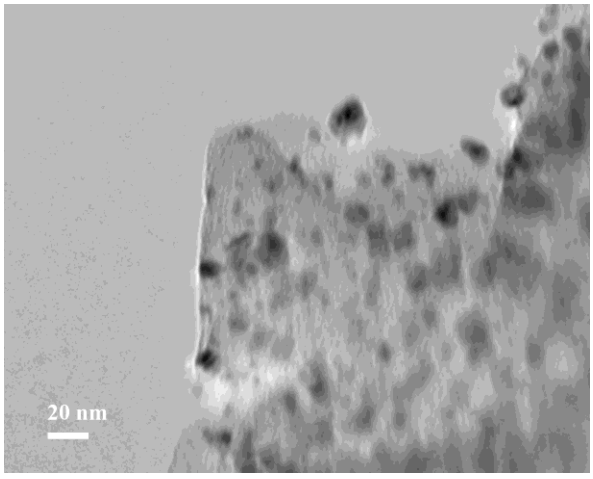

Figure 27. TEM images of Pt/IRMOF-8-1 (A), Pt/IRMOF-8-2 (B) and Pt/IRMOF-8-3 (C). Obtained by Lifeng Wang.

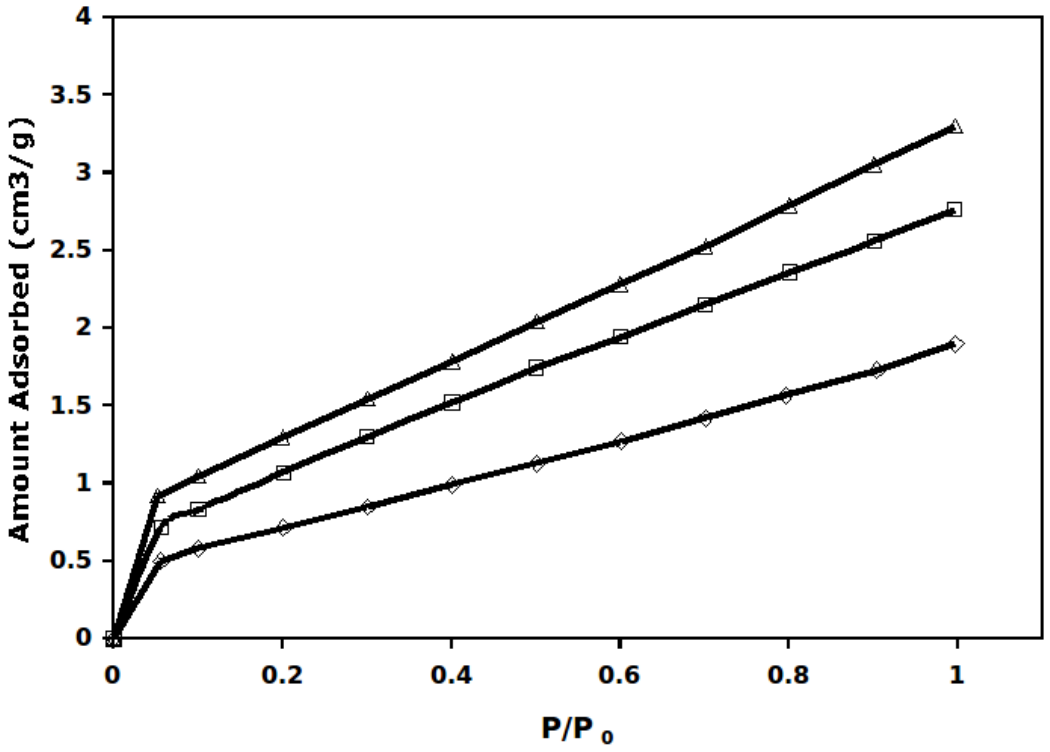

Figure 28. Hydrogen isotherms of Pt/IRMOF-8-1 (△), Pt/IRMOF-8-2 (□) and Pt/IRMOF-8-3 (◇).Obtained by Lifeng Wang.

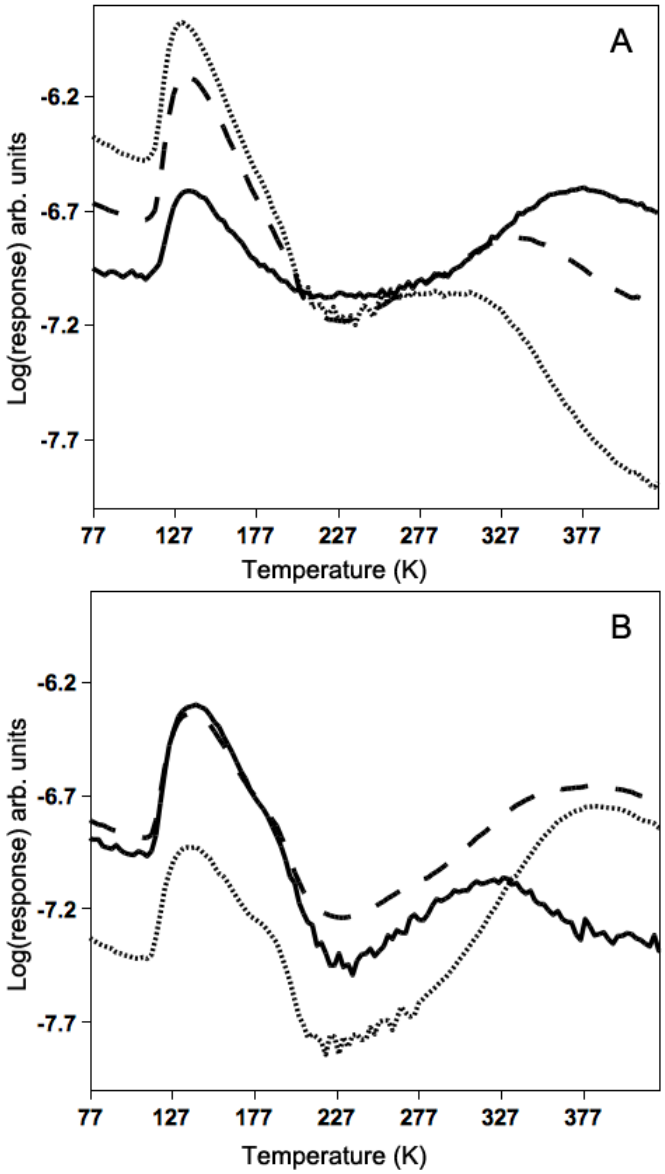

Figure 29. The TPD spectra for Pt/IRMOF-8. (A) H_2 was dosed for 1 hr at 298 K and 300 torr. D_2 was subsequently dosed without evacuation but left ~22 torr of H_2 and 300 torr D_2 for 30 min at 298 K. (B) D_2 was dosed for 24 hr at 298 K and 300 torr. H_2 was subsequently dosed without evacuation but left ~22 torr of D_2 and 400 torr H_2 for 15 min at 298 K. H_2 (—), D_2 (…) and HD (–––) are shown for all spectra.

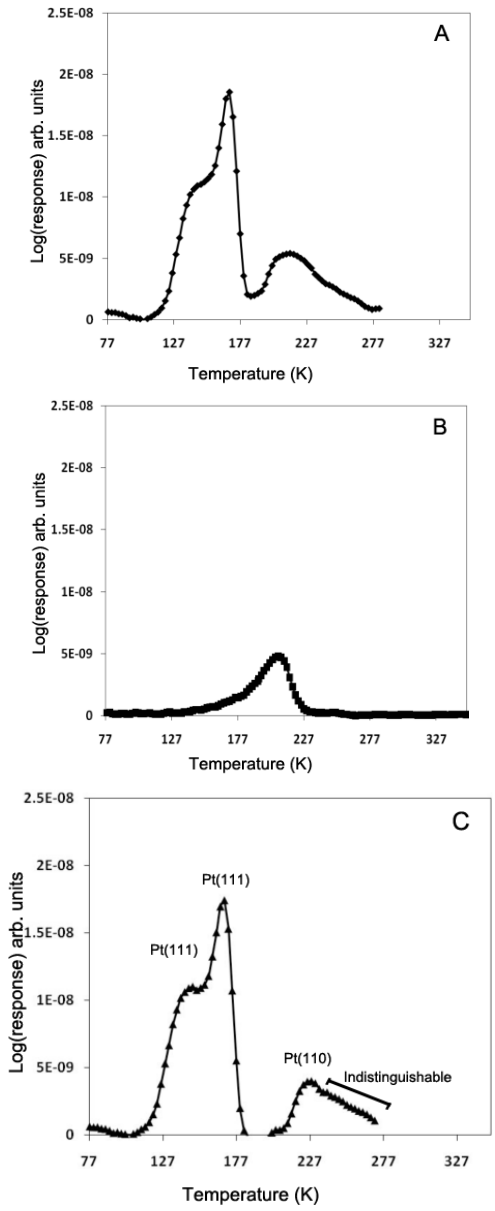

Figure 30. The TPD spectra for Pt/IRMOF-8 and IRMOF-8 at low pressure. D_2 was dosed for 5 min at 298 K and 25 torr, then quenched, evacuated and heated at a rate of 10K/min (A) Pt/IRMOF-8, (B) IRMOF-8, (C) Difference between A and B (showing only Pt contributions). The peaks are labeled corresponding to Pt binding sites derived from reference sources[53-56].

Chapter 4: Atmospheric CO2 Capture and Simultaneous Concentration using Zeolites and Amine Grafted SBA-15

Introduction

CO_2 capture from the atmosphere ("air capture") and sequestration has recently gained interest as a true carbon negative alternative.[1] To this end, it is important to be able to concentrate the captured CO_2 into >90% concentration that is suitable for underground storage. While carbon capture at concentrated streams (e.g., from power plants) is desirable, in the case of emission from the transportation sector (which accounts for 23% of total CO_2 emission), this is infeasible.[2] Additionally, proposals have been presented where atmospheric CO_2 could be used to generate hydrocarbon fuels that would allow continuing use of the transportation infrastructure.[3]

Atmospheric CO_2 capture for air purification has been reported by numerous other groups. The methods fall into three categories. The first are amine based adsorbents.[4-6] These come from an extension of flue gas capture,[7-14] where the amine adsorption rates are relatively fast.[10] These same adsorbents demonstrate adsorption half times that are almost two orders of magnitude slower under atmospheric conditions.[4] The pseudo-diffusion time constants (D/R^2) necessary for adsorber design have not been reported. Here I address this issue and give both the heat of adsorption and pseudo-diffusion time constants. I take into account pore blocking effects[10] from amine grafted groups by grafting only the smallest amount of amine necessary for accurate measurements.

The second category of adsorbents are zeolites, which have long been considered for atmospheric CO_2 removal[15] as well as flue gas conditions.[16-28] Initially the view of CO_2 was as a contaminant in pressure swing adsorption processes (PSA) and pre-purification has been studied for almost all common zeolites.[15] Based on Nitrogen adsorption trends, high cation content zeolites hold the most promise.[14] These would be low silica types of zeolite X. Previous information on low-silica type X zeolite is not available for CO_2 contaminant removal. The

previously most studied zeolite has been NaX. Thus, I will use the benchmarks from NaX as a comparison.

The third group would be capture by caustic solution spraying.[23-28] This method has been particularly well developed recently, with an emphasis on industrialization. Drawbacks of applying this solution are the need for both water and sodium hydroxide. The largest benefit is the cost which at \$53/ton CO_2 captured is a good price target.[29] However, the authors did not include the air compression cost, which is \$150 per psi increase for a ton of CO_2 passed (assuimg an energy cost of \$0.06/(kW h)).[30] For adsorbents this cost will be the most critical, as it eliminates pressure swing adsorption (PSA)[31] for atmospheric CO_2 capture.

Zeolites have been known to have reduced capacity under moist conditions.[14] Here I will employ the use of a guard bed,[32] using a desiccant or potassium substituted zeolite type A (3A). This would be feasible in relatively dry environments which would enable the use of a small fraction of the total bed for water removal.

One prominent set of adsorbents not tested are metal organic frameworks (MOFs)[33-36]. These along with other zeolites[37,38], may be able to retain fast rates while reducing water sensitivity (shown as a major issue later) and are good candidates for future study.

Additionally, in an ideal case, temperature swing adsorption (TSA) would be sufficient for CO_2 purification.[39] I will show that due to co-adsorption of N_2 and CO_2, single cycle-TSA, without a purge, is not sufficient to meet the carbon capture and storage (CCS) target for zeolites where a CO_2 desorption product of >90% is desired for underground storage. I will show a vacuum degas of the pores is ideal.[40] This is due to the low partial pressure of the adsorbate of interest (CO_2), which ensures minimal loss. This is also helped by the higher partial pressures of competing adsobates (N_2 and O_2) and nearly linear isotherms, which allows their quick, almost complete removal. Previously, a combined temperature vacuum swing adsorption (TVSA) has been proposed and optimized previously for flue gas concentration[41]. To our knowledge this is the first time TVSA has been proposed for atmospheric capture.

Materials and Methods

Ion exchanged zeolites. Ion exchange was performed according to Hutson et al.[14] 250 mg of Na-LSX or NaX or NaY zeolite was added to 50 mL water and heated with stirring. 2 mmol of

Na/K/Li/Ca hydroxide was added, followed by 5 mol of Na/K/Li chloride or calcium nitrate. The solution was heated to 90 °C and stirred for 2 hours, then decanted. This was repeated 8 times. The solution was rinsed with DI water and decanted 5 times to ensure removal of the chloride solution. Surface area was compared to the starting material to test for retained crystalline structure. XRD patterns of LSX prepared zeolites are presented in the supporting information, also showing retained crystallinity.

SBA-15. Meoporous silica SBA-15 was prepared using the procedure reported by Zhao et al.[42] Four grams of Pluronic 123 was added to 144 mL of 1.7 M HCl at 40 °C and stirred until dissolved. 8 g of TEOS was then added and stirred for 2h. The sample was filtered then calcined at 385 °C for 4h.

SBA-15 grafted with amine. SBA-15 was grafted with low amounts of 3-aminopropyltrimethoxysilane to ensure no pore blocking and accurate maximum rate determination.[4] A procedure similar to Hicks et al.[43] was followed. 400 mg of SBA-15 was dissolved in 20 mL of anhydrous toluene while stirring and placed under nitrogen protection. 200 mg of 3-aminopropyltrimethoxysilane was then added to the solution. The solution was stirred for 12 hours, then filtered and washed with toluene. The sample was then dried under vacuum at 100°C. A yield of 1 mmol/g amine loading was achieved, determined through weight loss analysis during decomposition on a thermogravimetric analyzer (TGA).

Pellets. Commercial grade pellets were obtained for Li-LSX and NaX. Ion exchange was performed for K-LSX as described above, except stirring was replaced with vigorous swirling. Information for this procedure is discussed more thoroughly in the supporting information. Pellets for SBA-15 were made using a compression pressure of 200 atm (20 MPa) which provided a low loss in capacity.[44]

Sample Preparation. Degas conditions were 400 °C for LiLSX, 385 °C for NaLSX, 350 °C for KLSX[14] and 120 °C for amine-grafted SBA-15, and were evacuated until a final pressure of 1.3×10^{-8} atm was achieved. All thermal conditions are of both the wall and the bed. Heating was carefully performed from the interior wall. The extreme importance of heating throughout these experiments is discussed more thoroughly in the supporting information.

Equilibrium Isotherms. Pure component isotherms and the BET surface areas were obtained using a Micromeritics ASAP 2020 sorptometer (which is a Sievert's volumetric technique). For the CO_2 isotherms, pressure ranged from 3×10^{-6} atm to 1 atm.

The isosteric heats of adsorption were calculated from the temperature dependence of the isotherms by using the Clausius-Clapeyron equation. Specifically by using multiple isotherms at different temperatures and evaluating the slope of ln(P) versus (1/T) for the same adsorption amount for the different isotherms. Zero loading heats of adsorption were obtained by fitting Langmuir, Fruendlich and Toth isotherms and are discussed later.

Rates of adsorption were calculated using the same instrument. A pressure step from 6.5×10^{-6} atm to 4.6×10^{-5} atm (or, 0.005 Torr to 0.035 Torr) was selected. This corresponds to the rate of uptake for only the amine adsorption of CO_2 in the amine grafted SBA-15 (which was determined by background subtraction with pure SBA-15 and is shown in the supporting information). This was done such that the rates could be compared for the same pressure increase step for all sorbents. Additionally this pressure step was shown to have good agreement with the TGA analysis described below. It was noted that as loading increased, the rate of adsorption for amines slowed slightly (~10%). Further discussion of the rate measurement procedure is available in the supporting information.

Thermogravimetric Analysis (TGA). Total equilibrium adsorption amounts as well as adsorption rates were measured using a Shimadzu TGA-50 analyzer, under dry and wet conditions, for both atmospheric air and pure CO_2. The rate of adsorption was taken as a pressure step from 0 to 4×10^{-4} atm CO_2 for both wet (R.H. 80%) and dry conditions, using a balance of N_2. The rate obtained for dry CO_2 for amine grafted SBA-15 was identical to that obtained using the sorptometer. I assume that this indicates that this method provides accurate rate information under these conditions, as well as wet conditions. This point is further discussed in the supporting information.

Fixed-Bed Adsorber Breakthrough Curves. Breakthrough curves were measured using a vertical, fixed bed with ambient air feed in a down-flow manner. The outlet CO_2 concentration was continually monitored with a Vaisala GMP220 probe. Additionally there was a pressure gauge located at the bed feed and a flow meter controlling the bed feed. Beds were set at 3

inches (7.62 cm) in height, and ¼" (0.64 cm) diameter. Void factions were measured via helium displacement (assisted by the Micromeritics 2020) and had total void fractions of 85±3% for amine-grafted SBA-15 and 70±3% for zeolites. Beds were contained by using a small piece of quartz wool and a pinch in the glass neck, instead of a frit.

For measuring the breakthrough curves, fixed beds were prepared for all sorbents. Preparation of a fixed bed of amine-grafted SBA-15 presented a problem because it was in the form of fine powder. Compaction into pellets reduces adsorption and capacity significantly in order to form stable pellets.[40] Additionally, pellets are not ideal, adding another 35% fraction to void spaces. Thus, a new technique for forming an amine-grafted SBA-15 bed was employed. This consisted of dispersing the synthesized powder in toluene and then drying (by heating to 40 °C) until a slurry 20% larger in volume than the packed powder was obtained. The slurry was then injected into the bed column and allowed to dry (by heating to 60 °C) with a constant 1.14 atm (13.8 kPa) pressure applied to the bed by flowing air. This allowed the formation of a meso-crystalline structure able to withstand a 1.7 atm (25 psi) pressure drop per inch, but with a lower flow resistance (0.013 atm / 0.2 psi drop vs. 0.09 atm / 1.3 psi drop for pellets), lower total void fraction (75±3% vs. 85±3%) and marginally better breakthrough performance (possibly due to lower void fraction, and better macro-pore diffusion). Further comparison and analysis is available in the supporting information. This new bed design for silicas was used for all subsequent tests.

Desorption from TSA and Combined VSA/TSA. Commercial adsorption processes are operated via TSA or PSA/VSA.[32] Combined TSA and VSA/PSA are also used in industry. These processes are tested in this work to study the feasibility of producing desorption products with over 90% CO_2 concentration that is suitable for permanent storage.

Desorption gas concentrations were measured using a mass spectrometer (Vacuum Technology, Inc. Magnetic Sector MS50) and compared to standards of known CO_2/air concentrations. All measurements were taken on a dry basis. Temperature swing desorption was done by heating a saturated bed (dry conditions for zeolites and RH of 80% for amine) with

one end closed and sampling the evolved gas while the temperature was rapidly increased (~500 °C/min) from room temperature.

For combined vacuum and temperature swing adsorption, the saturated breakthrough bed was used. Connection to a pressure gauge and valves caused an additional 25% increase in void space, which decreased the CO_2 concentration of the desorption products. Thus, the results reported here represent lower limits. Vacuum swing or a quick vacuum degas was done first. In the first step, each bed was evacuated to 0.01 atm absolute pressure (while sampling) in order to clear voids and remove adsorbed nitrogen. Vacuum was then stopped and the previous TSA process was performed, except the gas was not sampled until the pressure was over 1 atm and the temperature needed varied from 80-260 °C for tested adsorbents. In both steps, the feed end of the bed was closed during degassing and TSA heating desorption. An optional third degas step was added, where the vacuum was resumed until 0.01 atm and the temperature was held constant. The vacuumed gas at this step could be used as well. I want to emphasize that it is impossible to tell which parameters will be ideal. Adjustments to temperature and vacuum rates, as well as the times which step two and/or step three are operated are dependent on the specific economics of the implementation. Additionally, heating done with a hot purge gas will be highly dependent on having a vacuum recovery.

Results and Discussion

Pure-Component Isotherms. Pure component equilibrium capacities of sorbents of interest are shown in Table 1, Figure 31 and Figure 32. All others are available in the supporting information. A comparison with previously published data for NaX[15], shows that capacities are similar to previously published data. The data for Li-LSX also shows that I are reporting the highest capacity for a zeolite at atmospheric conditions published thus far. The previously observed trend for zeolite X holds for low silica type X as well.[45] That is, zero loading heat of adsorption for cations follows Li&Ca>Na>K. This is further examined in the supporting information.

The isosteric heats of adsorption of CO_2 and N_2 for sorbents of interest are also shown in Table 1. The other sorbents are presented in the supporting information. The heats of adsorption for CO_2 are much higher than that of N_2, mainly due to the larger quadrupole

moment of CO_2, as discussed in the supporting information. The effect of the cation size, and the effect of cation charge, are both manifested in the differences in the heats of adsorption. The isosteric heats of adsorption of CO_2 at zero loading were predicted using Langmuir (fitted from 0 - 1.4×10^{-3} atm), Freundlich and Toth[46] isotherms. They were not predicted using extrapolated data since it is clear that the isotherms are non-linear at the lowest adsorption pressure recorded. This means saturation effects are present and must be accounted for (this eliminates Henry's constant fitting as well). The isosteric heats of adsorption were also predicted purely theoretically as described in the supporting information. Langmuir fitting gave the values closest to what would be expected theoretically and are reported in Table 1. The Toth and Freundlich isotherms both fit well over the entire pressure range. The Toth isotherm proved a slightly better fit, as found for CO_2 on other zeolites[46]. Fitted parameters are available in the supporting information.

Adsorption Rates. The adsorption uptake rate is an important parameter that determines the fixed-bed adsorption performance.[32] For CO_2 adsorption on zeolites and carbons, pore diffusion is the rate limiting step, and the uptake rate can be conveniently expressed by a diffusion time constant (D/R^2, where D is pore diffusivity and R is the particle radius). For CO_2 adsorption on amine-grafted silicas, the uptake rate is limited by a chemical reaction between CO_2 and the primary amine group(s).[8,33] Under dry conditions, one CO_2 reacts with two amine groups to form a zwitterion carbamate; whereas two CO_2 and two H_2O react with two amine groups to form two bicarbonates under wet conditions. For practical purposes (i.e., for prediction of breakthrough curves and for comparison with other sorbents such as zeolites), I expressed the uptake (reaction) rates of CO_2 on amine-grafted silica by a pseudo diffusion time constant D/R^2. Experimentally, the values of D/R^2 can be determined from the uptake rates (i.e., amount adsorbed vs. time upon a step change in gas-phase concentration). To this end, the following diffusion equation is solved:

$$\frac{\partial u}{\partial t} = D\left(\frac{\partial^2 u}{\partial r^2}\right) \tag{3}$$

$$u = Cr \tag{4}$$

Where r denotes the radial distance from the center of the spherical particle and C is the concentration at radial distance r and time t. The diffusion equation is solved for a step change in the surface concentration (at r = R), and the short time approximation for $M_t/M_¥$ < 0.3 is given by:

$$\frac{M_t}{M_¥} » \frac{4}{\sqrt{p}}(\frac{Dt}{R^2})^{1/2} \quad (5)$$

Where M_t and $M_¥$ represent the total adsorbed amounts of CO_2 at time *t* and at equilibrium, respectively.[51]

The diffusion time constants were determined for CO_2 on all sorbents from uptake rates by using either the Micromeritics sorptometer (for zeolites, carbons and dry amine-grafted SBA-15) or TGA (for amine-grafted silica, both dry and wet conditions). They are shown in Table 1 and in Figure 33. This is the first time the diffusion time constant is published for amine at atmospheric concentrations of CO_2. It is seen that the uptake rates are significantly higher on zeolites than amine-grafted SBA-15, approximately 2 orders of magnitude higher. For amine-grafted SBA-15, the uptake rates are lower under wet conditions than dry conditions. The values of the diffusion time constants for LSX zeolites were typical of diffusion of CO_2 in type X zeolites[15]. Additionally, the results for LSX followed the trend previously observed for zeolite Y[49].

CO_2/N_2 Selectivity. The selectivity ratio for actual performance conditions (the result of CO_2 adsorption divided by N_2 adsorption from Table 2) shows that single step temperature swing adsorption will not produce high purity (>90%) CO_2 for zeolites (since high amounts of N_2 would adsorb, and bed dilution would occur). For amines, single step TSA could be possible, if sufficient CO_2 adsorption occurred (>1 mmol/g). Many variations of these adsorbents are known that could meet this challenge.[9-13] It should be noted that these selectivity ratios were based on pure-component isotherms for N_2. Under mixed gases, both gases will compete and adsorb less, but the component that adsorbs more strongly (i.e., CO_2) will be favored. Additionally, the binder could be modified to adsorb CO_2 and not only N_2 using a novel alkaline treatment.[51]

Fixed-Bed Breakthrough Curves. Based on the information from the isotherms, the zeolite sorbent with the highest CO_2 capacity (Li-LSX), and the highest CO_2/N_2 selectivity (K-LSX) were

selected for breakthrough experiments. Additionally, the widely used commercial zeolite NaX was selected for comparison. Breakthrough performance was also studied for the amine-grafted silica, SBA-15. Feed gas-hourly space velocities (GHSV) at > 1000 hr^{-1} were used for all sorbent beds. The results for dry conditions are summarized in Figure 34. These were compared with previously published results for NaX[15] and found to match closely. No published data for zeolite LSX or dry amine conditions is available at this time for comparison.

The sharpness of the fixed-bed breakthrough curves is determined by the adsorption rates, or, D/R^2; high D/R^2 yields sharp breakthrough while low D/R^2 leads to dispersed breakthrough.[32] This is clearly seen in Figure 34. All three zeolites showed sharp breakthrough curves due to their large D/R^2, while a highly dispersed breakthrough curve for amine-grafted SBA-15 led to premature CO_2 breakthrough. Much lower GHSVs are needed for the amine-grafted SBA-15 bed to yield clean breakthrough curves (1500 hr^{-1} for amine grafted SBA-15 vs. 63000 hr^{-1} for LiLSX).

The dependence of the breakthrough capacity on the feed space velocity is demonstrated in Figure 34, for dry air on Li-LSX. As the feed space velocity was increased to very high values, the CO_2 capacity remained and sharp breakthrough curves were preserved. At all GHSV tested, the bed capacity at the breakthrough point was approximately 0.82 mmol/g (Figure 34), compared to the pure-component capacity of 1.34 mmol/g (Table 1). The pure-component capacity was measured on a powder while the bed breakthrough capacity was measured on pellets that contained approximately 15% binder with no CO_2 capacity. This comparison shows rather effective use of the Li-LSX in a fixed bed adsorber. The drop in the capacity for CO_2 compared with the pure component isotherm capacity was also due to competing adsorption with nitrogen. Table 2 shows the adsorption capacity for the breakthrough experiment with ambient air feed, for both wet and dry conditions.

For amine-grafted silica, the performance during breakthrough tests was poor, taking significantly longer to saturate than zeolites under dry conditions, and also being significantly slower still under wet conditions (shown in (dry conditions) Figure 34 and Figure 35 (wet conditions)). As shown below, the desorption half-cycle requires only minutes to complete. Thus, for a commercial duel-bed, tandem-operation for cyclic processes, the cycle time is

determined by the (longer) adsorption breakthrough time. The size of the bed depends directly on the sorbent productivity (i.e., kg CO_2 produced per kg sorbent per hour) which depends on both the equilibrium adsorbed amount and the uptake rate.[32] The results above illustrate that the uptake rate (e.g., as expressed by D/R^2) is as important as the equilibrium adsorbed amount in determining the cyclic process performance.

Moisture Effect. In dry conditions the zeolites performed exceptionally well, but with water almost all adsorption capacity was lost (96%) at a relative humidity (RH) of 80%. This has been observed previously on other zeolites[21] and also for N_2 uptake on LSX.[14] Total CO_2 adsorption was negligible when measured by breakthrough and gravimetric methods (shown in Table 2 and Figure 35). Regeneration of the beds after complete water saturation was studied for Li-LSX and K-LSX. I found that dry air (dried using a potassium substituted zeolite type A adsorbent (3A)) operating capacity could be reached with a regeneration temperature of 400 °C for Li-LSX and 320 °C for K-LSX while using a dry air purge.

Desorption CO_2 Product Purity. As mentioned, temperature-swing and pressure/vacuum-swing adsorption processes are used commercially in large scales. For TSA, many modes of operations are being used, usually involving the use of a purge gas.[32] Most recently, it was proposed to use steam purge for desorption for power plant CCS.[52] In this work, it is intended to demonstrate the feasibility of concentrating CO_2 in the desorption product to over 90% purity. Thus, a simple TSA and a simple combined TSA/VSA cycle was adopted while no purge was used, previously considered for flue gas applications.[41] In TSA, the bed temperature was quickly raised (within two minutes) to various values (as high as 280^{o}C). In TSA/VSA, the feed end of the bed was closed. Then the pressure was decreased until 0.01atm (to degas the voids) and the TSA process was done at 240 °C for LiLSX, 180 °C for KLSX and 80 °C for amine grafted SBA-15. An optional vacuum step while the bed was still heated was tested as well. These temperatures were chosen in order to release 50% of the adsorbed CO_2 at 1 atm. Optimization would be an economic consideration, especially since it was found that the high purity concentration remained under lower temperatures, but the pressure did not exceed 1 atm. The concentration of CO_2 in the effluent gas was monitored by a mass spectrometer.

Three sorbents were used in the desorption study: Li-LSX, K-LSX and amine-grafted SBA-15. By simple TSA, none of these sorbents could produce a desorption product that could reach 90% CO_2 concentration (as discussed earlier, amines have the potential to do this with higher amine loadings). Li-LSX, as expected, showed the best result for TSA. The highest purity was obtained for Li-LSX - 63% at 280 °C, for K-LSX - 56% at 220 °C and for Amine-grafted SBA-15 - 18% at 120 °C for RH 80% and 9% at 120 °C for dry conditions. Measurements were done with and without a purge gas (dry air) where the purge flow was 10 mL/min, however maximum concentration did not decrease and the effect of the purge on the desorption concentration can be seen in the supporting information (SI)Figure 314, which also shows the entire desorption temperature and concentration profile. Process diagrams and steps are also shown in the supporting information.

For the combined TVSA cycle, concentration of the captured gas started at the minimum (93% for Li-LSX, 94% for K-LSX and 98% for Amine-grafted SBA-15) and gradually rose to 99% purity. This process is shown in Figure 36 for the desorption half-cycle in the TVSA process for Li-LSX (using optional desorption step 3). Final purities for these cycles are shown in Figure 37. Fractional removal of CO_2 (i.e. not using a final evacuation step) will cause an increase in exit concentration of CO_2 during the adsorption process. This can be approximated by the observation that time required to saturate the bed remained nearly constant, no matter the amount of CO_2 removed. This is shown more clearly in the supporting information. Process diagrams are also shown in the supporting information for clarity.

It is interesting to note that during TSA cycles, I found that a cooling time was not required for zeolites as the air passed during adsorption cooled the bed more rapidly than it saturated with CO_2. This is a key consideration for TSA implementation since it is often the time limiting step during any TSA process[47] and increases bed utilization dramatically. Additionally, I provide a basic energy analysis for this process in the supporting information, and note that with green electricity this would be a carbon negative process.

Acknowledgement. I would like to extend our thanks to Praxair, Inc. for providing the Li-LSX pellets and K/Na-LSX powder.

REFERENCES

1. Lackner, K. S.; Grimes, P.; Ziock, H. Carbon dioxide extraction from air? Los Alamos National Laboratory, LAUR-99-5113, Los Alamos, NM, **1999**.
2. Keith, D. W. Why Capture CO2 from the Atmosphere? *Science.* **2009** *25*, 1654. DOI 10.1126/science.1175680
3. Zeman, F. S.; Keith, D. W. Carbon neutral hydrocarbons Philos. Trans. R. Soc. London, Ser. A **2008**, *366* (1882), 3901.
4. Choi, S.; Drese, J. H.; Eisenberger, P. M.; Jones, C. W. Application of Amine-Tethered Solid Sorbents for Direct CO2 Capture from the Ambient Air. *Environmental Science & Technology* **2011** *45* (6), 2420.
5. Satyapal, S.; Filburn, T.; Trela, J.; Strange, J. Performances and properties of a solid amine sorbent for carbon dioxide removal in space life support application. *Energy Fuels* **2001**, *15*, 250.
6. Belmabkhout, Y.; Serna-Guerrero, R.; Sayari, A. Amine-bearing mesoporous silica for CO_2 removal from dry and humid air. *Chem. Eng. Sci.* **2010**, *65* (11) 3695.
7. Van Wagener, D. H.; Rochelle, G. T. Stripper configurations for CO2 capture by aqueous monoethanolamine. *Chemical Engineering Research and Design* **2011.** DOI 10.1016/j.cherd.2010.11.01
8. Huang, H. Y.; Yang, R. T.; Chinn, D.; Munson, C. L. Amine-grafted MCM-48 and silica Xerogel as Superior Sorbents for Acidic Gases Removal from Natural Gas. *Ind. Eng. Chem. Res.* **2003**, *42*, 2427.
9. Chatti, R.; Bansiwal, A. K.; Thote, J. A.; Kumar, V.; Jadhav, P.; Lokhande, S. K.; Biniwale, R. B.; Labhsetwar, N. K.; Rayalu, S. S. Amine loaded zeolites for carbon dioxide capture: Amine loading and adsorption studies. *Microporous and Mesoporous Materials*. **2009**, *121*, 84.
10. Drese, J. H.; Choi, S.; Lively, R. P.; Koros, W. J.; Fauth, D. J.; Gray, M. L.; Jones, C. W. Synthesis–Structure–Property Relationships for Hyperbranched Aminosilica CO2 Adsorbents. *Adv. Funct. Mater*. **2009**, *19*, 3821.
11. Xu, X.C.; Song, C. S.; Andersen, J. M.; Miller, B. G.; Scaroni, A. W. *Energy Fuels*, **2002**, *16*, 1463.
12. Ma, X. L.; Wang, X. X.; Song, C. S. Molecular Basket Sorbents for Separation of CO2 and H2S from Various Gas Streams. *J. Am. Chem. Soc.* **2009**, *131*, 5777
13. Sayari, A.; Belmabkhout Y. Stabilization of Amine-Containing CO2 Adsorbents: Dramatic Effect of Water Vapor. *J. Am. Chem. Soc*. **2010**, *132*, 6212. DOI 10.1021/ja1013773
14. Xu, X.; Song, C.; Miller, B.G.; Scaroni, A.W. Influence of moisture on CO2 separation from gas mixtures by a nanoporous adsorbent based on polyethylenimine-modified molecular sieve MCM-41. *Ind. Eng. Chem. Res.* **2005**, *44*, 8113.
15. Maurer, R. T. Apparent Surface Diffusion Effects for Carbon Dioxide/Air and Carbon Dioxide/Nitrogen Mixtures with Pelleted Zeolite Beds. In *Adsorption and Ion Exchange with Synthetic Zeolites*. Flank, W. H. Ed.; American Chemical Society. 1980, p. 73.
16. Chue, K. T.; Kim, J. N.; Yoo, Y. J.; Cho, S. H.; Yang, R. T. Comparison of Activated Carbon and Zeolite NaX for CO2 Recovery from Flue Gas by Pressure Swing Adsorption. *Ind. Eng. Chem. Res.* **1995**, *34*, 591.

17. Kikkinides, E. S.; Yang R. T.; Cho, S. H. Concentration and Recovery of CO2 from Flue Gas by Pressure Swing Adsorption. *Ind. Eng. Chem. Res.* **1993**, *32*, 2714.
18. Li, G.; Xiao, P.; Webley, P.; Zhang, J.; Singh R.; Marshall M. Capture of CO2 from high humidity flue gas by vacuum swing adsorption with zeolite NaX. *Adsorption*. **2008**, *14*, 415 .
19. Siriwardane, R. V.; Shen M. S.; Fisher E. P.; Poston J. A. Adsorption of CO2 on Molecular Sieves and Activated Carbon. *Energy & Fuels* **2001**, *15*, 279.
20. Zhao, Z.; Cui, X.; Ma, J.; Li, R. Adsorption of carbon dioxide on alkali-modified zeolite NaX adsorbents. *Int. J. of Greenhouse Gas Control* **2007** *1* 355 .
21. Wang, Y.; LeVan, M. D. Adsorption Equilibrium of Carbon Dioxide and Water Vapor on Zeolites 5A and NaX and Silica Gel: Pure Components. *J. Chem. Eng. Data* **2009**, *54*, 2839.
22. Hutson, N. D; Yang, R. T. Influence of Residual Water on the Adsorption of Atmospheric Gases in Li−X Zeolite: Experiment and Simulation. *Ind. Eng. Chem. Res.*, **2000**, *39* (6), 1775. DOI 10.1021/ie990763z
23. Nikulshina, V.; Ayesa, N.; Galvez, M. E.; Steinfeld, A. Feasibility of Na-based thermochemical cycles for the capture of CO2 from air - Thermodynamic and thermogravimetric analyses. *Chem. Eng. J.* **2008**, *140* (1−3), 62.
24. Nikulshina, V.; Gebald, C.; Steinfeld, A. CO_2 capture from atmospheric air via consecutive CaO-carbonation and $CaCO_3$-calcination cycles in a fluidized-bed solar reactor. *Chem. Eng. J.* **2009**, *146* (2), 244.
25. Zeman, F. Experimental results for capturing CO_2 from the atmosphere *AIChE J.* **2008**, *54* (5), 1396.
26. Mahmoudkhani, M.; Keith, D. W. Low-energy sodium hydroxide recovery for CO_2 capture from atmospheric air-Thermodynamic analysis. *Int. J. Greenhouse Gas Control* **2009**, *3* (4), 376.
27. Sherman, S. R. Nuclear powered CO_2 capture from the atmosphere. *Environ. Prog. Sustainable Energy* **2009**, *28* (1), 52.
28. Murray, J.M.; Renfrew, C.W.; Bedi, A.; McCrystal, C.B.; Jones, D.S.; Fee, J.P.H. Amsorb. A new carbon dioxide absorbent for use in anesthetic breathing systems, *Anesthesiology* **1999**, *91*, 1342.
29. Stolaroff, J. K.; Keith, D. W.; Lowry, G. V. Carbon Dioxide Capture from Atmospheric Air Using Sodium Hydroxide Spray. *Environ. Sci. Technol.* **2008**, *42*, 2728.
30. Cengel, Y. A.; Boles, M. *Thermodynamics: An Engineering Approach*, 3rd ed.; McGraw-Hill Science/Engineering/Math, 1999.
31. Walton, K. S., and M. D. LeVan. A Novel Adsorption Cycle for CO2 Recovery: Experimental and Theoretical Investigations of a Temperature Swing Compression Process. *Separation Science and Technology*, 2006, 41, 485–500.
32. Yang, R. T. *Adsorbents Fundamentals and Applications*; Wiley: Hoboken, New Jersey, 2003.
33. Liang, Z.; Marc Marshall, M.; Chaffee, A. L.; CO2 Adsorption-Based Separation by Metal Organic Framework (Cu-BTC) versus Zeolite (NaX). *Energy & Fuels* **2009**, *23*, 2785. DOI 10.1021/ef800938e

34. Ma, S.; Zhou, H. C. Gas storage in porous metal–organic frameworks for clean energy applications. *Chem. Commun.* **2010**, *46*, 44.
35. Banerjee, R.; Phan, A.; Wang, B.; Knobler, C.; Furukawa, H.; O'Keeffe, M.; Yaghi, O. High-Throughput Synthesis of Zeolitic Imidazolate Frameworks and Application to CO2 Capture. *Science*. **2008**, *319*, 939. *DOI: 10.1126/science.1152516*
36. Yazaydın, A,; Benin, A. I.; Fahemm, S. A.; Jakubczak, P.; Low, J. J.; Willis, R. R.; Snurr, R. Q. Enhanced CO2 Adsorption in Metal-Organic Frameworks via Occupation of Open-Metal Sites by Coordinated Water Molecules *Chemistry of Materials*. **2009**, *21* (8), 1425-1430
37. Goj, A.; Sholl, D. S.; Akten, E. D.; Kohen, D. Atomistic Simulations of CO2 and N2 Adsorption in Silica Zeolites: The Impact of Pore Size and Shape. *J. Phys. Chem. B*. **2002**, *106* (33), 8367
38. Jee, S. E; Sholl, D. S. Carbon Dioxide and Methane Transport in DDR Zeolite: Insights from Molecular Simulations into Carbon Dioxide Separations in Small Pore Zeolites. *J. Am. Chem. Soc*. **2009**, *131* (22), 7896.
39. Yang W. C.; Hoffman J. Exploratory Design Study on Reactor Configurations for Carbon Dioxide Capture from Conventional Power Plants Employing Regenerable Solid Sorbents. *Ind. Eng. Chem. Res.* **2009**, *48*, 341
40. Tlili, N.; Grevillot, G.; Vallieres, C. Carbon dioxide capture and recovery by means of TSA and/or VSA NaX adsorbents. *Int. J. of Greenhouse Gas Control.* **2009**, *3*, 519.
41. Zhang, J.; Webley, P. A.; Xiao, P. Effect of process parameters on power requirements of vacuum swing adsorption technology for CO2 capture from flue gas. *Energy Conversion and Management*. **2008**, *49* (2), 346. DOI: 10.1016/j.enconman.2007.06.007.
42. Zhao, D.; Feng, J.; Huo, Q.; Melosh, N.; Fredrickson, G. H.; Chmelka, B. F.; Stucky, G. D. *Science*, **1998**, *279*, 548.
43. Hicks, J. C.; Drese, J. H.; Fauth, D. J.; Gray, M. L.; Qi, G. ; Jones, C. W. Designing Adsorbents for CO2 Capture From Flue Gas - Hyperbranched Aminosilicas Capable of Capturing CO2 Reversibly. *J. Am. Chem. Soc.* **2008**, *130*, 2902. DOI 10.1021/ja077795v.
44. Hartmann, M.; Vinu, A. Mechanical Stability and Porosity of Large-Pore SBA-15 Mesoporous Molecular Sieces by Mercury Porosimetry and Organics Adsorption. *Langmuir* **2002**, *18*, 8010.
45. Walton, K. S.; Abney, M. B.; LeVan, M. D. CO2 adsorption in Y and X zeolites modified by alkali metal cation exchange. *Micro and Meso Mat*. **2006**, *91*(1-3), 78. DOI: 10.1016/j.micromeso.2005.11.023.
46. Wang, Y.; Levan M. D. Adsorption Equilibrium of Carbon Dioxide and Water Vapor on Zeolites 5A and 13X and Silica Gel: Pure Components. *J. of Chem & Eng Data.* **2009,** *54* (10), 2839
47. Yang, R. T. *Gas Separation by Adsorption Processes*; Imperial College Press: London, 1999.
48. Crank, J. *The Mathematics of Diffusion;* Clarendon: Oxford, 1979; pp 89-92.
49. Hasegawa, Y.; Watanabe, K.; Kusakabe, K.; Morooka, S. The separation of CO2 using Y-type zeolite membranes ion-exchanged with alkali metal cations. *Sep and Pur Tech*. **2001**, *22*, 319. DOI: 10.1016/S1383-5866(00)00154-4
50. Leal, O.; Bolivar, C.; Ovalles, C.; Garcia, J. J.; Espidel, Y. Reversible Adsorption of Carbon Dioxide on Amine Surface-bonded Silica Gel, *Inorg. Chim. Acta,* **1995** *240*, 183.

51. Zhao, Z.; Cui, X.; Ma, J.; Li, R. Adsorption of carbon dioxide on alkali-modified zeolite 13X adsorbents. *Int J. of Greenhouse Gas Control*. **2007**, *1* (3), 355. DOI: 10.1016/S1750-5836(07)00072-2.
52. Li, W.; Choi, S.; Drese, J. H.; Hornbostel, M.; Krishnan, G.; Eisenberger, P. M.; Jones, C. W. Steam-Stripping for Regeneration of Supported Amine-Based CO_2 Adsorbents. *ChemSusChem*, **2010**, *3*, 899.

	Li-LSX	Na-LSX	K-LSX	Ca-LSX	NaX	NaY	CaY	Amine-grafted SBA-15
CO_2 Capacity 395ppm (mmol/g)	1.34	0.87	0.67	0.76	0.41	0.08	0.14	0.14
N_2 Capacity 0.8atm (mmol/g)	0.84	0.36	0.22	0.94	0.28	0.24	0.22	0.042
CO_2 heat of adsorption 395ppm (-kJ/mol)	51	45	43	39	40	30	46	65
CO_2 heat of adsorption zero loading (-kJ/mol)	63	55	48	60	56	45	47	65
N_2 heat of adsorption 0.8 atm (-kJ/mol)	22	15	12	25	14	13	21	20
D/R^2 Dry ($1x10^{-2}$/s)	2.2	N/A	1.6	N/A	2.4	N/A	N/A	0.043
D/R^2 Wet ($1x10^{-2}$/s)	N/A	N/A	N/A	N/A	N/A	N/A	N/A	0.014

Table 1. Table showing isotherm values (pure component) for measured materials and diffusion time constants (D/R^2) for CO_2 in powders (units of s^{-1}) at 25 ^oC. RH of 0% for dry and 80% for wet for promising adsorbents . (Wet adsorption was done using a gravimetric technique. Dry adsorption was done using a gravimetric technique and a sorptometer). On zeolites adsorption was too fast to use a gravimetric technique and not possible with the sorptometer. Error for heat of adsorption at 395ppm is ±2kJ/mol, for zero loading it is ±4kJ/mol.

	Li-LSX	K-LSX	NaX	Amine-grafted SBA-15
CO_2 Capacity 395ppm in air (mmol/g)	0.82	0.25	0.32	0.09
CO_2 Capacity 395ppm in wet air (mmol/g)	0.01	0.03	0	0.13
N_2 Capacity 0.8atm (mmol/g)	0.85	0.24	0.30	0.042

Table 2. Table showing measured capacities for pellets of the corresponding material (using 15% binder for zeolites).

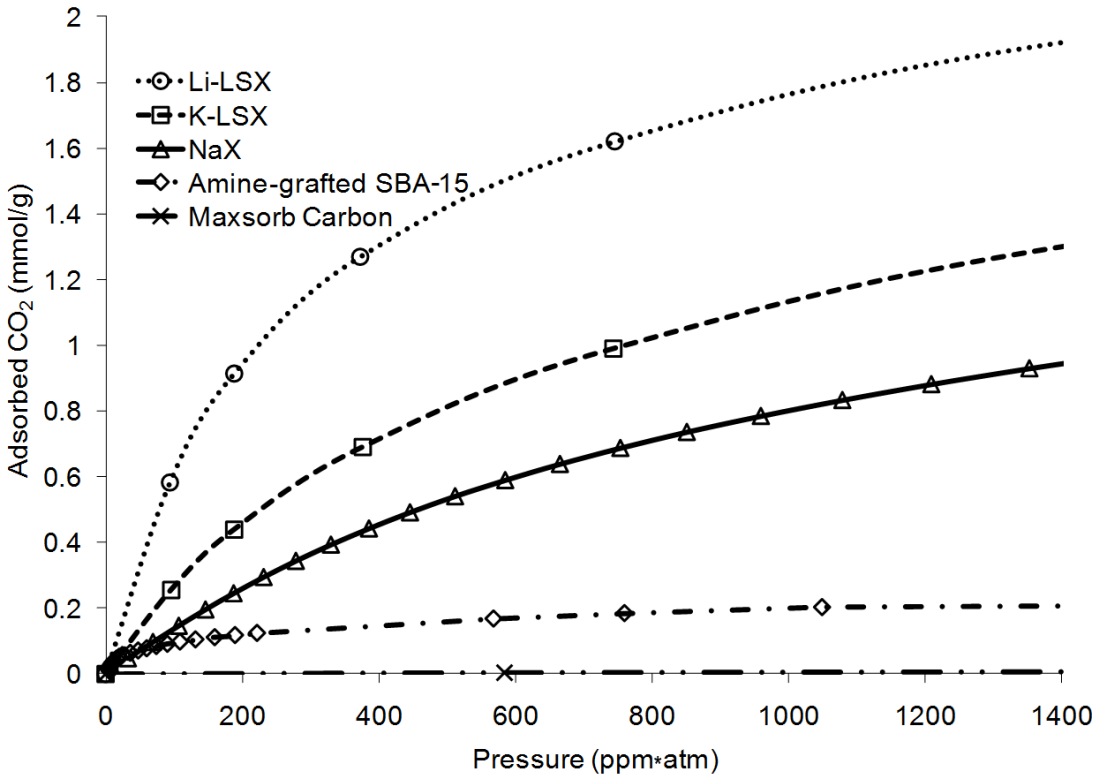

Figure 31. Low pressure pure component CO_2 isotherms at 25^{o}C on representative adsorbents studied. Zeolites have the largest capacity at 400ppm and amine-grafted SBA-15 has the highest heat of adsorption.

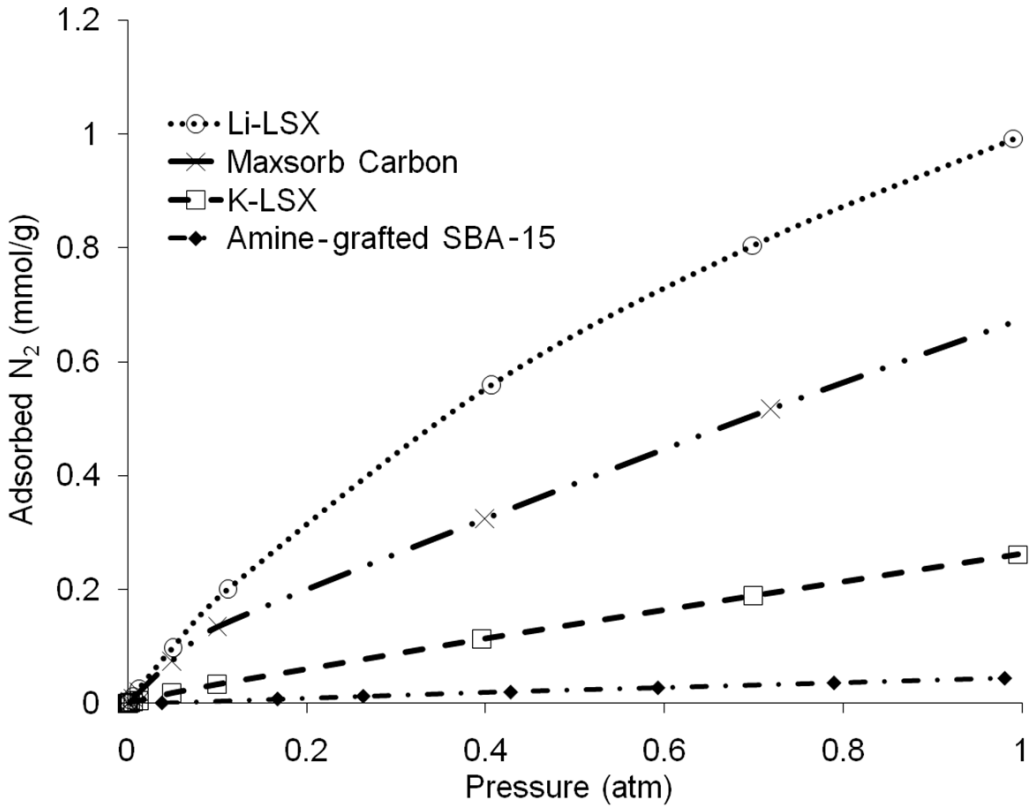

Figure 32. Pure component N_2 isotherms at 25°C on representative adsorbents. Zeolites have the largest capacity and amine-grafted silica the lowest.

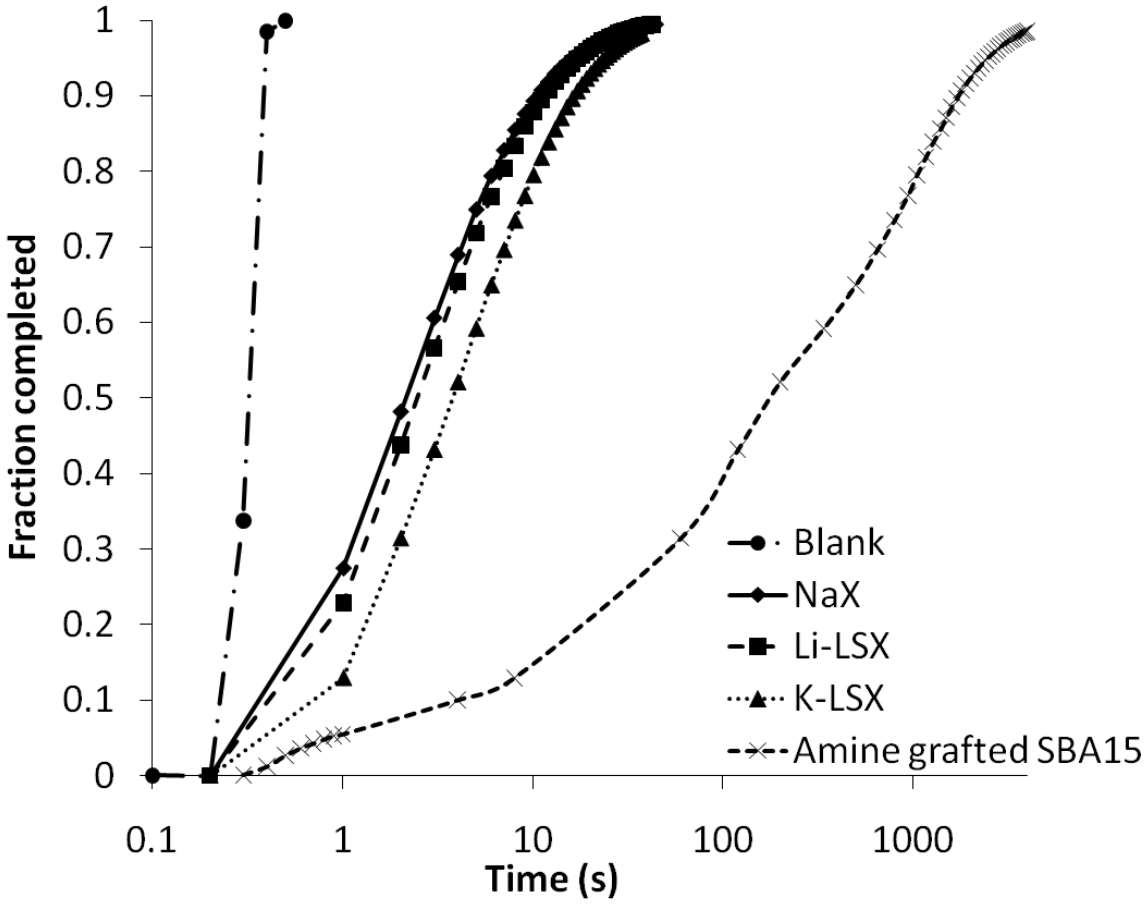

Figure 33. Adsorption rates for zeolites Li-LSX, K-LSX, NaX and Amine-grafted SBA-15 under dry conditions using pure CO_2, upon a step change in CO_2 pressure from 6.5×10^{-6} atm to 4.6×10^{-5} atm (or, 0.005 Torr to 0.035 Torr), at 25 ^{o}C. The gas was dosed at 0.2 s.

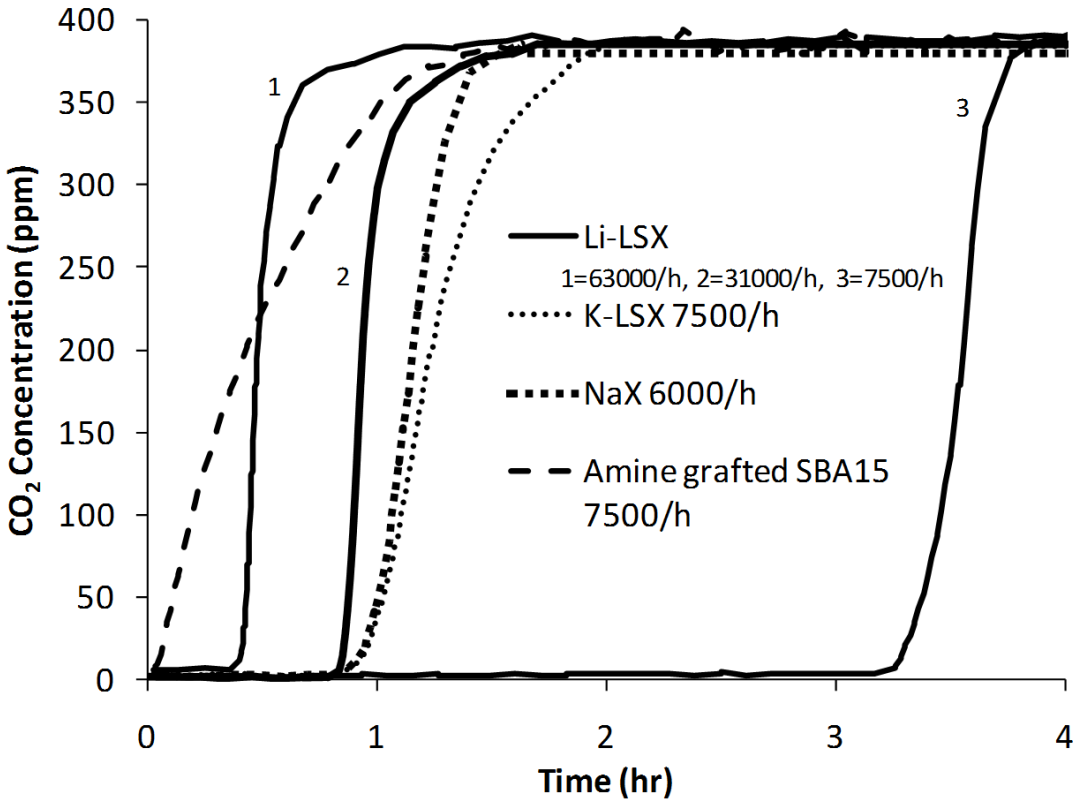

Figure 34. CO_2 breakthrough curves for ambient air feed with 395 ppm CO_2, at 1atm, 25ºC and RH 0.0% for gas-hourly space velocities above 5000 1/h. (CO_2 capacity at the breakthrough point for Li-LSX was 0.82 mmol/g for all space velocities)

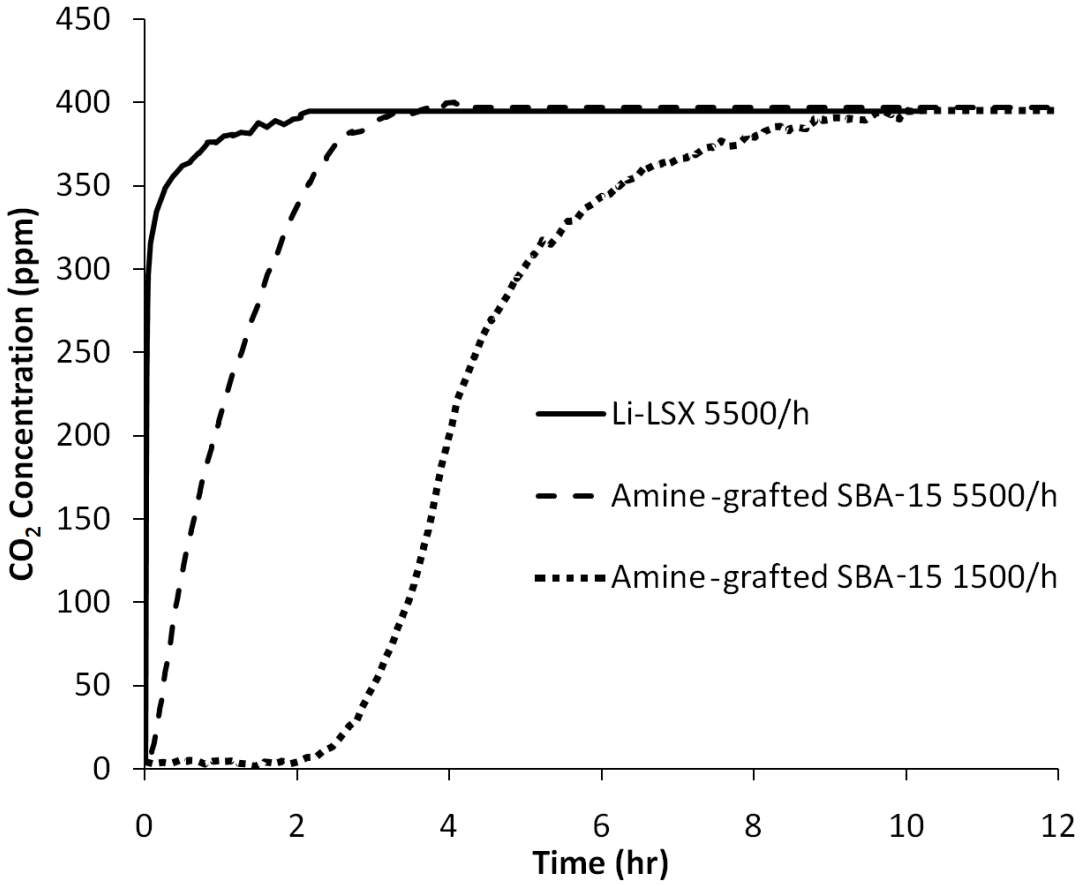

Figure 35. CO_2 breakthrough curves for ambient air with 395 ppm CO_2, at 1 atm, 25 ºC and RH 80%.

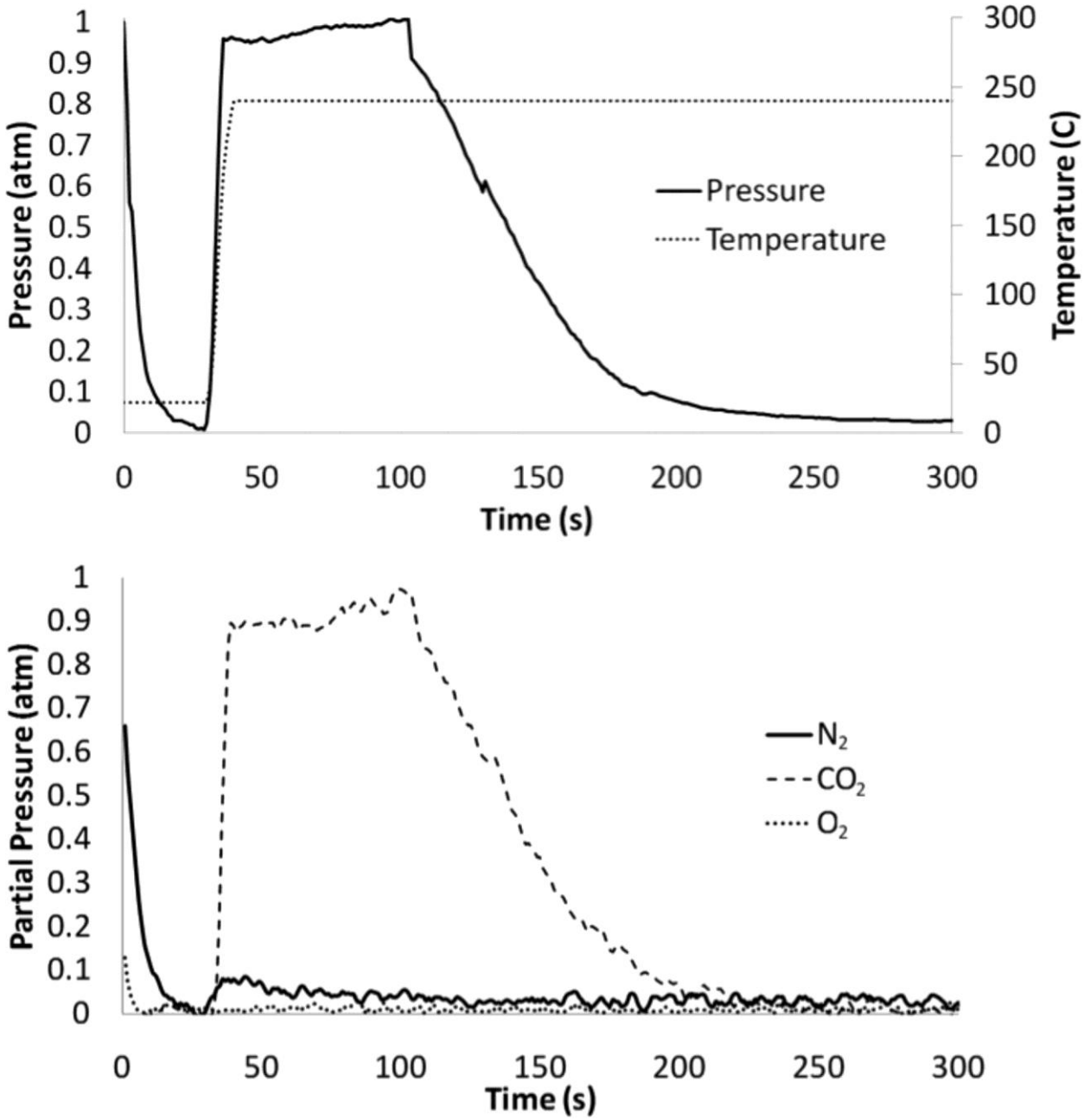

Figure 36. Desorption half-cycle for the combined temperature and vacuum swing process on Li-LSX. The bed was degassed to 0.01 atm and isolated. Then the bed was heated to 80 °C and allowed to vent when the pressure exceeded 1 atm. Degassing was reinitiated when the pressure dropped below 1 atm.

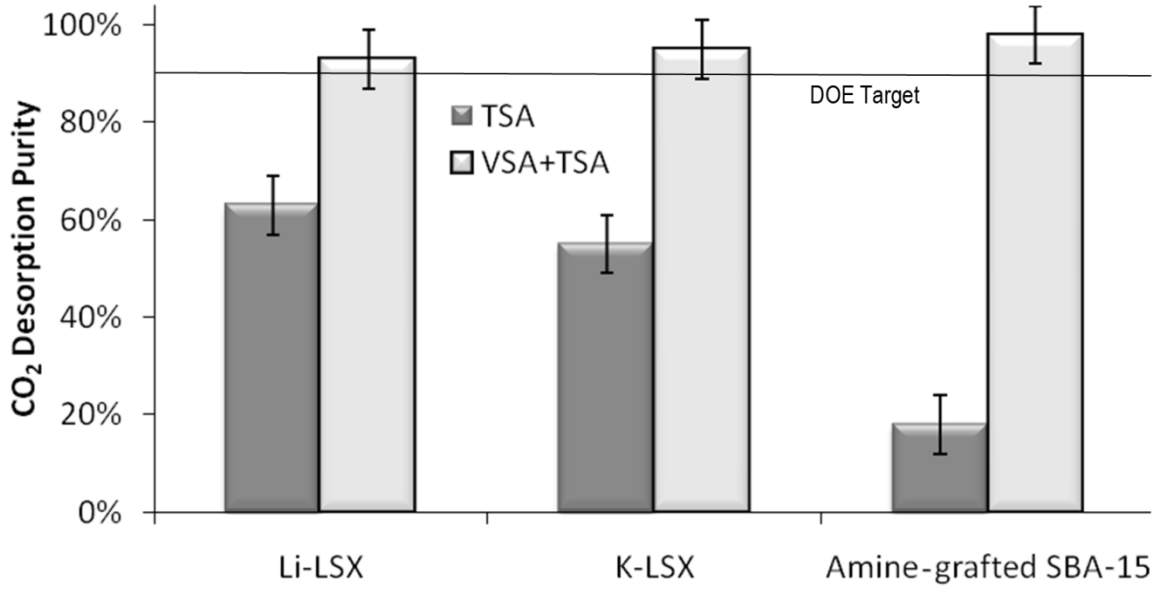

Figure 37. Desorption purity for CO_2 on a dry basis from the three most promising adsorbents/absorbents for single step TSA and a combined VSA/TSA process. Relative to the DOE target of 90% purity. [1] *For TSA, the bed temperature was raised quickly from 25 ^{o}C to 280 ^{o}C (for Li-LSX), 180 ^{o}C (for K-LSX) and 120 ^{o}C (for Amine-grafted SBA-15). For combined VSA/TSA, the bed was degassed from 1 atm to 0.01 atm then isolated and the temperature was increased from 25 ^{o}C to 240 ^{o}C (for Li-LSX), 220 ^{o}C (for K-LSX) and 120 ^{o}C (for Amine-grafted SBA-15). The value shown is the lowest concentration obtained during this procedure, during the CO_2 recovery stage.*

Chapter 5: CO_2 Capture from Atmosphere and Flue Gas Using Fixed Beds of Amine Grafted SBA15 and High Silica Type X Zeolite

Introduction

Atmospheric carbon dioxide capture and mitigation is gaining traction as a new last approach towards global carbon dioxide mitigation and also as a carbon source for renewable fuel production.[1] Additionally, transportation has been long targeted as a major source of carbon dioxide emissions. Recently Sherman et al. [2] and also Zeman et al.[3] proposed that instead of increasing the carbon load during production of fuel efficient vehicles that atmospheric capture could pose as a less intrusive method and potentially more efficient/less costly. This issue has been addressed with possible technologies such as hydroxide solution scrubbing[4,5] and amine based solid adsorbents.[6,7,8] Hydroxide solution scrubbing inherently operates best in high moisture environments where the loss of water is minimal. However, there is a shortage of land if this is to be the only method removing even a tenth of the CO_2 produced by transportation. This leaves room for amines, which function well in moderate humidity areas and zeolites which function better in low humidity areas. [9]

In an effort to address this idea we analyzed a series of commercially available adsorbents and evaluated their performance based on adsorption breakthrough curves and desorption carbon dioxide concentrations. Additionally, we optimized complete adsorption cycles for zeolites of interest and measured all known parameters that would have an impact on adsorption cycle performance. Our interest now focuses on modeling the previous results with a much wider variety of parameters.

Others have addressed the modeling aspect for flue gas capture using amines[10,11,12] and flue gas capture using zeolites.[13,14,15] The novelty here is the combination with atmospheric carbon dioxide removal primarily with amines, which have only recently been modeled by Kulkarni and

Sholl.[a] Zeolites for atmospheric removal are well studied and the traditional models fit well.[16,17,18] These will be used as the basis for our atmospheric breakthrough modeling. Breakthrough data was analyzed from our previous article[9] and new data was taken to evaluate the performance of the adsorbents in flue gas conditions. This provides a reference for the data/models to be evaluated against and also serves to strike a very distinct difference between the two problems. Additionally the modeling will raise a discrepancy between wet and dry conditions which will call into question a capacity difference between the two. Previously Huang et al as well as others found that moisture doubled the capacity of carbon dioxide adsorption on amine systems. This finding has been reported on some amine systems and not reported on others. Contradictions have been presented by Sayari and coworkers, Song and coworkers and Jones and coworkers who report a 0, 10 and 20 wt% increase in carbon dioxide storage capacity under wet conditions. Our work here presents the issue as a question of rates of adsorption and equilibration times used by the different groups which were limited by their measurement method.

Methods

Ion exchanged zeolites. Ion exchange was performed according to Hutson et al. [19] 250 mg of Na-LSX or was added to 50 mL water and heated with stirring. 2 mmol of Li hydroxide was added, followed by 5 mol of Li chloride. The solution was heated to 90 °C and stirred for 2 hours, then decanted. This was repeated 8 times. The solution was rinsed with DI water and decanted 5 times to ensure removal of the chloride solution. Surface area was compared to the starting material to test for retained crystalline structure. XRD patterns of prepared LSX zeolites are presented in the supporting information, also showing retained crystallinity.

SBA-15. Meoporous silica SBA-15 was prepared using the procedure reported by Zhao et al. [20] Four grams of Pluronic 123 was added to 144 mL of 1.7 M HCl at 40 °C and stirred until dissolved. 8 g of TEOS was then added and stirred for 2h. The sample was filtered then calcined at 385 °C for 4h or was extracted with 60 mL of ethanol (99.5%) and refluxed at 78 °C for 8 h. This extraction was repeated twice to remove the template.

SBA-15 grafted with low loadings of amine. SBA-15 was grafted with low amounts of 3-aminopropyltrimethoxysilane to ensure no pore blocking and accurate maximum rate

determination.[6] A procedure similar to Hicks et al.[21] was followed. 400 mg of SBA-15 was dissolved in 20 mL of anhydrous toluene while stirring and placed under nitrogen protection. 5mL of 3-aminopropyltrimethoxysilane was then added to the solution. The solution was stirred for 12 hours, then filtered and washed repeatedly with toluene. For high loadings the solution was refluxed for 12 hours at 80 °C. The sample was then dried under vacuum at 60 °C. A yield of 1 mmol/g amine loading was achieved, determined through weight loss analysis during decomposition on a thermogravimetric analyzer (TGA). Prepared by Lifeng Wang.

Pelletization. Pellets were formed for all samples by using compaction at 20MPa.[22] These discs were then crushed and sieved through a 30x50 mesh until sufficient material had been obtained.

Sample Preparation. Degas conditions were 400 °C for LiLSX and 120 °C for amine-grafted SBA-15. Samples were evacuated until a final pressure of 1.3×10^{-8} atm was achieved. All thermal conditions are of both the wall and the bed. Heating was carefully performed from the interior wall. The extreme importance of heating throughout these experiments is discussed more thoroughly in the supporting information.

Equilibrium Isotherms and Rates of Adsorption. Pure component isotherms and the BET surface areas were obtained using a Micromeritics ASAP 2020 sorptometer (which is a Sievert's volumetric technique). For the CO_2 isotherms, pressure ranged from 3×10^{-6} atm to 1 atm. Rates of adsorption were calculated using the same instrument. A pressure step from 6.5×10^{-6} atm to 4.6×10^{-5} atm (or, 0.005 Torr to 0.035 Torr) was selected for atmospheric capture rates. A pressure step from 0.08 atm to 0.1 atm was selected for flue gas capture rates. This corresponds to the rate of uptake for only the amine adsorption of CO_2 in the amine grafted SBA-15 (which was determined by background subtraction with pure SBA-15 and is shown in the supporting information). This was done such that the rates could be compared for the same pressure increase step for all sorbents. Additionally this pressure step was shown to have good agreement with the TGA analysis described below. It was noted that as loading increased, the rate of adsorption for amines slowed slightly (~10%). Further discussion of the rate measurement procedure is available in the supporting information.

Thermogravimetric Analysis (TGA). Total equilibrium adsorption amounts as well as adsorption rates were measured using a Shimadzu TGA-50 analyzer, under dry and wet conditions, for both atmospheric air and pure CO_2. The rate of adsorption was taken as a pressure step from 0 to 4×10^{-4} atm CO_2 at 25 °C or 1 atm CO_2 at 85 °C for both wet (R.H. 80%) and dry conditions, using a balance of N_2. The rate obtained for dry CO_2 for amine grafted SBA-15 at low pressure was identical to that obtained using the sorptometer. We assume that this indicates that this method provides accurate rate information under these conditions, as well as wet conditions. Time accuracy is approximately 0.01h. Weight accuracy is approximately 0.01wt%.

Atmospheric Air Fixed-Bed Adsorber Breakthrough Curves. Breakthrough curves were measured using a vertical, fixed bed with ambient air feed in a down-flow manner. The outlet CO_2 concentration was continually monitored with a Vaisala GMP220 probe. Additionally there was a pressure gauge located at the bed feed and a flow meter controlling the bed feed. Beds were set at 3“ (7.62 cm) in height, and ¼” (0.64 cm) diameter. Void factions were measured via helium displacement (assisted by the Micromeritics 2020) and had total void fractions of 70±3%. Beds were contained by using a small piece of quartz wool and a pinch in the glass neck, instead of a frit.

Flue Gas Fixed-Bed Adsorber Breakthrough Curves. Breakthrough curves were measured using a vertical, fixed bed with a mixture of N_2 and CO_2 in a down-flow manner. The concentration was controlled using two flow meters in parallel and the pressure was carefully controlled from the cylinder using two regulators in series. The outlet CO_2 concentration was continually monitored with a Vaisala GMT221 probe. Additionally there was a pressure gauge located at the bed feed and a flow meter controlling the bed feed. Beds were set at 3“ (7.62 cm) in height, and ¼” (0.64 cm) diameter. Void factions were assumed based on spherical bead packing. Beds were contained by using a small piece of quartz wool. Data from Lifeng Wang.

Modeling. Mathematical models were used from previous sources for the breakthrough performance of the adsorbents tested. For atmospheric conditions we assume the bed is isothermal. This is supported by the fact that the air flow rates in the system and thus heat capacity of the air itself, is more than 100 times the heating effects from the adsorption of the minute amount of carbon dioxide present. This isothermal assumption allows us to use purely

mathematical methods in order to determine the breakthrough performance and in turn derive performance equations for each of the parameters. We also assume isothermal performance for the flue gas conditions. This was a carefully considered assumption based on the isothermal results for 5 °C increases in temperature above room temperature (taken from data obtained by Jones and co-workers[10]). We concluded that the potential increase in temperature would not have a significant effect on the breakthrough performance, which we discuss later. Final analysis of all the parameters was then done to determine relative importance and applicable optimization techniques for the adsorbents.

Rosen Model. The Rosen model comes from the derivation of surface film diffusion resistance followed by intra-particle diffusion resistance.[23] The pellets are assumed to be uniform and constant in size. This model assumes a linear isotherm, which doesn't account for self sharpening breakthrough curves when the isotherm is of favorable type. The solution of Rosen model is given by: [24]

$$\frac{C}{C_0} = \frac{1}{2}\cdot\left[1 + \operatorname{erf}\left[\frac{\frac{3\cdot U}{2\cdot V} - 1}{2\left(\frac{1 + 5\cdot\upsilon}{5\cdot V}\right)^{\frac{1}{2}}}\right]\right] \tag{1}$$

$$U = \frac{2\cdot D_e\cdot\left(t - \frac{L}{u}\right)}{R_p^{\,2}} \tag{2}$$

$$V = \frac{3\cdot D_e\cdot K\cdot L}{u\cdot R_p^{\,2}}\cdot\left(\frac{\varepsilon}{1-\varepsilon}\right) \tag{3}$$

$$u = \frac{v}{\pi\cdot\left(\frac{D_i}{2}\right)^2}\cdot\left(\frac{1}{\varepsilon}\right) \tag{4}$$

$$\upsilon = \frac{D_e\cdot K}{k\cdot R_p} \tag{5}$$

Where D_e is the effective diffusivity (cm^2/s), R_p is the radius of the crystal (cm), L is the length of the bed (cm), ε is the void fraction in the bed (unitless), K is the Henry's law constant which is unit less for the liquid systems and used as a unit less fitting parameter here, u is the gas flow velocity (cm/s), v is the gas flow rate (cm^3/s) and k is the mass transfer coefficient (cm/s). The Rosen model was implemented in Excel.

The breakthrough capacity was taken from an average of the curves measured. The length of the bed was measured, as was the radius of the crystal (using TEM and XRD observation). The crystal diffusion was assumed to be the rate limiting step since the fit was significantly more accurate than the pore diffusion limitation assumption. This can be assumed since the diffusion resistance of gas inside the micron sized pores of the pellet would be significantly less than diffusion resistance of liquid as Rosen studied. The gas is most likely able to flow through the large channel pellet as part of the flow pathway through the bed, thus little diffusion resistance would be present. The effective diffusivity was taken from measurements on the sorptometer. The void fraction was calculated from the total bed voids without the measured inter-crystal voids, or assumed to be the same based on spherical packing. The mass transfer coefficient used CO_2 in air was 0.016 m/s.[25]

Thomas Model. The Thomas model is based on the assumption of a Langmuir isotherm, which accounts for the self sharpening nature of the isotherm, but this effect is primarily disregarded due to the assumption of a rate constant associated with adsorption.[26] This is particularly well suited to the adsorption of CO_2 on amine adsorbents due to the chemical reaction that takes place during adsorption. Diffusion effects are also accounted for in the case that this influences the kinetics. The solution to the Thomas model is given by: [27]

$$\frac{c}{c_0} = \frac{I_0\left(2\sqrt{A \cdot B \cdot x \cdot y}\right)}{I_0\left(2\sqrt{A \cdot B \cdot x \cdot y}\right) + \phi(B \cdot x, A \cdot y)} \tag{6}$$

$$\phi(u, v) = e^u \cdot \int_0^u e^{-t} \cdot I0\left(2 \cdot \sqrt{v \cdot t}\right) dt \tag{7}$$

$$B = \frac{k_1 \cdot a}{V} \tag{8}$$

$$A = \frac{k_2}{V} \tag{9}$$

$$y = V \cdot t - m \cdot x \tag{10}$$

Where I_0 is the modified Bessel function of the zeroeth order, k_1 and k_2 are kinetic constants with units $cm^3/(mmol*s)$ and 1/s respectively, a is sample capacity (mol/g), V is the volumetric flow rate (cm^3/s), m is the void volume of the sample per unit mass (cm^3/g), x is the mass of the sample (g), y is given by V*t-m*x, and t is time (s). The Thomas model was implemented in MathCad.

Hybridization of the models was done empirically through multiplication of the results. This was necessary for amine grafted adsorbents when it was apparent that two adsorption mechanisms were occurring simultaneously to give the full capacity of the adsorbent. The overall model would be explained by saying that the fraction of CO2 that is not captured by one mechanism is captured at the same rate by the other (this assumes a linear isotherm which we have already assumed).

Dual Adsorption Mechanism. Two mechanisms for adsorption of carbon dioxide on amines have been proposed.[28] The first is the zwitterion mechanism as follows:

$$R\text{-}NH_2 + CO_2 \rightarrow R\text{-}NH\text{-}COOH \tag{11}$$

$$R\text{-}NH\text{-}COOH + R\text{-}NH_2 \rightarrow R\text{-}NH\text{-}COO^- + R\text{-}NH_3^+ \tag{12}$$

The second mechanism is the base catalyzed mechanism as follows:

$$R\text{-}NH_2 + H_2O + CO_2 \rightarrow R\text{-}N(^+)H_3\text{-}CO_3H(^-) \tag{13}$$

While both mechanisms have been studied for aqueous amine solutions, little work has been done on amine grafted systems. The differences would primarily express themselves as the interaction between amines which are now immobilized, and formation of carbonate which now must remain on the surface of the silica, rather than being stabilized in solution.

Results

The isotherms, volumetric rates of adsorption and TGA rates of adsorption are given in the supporting information and previously explained. The breakthrough curves for atmospheric capture are shown in Figure . In this figure, we show the results for LiLSX at dry conditions under varying flow rates. The breakthrough curves appear to sharpen as the flow rate increases

and all exhibit relatively sharp curves, taking less than one tenth of the saturation time and accounting for less than one twentieth of break through capacity. This figure also shows the break through capacities for low loading amine grafted SBA15. These curves show the adsorption capacity of amines is mostly during the breakthrough (at similar flow rates) and thus the breakthrough capacity is relatively very low. At lower flow rates the breakthrough begins to sharpen, but not to that of LiLSX. It is also shown here that the capacity for amines is higher in wet conditions.

In Figure 39, the Rosen model is plotted for LiLSX at the conditions measured. The breakthrough capacity is taken from an average of the curves measured. The length of the bed was measured (3"), as was the radius of the crystal (2 micron). The effective diffusivity was taken from measurements on the sorptometer ($1.3*10^{-8}$ cm^2/s). The void fraction was calculated from the total bed voids (0.7) without the intra-crystal voids (0.25). The mass transfer coefficient was taken from Perry's for CO_2 in air (0.016 m/s).[25] The Rosen model was able to predict the concentration and time of the breakthrough to within 10%, which is within the error of the breakthrough curves. This demonstrates the accuracy of the model and verifies the assumptions made. While there are more complex methods to model the breakthrough capacity, this model works well due to the isothermal conditions and close fitting of the isotherm to Henry's law.

The Rosen model was also applied to low loading amine grafted SBA15 at atmospheric conditions and shown in Figure 40. The same parameters were used except the effective diffusivity ($8*10^{-11}$ cm^2/s) and the radius of the crystal (4 micron). The model was not able to accurately predict the breakthrough curves to greater than 30% of their value. This suggests that while the model expected much sharper breakthrough curves, a mechanism other than diffusion is most likely slowing adsorption. In this case we know that amines react in two pathways as stated earlier. The indication here is that those reactions are slower than the rate of diffusion. For this reason, the Thomas model was chosen and tested. The capacities were matched to the equilibrium measurements, with the ratio of the reaction coefficients (k_1/k_2) set to the breakthrough capacity. Then the reaction constants were fit to the breakthrough curves providing only one extra degree of freedom over the Rosen model. The results show a

significantly more accurate fit, potentially due to the extra fitting parameter, but more likely due to the accurate accounting of the rate of reaction. When we examine the reaction rates that were fit to this curve, we can observe that k_2 at 0.024 1/s fits the inverse of the adsorption halftime measured on the sorptometer. Essentially we can solve the Thomas model using only the same fitting parameters as used for the Rosen model, all of which are measured independently, except the breakthrough capacity.

In Figure 41, the breakthrough curves for LSX and amine grafted SBA15 are presented. In dry conditions LSX preserves about 85% of its isothermal equilibrium capacity and amine grafted SBA15 only 35%. In wet conditions the capacity of amine grafted SBA15 rose to 60% of equilibrium capacity. It is also noted that the increase in capacity came at a much slower rate as identified by spreading of breakthrough curve. Additionally this curve is not symmetrical.

For the LSX curves, the Rosen model was fit as explained earlier with a crystal size of 2 micron, effective diffusivity of $1.3*10^{-8}$ cm^2/s, bed voids of 0.35 and mass transfer coefficient of 0.016 m/s. This is shown in Figure 42. The model again fits within 10% of the measurement; however there are two interesting phenomena that the model is most likely not taking into account. The first is the self sharpening of the bed due to the very favorable adsorption isotherm of this material. This causes the initial part of the breakthrough to sharpen with increasing bed length and which is ignored by the model (the assumption of a linear isotherm). The second is the tail end of the breakthrough curve. While typically this is not as important to model accurately, typically process cycle ending once breakthrough starts, some work has been done by Jones and co-workers[10] detailing the significance of the non-isothermal state of the bed and the role it has in explaining this tail. Unfortunately, the measurements here are not of the accuracy necessary to fit parameters and the bed temperature was not measured. Their model was shown to accurately account for this effect in their systems during adiabatic adsorption and could explain the observation here.

43 shows the results for the Rosen and Thomas model for the amine system in flue gas conditions. With high loading amine SBA15 under wet conditions we see the breakdown of both models with the lack of accurate prediction of this breakthrough curve. Due to the indications that the sorptometer could provide accurate information for the k_2 reaction

constant, we measured this and found a k_2 of 0.42 1/s. Using the TGA we measured the adsorption rate for a moisture saturated (at 80% R.H.) sample and found a k_2 of 0.024 1/s. Using these values and the others previously determined, we were able to fit the models only to the breakthrough capacity. We show that both models fit within 30% of the breakthrough curve for all conditions, with the Rosen model more accurate for the dry conditions and the Thomas model more accurate for the wet conditions. Again the Rosen model does not accurately fit the tail of the breakthrough curve however the explanation may lie in the dissection of the dual reaction pathways for adsorption.

For the amine sample in wet conditions we find that the capacity is increased and that this increase in capacity more closely fits a model that takes into account rates of reaction. If we assume that this means the adsorption pathway that includes moisture is slower than the pathway for two amines, we can find that the amine in wet conditions is most accurately modeled by the combination of the Thomas and the Rosen model. The Rosen model was fitted to predict the dry breakthrough capacity and the Thomas model to encompass the entire capacity. By multiplication of the two normalized breakthrough concentrations we can construct a dual site breakthrough curve. This is demonstrated in the third graph of Figure . The slower rate of adsorption for the water-amine reaction can also explain the results obtained for the low loaded amine. Since the loading of amine is very low, the most likely method of adsorption even in dry conditions is through the base catalyzed pathway with this interaction facilitated by the surface silanol groups. This would lead to no observable difference between the adsorption rates of wet and dry conditions and matches our findings.

Additional evidence to support this theory comes from the measured rates of adsorption using the TGA and sorptometer. In dry conditions on both instruments the adsorption is very rapid and plateaus within a couple minutes but at roughly ½ of the capacity of wet conditions for the same time. This is shown clearly in Figure for the TGA measurement. Over the course of 4 hours, additional adsorption leads to full equilibrium capacity. If this sample is then exposed to moisture, the weight gain is consistent with the water capacity of the silica support. If both carbon dioxide and water are exposed to the sample at the same time, even at the same flow rate adsorption is slowed, however the adsorption capacity at 10 minutes is almost double that

of dry carbon dioxide and approximately equal to that of dry carbon dioxide after 4 hours of adsorption.

The rate of adsorption in the TGA in the presence of moisture exactly mirrors the breakthrough results of the wet breakthrough performance. Both are slow leading to longer adsorption times and more exaggerated breakthrough curves. The faster rate for dry CO_2 mirrors the dry breakthrough performance, which shows rapid adsorption for the first minute which leads to a sharp breakthrough curve (the slow rate of adsorption is not distinguishable by our breakthrough apparatus). Since the match is the same, we can use the TGA to extract more information on the desorption performance of the adsorbents. Figure shows desorption time as a function of saturation time, meaning that we start desorption after exposing the sample to the adsorption phase for (2min, 1h, and 12h). What we can see put very simply is fast on means fast off. We expect working capacity of the adsorbent will be most likely dictated by this faster adsorption mechanism. Since simple observation shows we can run a cycle with the faster mechanism more than 1000 times during a cycle for the slower mechanism. Therefore the first adsorption mechanism will dictate total adsorbent performance due faster adsorption and faster desorption. The second adsorption mechanism will most likely be parasitic capacity. It becomes imperative then that if neighboring amines (the zwitterion mechanism) are responsible for the faster rate. We can predict that if we fully utilize all amine capacity by only grafting geminal or vicinal amines, we can double the working capacity.

Further rate desorption information for wet amine systems shows that the desorption rate is slower when moisture is present, which matches slower adsorption rates. At this point most of the discussion is speculative since we cannot distinguish the adsorbed phase and if left in moist helium long enough the sample desorbs all species, contrary to what we found for adsorption of moisture in helium which saturated at 4wt%. Neither of these can be explained at this time. However for completeness this information is shown in Figure which shows the desorption rate for moist conditions under different total loadings of moist CO_2 (we assume CO_2 is the dominate species). Since the rate does not change with loading amount, we assume that only one mechanism is present for adsorption under moist conditions. This mechanism would need to result in an adsorbed state that is significantly lower in total energy than in dry conditions,

since the rate of adsorption in moist conditions is noticeably slower than in dry. This can also show that the moist mechanism and dry mechanism are competing mechanisms. Under wet conditions it may be that only the moist mechanism is observed and there is a considerable loss in adsorption and desorption rate for amines, versus the well reported dry conditions. Figure also shows the special case where CO_2 with moisture is momentarily switched to pure CO_2 at which point the adsorption rate spikes. The gas is then switched back to CO_2 with moisture and the adsorption rate slows, again potentially showing competing adsorption.

Overall we can try to explain previous experiments with these findings. Since we know that rates of adsorption may change due to diffusion resistances; we can simply say that we see an increase in the rate of adsorption of carbon dioxide with moisture for capacities above half of the equilibrium capacity in dry conditions. Thus if one does not wait long enough to saturate the adsorbent with pure carbon dioxide, moisture would give the impression of an increase in capacity, which may have been what others reported.

There are three potential issues with these experiments. The first is that we are assuming moisture does not leak into the TGA system from the ambient atmosphere. This is carefully validated by experiments in the supporting information showing that over the course of 20 hours, at the same flow rate used here, less than 1wt% water is adsorbed onto zeolite Li-LSX. Li-LSX is known to have one of the strongest binding energies for water of adsorbents and far stronger than amines and silica. The second assumption is that carbon dioxide binds to amines more strongly than moisture. While this has been previously demonstrated, we take the case where the adsorbent is exposed to moisture, then to carbon dioxide. As can be seen in Figure , the increase in total adsorption due to moisture is a small fraction of total adsorption of CO_2. For the opposite case, a sample saturated with moisture sees a large increase in total adsorption capacity. The third assumption is that for adsorption of moisture in helium, the helium mixture contains no carbon dioxide leaked in from the atmosphere. We tested this using the Vaisala low partial pressure CO_2 probe to measure the CO_2 concentration of this stream. We found that initial CO_2 levels were around 200ppm but quickly reduced to 2ppm over 10 seconds. Still this may be sufficient to enable the adsorption of moisture for the adsorbent which otherwise would not happen, further work on this would be encouraged.

Conclusion

We have now accurately modeled the breakthrough curves for CO_2 on amines and zeolites in atmospheric conditions and dry low temperature flue gas conditions. The models illuminated the difference in adsorption rates for amines in dry conditions and amines in wet conditions. This gives rise to the possible explanation that adsorption due to the base catalyzed mechanism is slower than through the zwitterion mechanism, and may explain previous discrepancies in adsorption rate measurements and total capacity measurements in humid conditions. We have also shown favorable desorption of CO_2 to occur only for the faster zwitterion mechanism.

In summary, for the dry conditions (we assume the zwitterion pathway) it would appear that the adsorption rate is still very rapid, but not diffusion limited under the most favorable conditions. This still supports the observations by Song and co-workers for dry amine based systems.[29] For the slower rate, it is very evident now that it is a reaction step that is rate limiting. The total amount of adsorption due to both steps also correlates with amine loading amount. For wet systems improvement is observed in the rate of adsorption but not in total capacity. This matches what others have observed ranging from no noticeable increase in capacity, to a doubling of capacity if we take into account the time previous experiments waited for equilibrium capacity.[21,29,30]

Finally, if the need arose to further derive breakthrough data without measuring the actual performance, we have found that the Dual Process Langmuir model accurately predicted the breakthrough capacity of the adsorbents measured here (this is demonstrated in the supporting information). This is detailed by Ritter and co-workers,[31] and can be joined with information in our previous work to fully solve all breakthrough curves for the adsorbents measured (LiLSX, NaLSX, KLSX, CaLSX, NaX, NaY, Amine-SBA15, activated carbon AX-21, activated carbon Maxsorb).

REFERENCES

1. Keith, D. W. Why Capture CO2 from the Atmosphere? *Science.* **2009** *25*, 1654. DOI 10.1126/science.1175680
2. Sherman, S. R. Nuclear powered CO_2 capture from the atmosphere. *Environ. Prog. Sustainable Energy* **2009**, *28* (1), 52.
3. Zeman, F. S.; Keith, D. W. Carbon neutral hydrocarbons Philos. Trans. R. Soc. London, Ser. A **2008**, *366* (1882), 3901.
4. Stolaroff, J. K.; Keith, D. W.; Lowry, G. V. Carbon Dioxide Capture from Atmospheric Air Using Sodium Hydroxide Spray. *Environ. Sci. Technol.* **2008**, *42*, 2728.
5. Nikulshina, V.; Gebald, C.; Steinfeld, A. CO_2 capture from atmospheric air via consecutive CaO-carbonation and $CaCO_3$-calcination cycles in a fluidized-bed solar reactor. *Chem. Eng. J*. **2009**, *146* (2), 244.
6. Choi, S.; Drese, J. H.; Eisenberger, P. M.; Jones, C. W. Application of Amine-Tethered Solid Sorbents for Direct CO2 Capture from the Ambient Air. *Environmental Science & Technology* **2011** *45* (6), 2420.
7. Satyapal, S.; Filburn, T.; Trela, J.; Strange, J. Performances and properties of a solid amine sorbent for carbon dioxide removal in space life support application. *Energy Fuels* **2001**, *15*, 250.
8. Belmabkhout, Y.; Serna-Guerrero, R.; Sayari, A. Amine-bearing mesoporous silica for CO_2 removal from dry and humid air. *Chem. Eng. Sci.* **2010**, *65* (11) 3695.
9. Stuckert, Nicholas R. and Yang, Ralph T. *CO2 Capture from the Atmosphere and Simultaneous Concentration using Zeolites and Amine Grafted SBA-15*. *Environ. Sci. Technol.*, **2011**, *45* (23), pp 10257–10264. **2011. DOI:** 10.1021/es202647a
10. Bollini, P.; Brunelli, N. A.; Didas, S. A.; Jones, C. W. Dynamics of CO2 Adsorption on Amine Adsorbents. 1. Impact of Heat Effects. *Ind. Eng. Chem. Res.*, **2012**, 51 (46), pp 15145–15152. **DOI:** 10.1021/ie301790a
11. Serna-Guerrero, R.; Sayari, A. Modeling Adsorption of CO2 on Amine-functionalized Mesoporous Silica. 2: Kinetics and Breakthrough Curves *Chem. Eng. J.* **2010**, 161, 182
12. Pirngruber, G. D.; Cassiano-Gaspar, S.; Louret, S.; Chaumonnot, A.; Delfort, B. Amines immobilized on a solid support for postcombustion CO2 capture–A preliminary analysis of the performance in a VSA or TSA process based on the adsorption isotherms and kinetic data. *Energy Procedia*. **2009**, *1*, (1), 1335.
13. Li, G.; Xiao, P.; Webley, P.; Zhang, J.; Singh R.; Marshall M. Capture of CO2 from high humidity flue gas by vacuum swing adsorption with zeolite NaX. *Adsorption*. **2008**, *14*, 415 .
14. Tlili, N.; Grevillot, G.; Vallieres, C. Carbon dioxide capture and recovery by means of TSA and/or VSA NaX adsorbents. *Int. J. of Greenhouse Gas Control.* **2009**, *3*, 519.
15. a.) Zhang, J.; Webley, P. A.; Xiao, P. Effect of process parameters on power requirements of vacuum swing adsorption technology for CO2 capture from flue gas. *Energy Conversion and Management*. **2008**, *49* (2), 346. DOI: 10.1016/j.enconman.2007.06.007.
    b.) Kulkarni and Sholl. Analysis of Equilibrium-Based TSA Processes for Direct Capture of CO2 from Air. *Ind. Eng. Chem. Res.* **2012**, *51*, 8631.

c.) Yang, R. T. *Gas Separation by Adsorption Processes*; Imperial College Press: London, **1999**.
d.) Wang, Y.; Levan M. D. Adsorption Equilibrium of Carbon Dioxide and Water Vapor on Zeolites 5A and 13X and Silica Gel: Pure Components. *J. of Chem & Eng Data.* **2009,** *54* (10), 2839
e.) Walton, K. S.; Abney, M. B.; LeVan, M. D. CO2 adsorption in Y and X zeolites modified by alkali metal cation exchange. *Micro and Meso Mat*. **2006**, *91*(1-3), 78. DOI: 10.1016/j.micromeso.2005.11.023.
f.) Hutson, N. D; Yang, R. T. Influence of Residual Water on the Adsorption of Atmospheric Gases in Li−X Zeolite: Experiment and Simulation. *Ind. Eng. Chem. Res.*, **2000**, *39* (6), 1775. DOI 10.1021/ie990763z
g.) Zhao, D.; Feng, J.; Huo, Q.; Melosh, N.; Fredrickson, G. H.; Chmelka, B. F.; Stucky, G. D. Triblock Copolymer Syntheses of Mesoporous Silica with Periodic 50 to 300 Angstrom Pores. *Science*, **1998**, *279*, 548.
h.) Hicks, J. C.; Drese, J. H.; Fauth, D. J.; Gray, M. L.; Qi, G. ; Jones, C. W. Designing Adsorbents for CO2 Capture From Flue Gas - Hyperbranched Aminosilicas Capable of Capturing CO2 Reversibly. *J. Am. Chem. Soc.* **2008**, *130*, 2902. DOI 10.1021/ja077795v.
i.) Hartmann, M.; Vinu, A. Mechanical Stability and Porosity of Large-Pore SBA-15 Mesoporous Molecular Sieces by Mercury Porosimetry and Organics Adsorption. *Langmuir* **2002**, *18*, 8010.
j.) Rosen, J. B. Kinetics of a Fixed Bed System for Solid Diffusion into Spherical Particles. *J. Chem. Phys.* **1952**, *20*, 387
k.) Rosen, J. B. General Numerical Solution for Solid Diffusion in Fixed Beds. *Ind. Eng. Chem.* **1954**, *46*, 1590
l.) Green, Don W.; Perry, Robert H. Perry's Chemical Engineers' Handbook (8th Edition). McGraw-Hill. **2008**.
m.) Thomas, H. C. Heterogeneous Ion Exchange in a Flowing System. *J. Am. Chem. Soc.* **1944**, *66*, 1664.
n.) Thomas, H. C. Chromatography: a Problem in Kinetics *Annals New York Academy of Science.* **1948**, *49,* 161
o.) Vaidya, P. D.; Kenig, E. Y. CO2-Alkanolamine Reaction Kinetics: A Review of Recent Studies *Chem. Eng. Technol.* **2007**, 30, (11), 1467.
p.) Xu, X.; Song, C.; Miller, B.G.; Scaroni, A.W. Influence of moisture on CO2 separation from gas mixtures by a nanoporous adsorbent based on polyethylenimine-modified molecular sieve MCM-41. *Ind. Eng. Chem. Res.* **2005**, *44*, 8113.
q.) Belmabkhout, Y.; Serna-Guerrero, R.; Sayari, A. Amine-bearing mesoporous silica for CO_2 removal from dry and humid air. *Chem. Eng. Sci.* **2010**, *65* (11) 3695.
r.) Ritter, J. A.; Bhadra, S. J.; Ebner, A. D. On the Use of the Dual-Process Langmuir Model for Correlating Unary Equilibria and Predicting Mixed-Gas Adsorption Equilibria. *Langmuir*, **2011**, 27 (8), 4700. DOI: 10.1021/la104965w

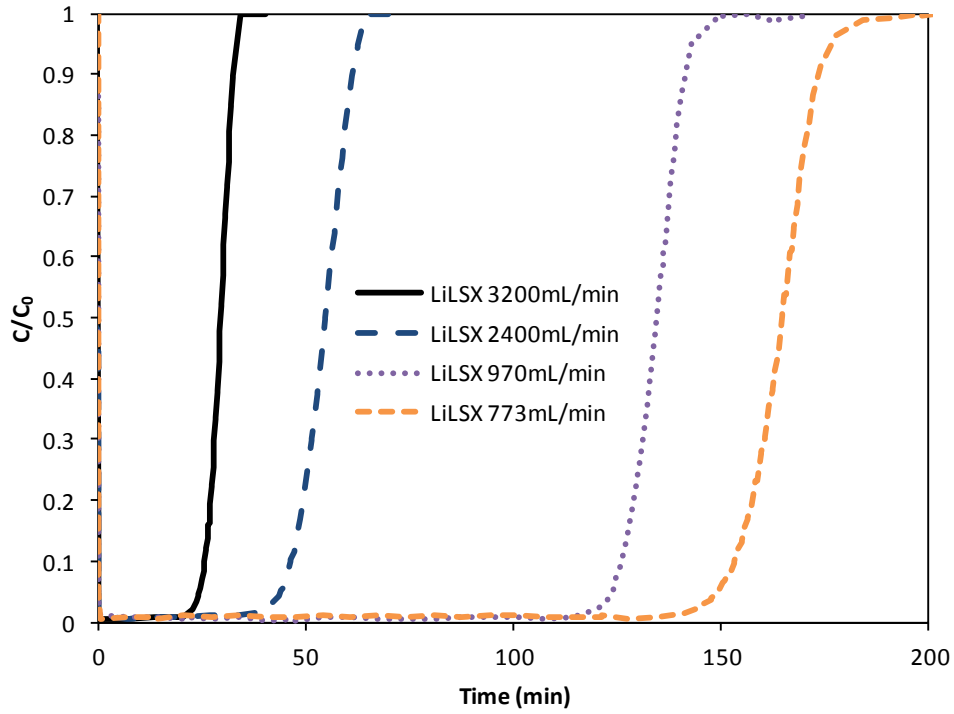

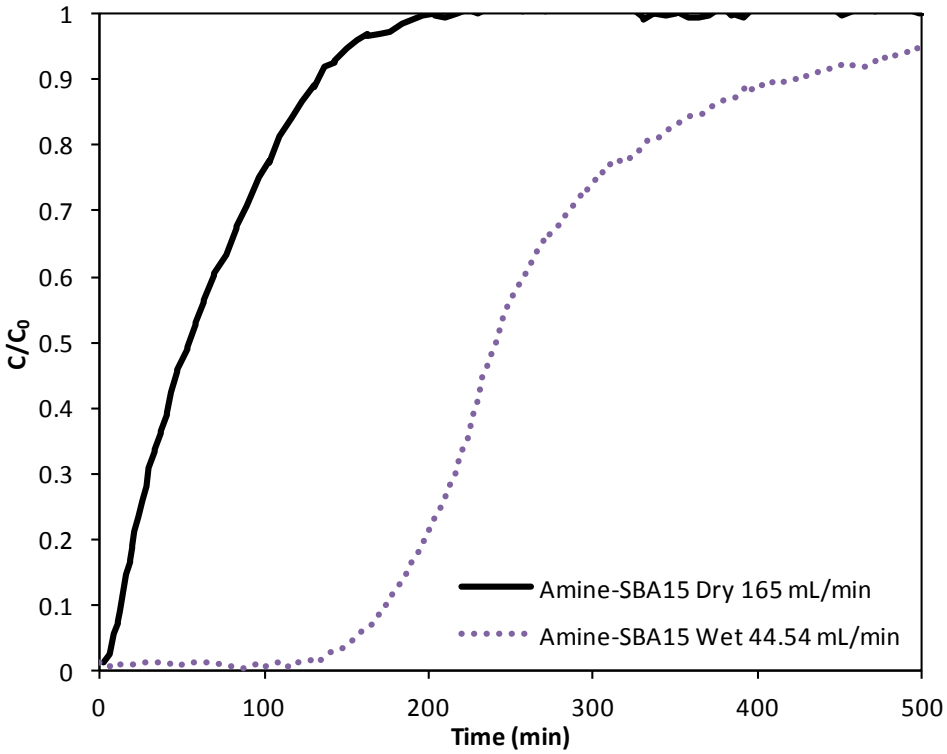

Figure 38 Breakthrough curves for atmospheric capture, for LiLSX (top) and low loading amine grafted SBA-15 (bottom). Conditions were 420ppm CO_2 in air dried by passing through a 3A bed that had been regenerated at 315°C for 8 hours in flowing air. For wet conditions R.H. was then set to 80%. 2.8g of LiLSX was used and 3.2g of amine sorbent was used.

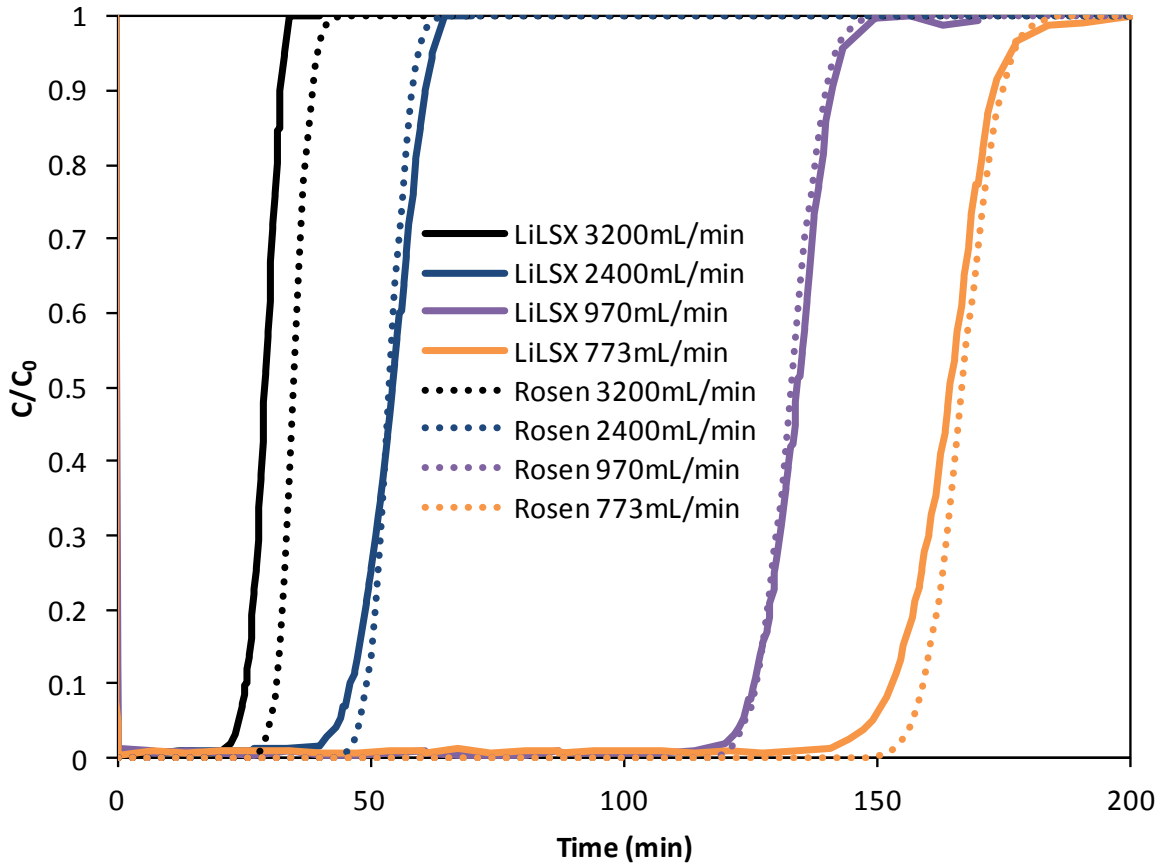

Figure 39 Rosen model fit for LSX at dry atmospheric conditions. The model was fit to the average breakthrough capacity of the isotherms and all other parameters were found through other measurements, not related to the breakthrough curves. Discrepancy between 3200mL/min and all other flow rates could potentially be caused by the need to use a different flow meter in order to obtain the high flow rate.

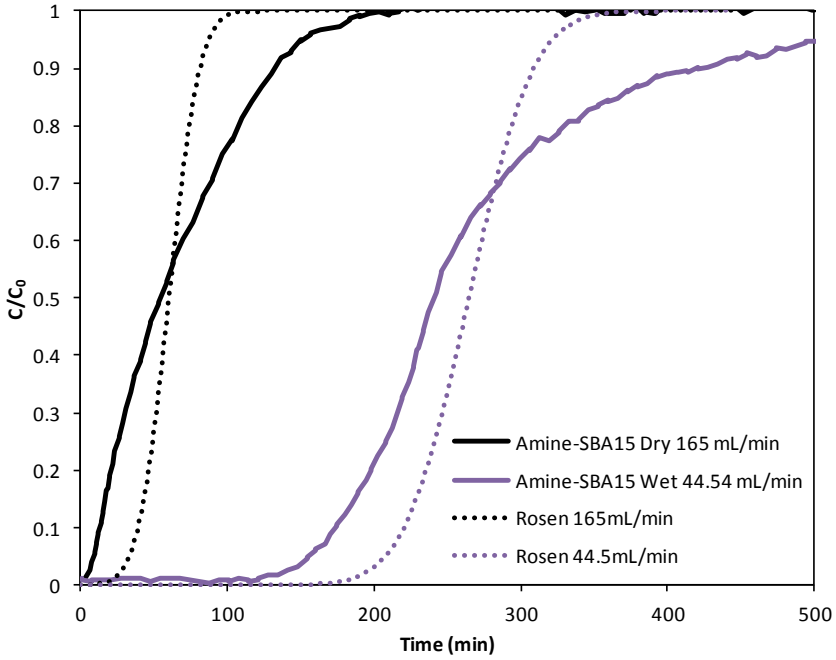

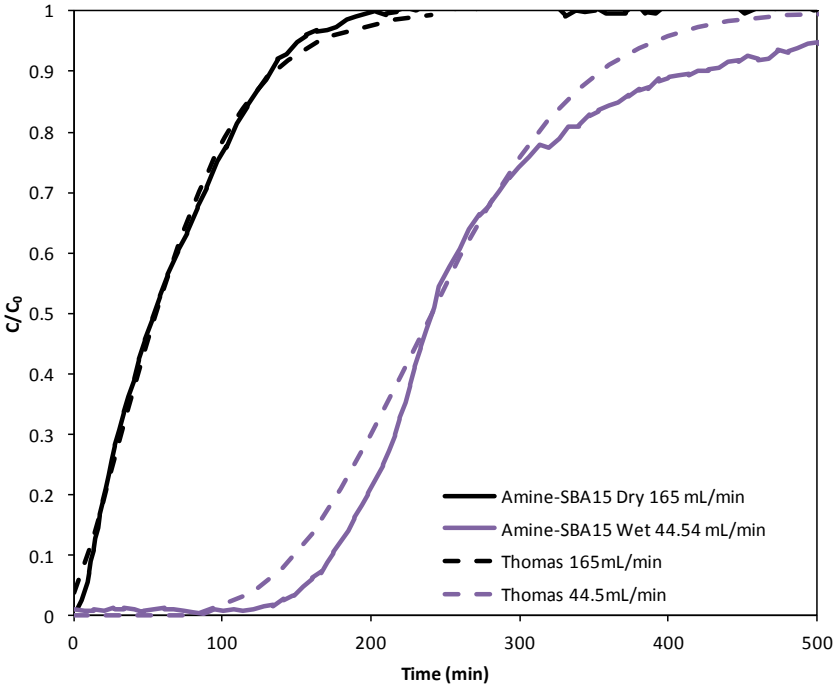

Figure 40 Modeling fit for Amine at atmospheric conditions (Rosen and Thomas). The Rosen model was fit to the breakthrough capacity of each measurement separately since they were at different conditions (wet vs dry) and had previously known different capacities. The faster rates for dry conditions were not observed here, possibly due to the low amine loading content and therefore lack of the zwitterion adsorption pathway. It is assumed then that adsorption in dry conditions was due to amine interaction with a surface silanol group.

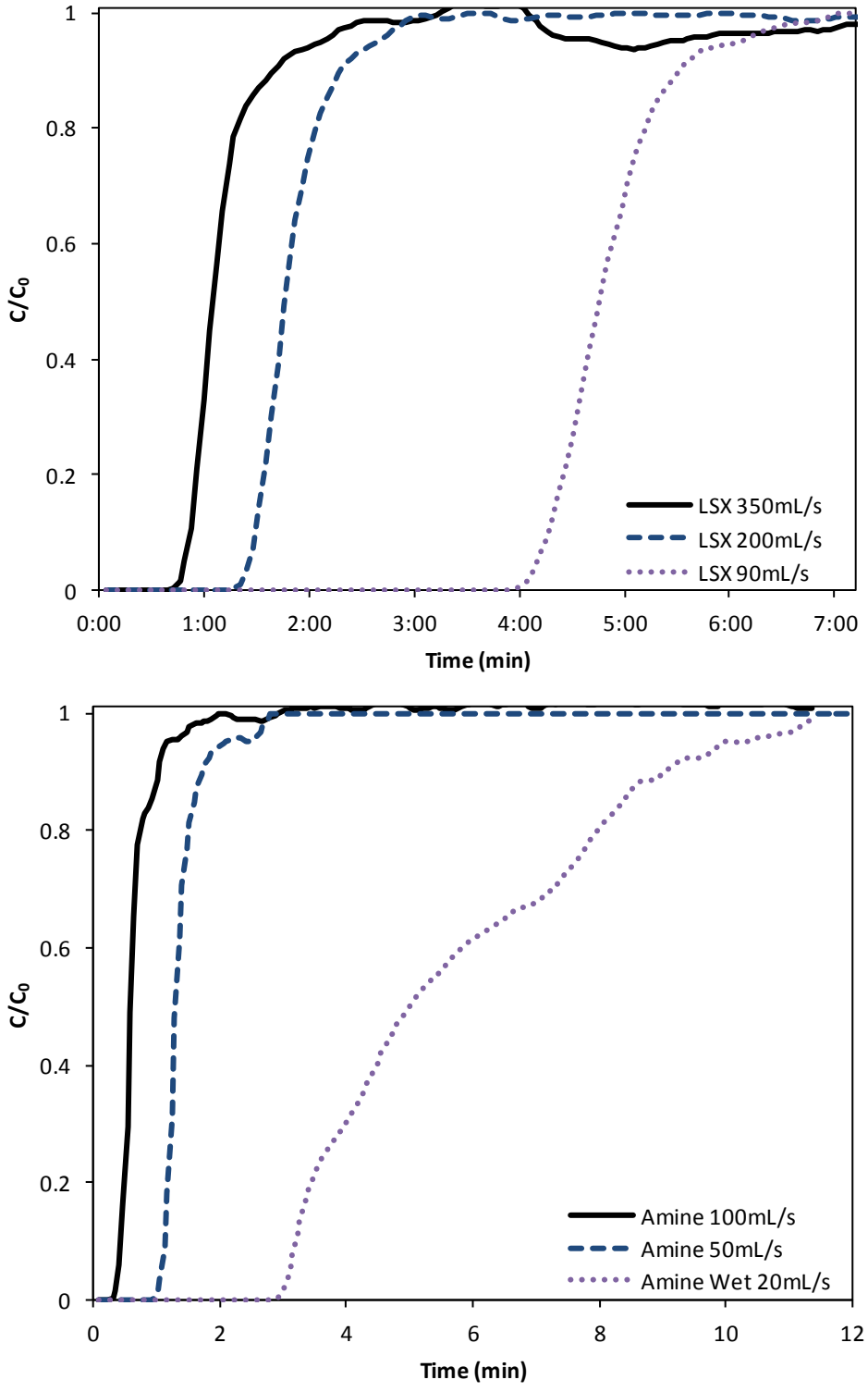

Figure 41 Breakthrough curves for flue gas conditions, obtained for K/Na (2:1) LSX and Amine grafted SBA15. Conditions were set at 25°C, 13% CO_2 and the balance N_2. For wet conditions R.H. was 80%. 0.55g of LSX was used and 0.3g of Amine grafted SBA15 was used. Obtained by Lifeng Wang.

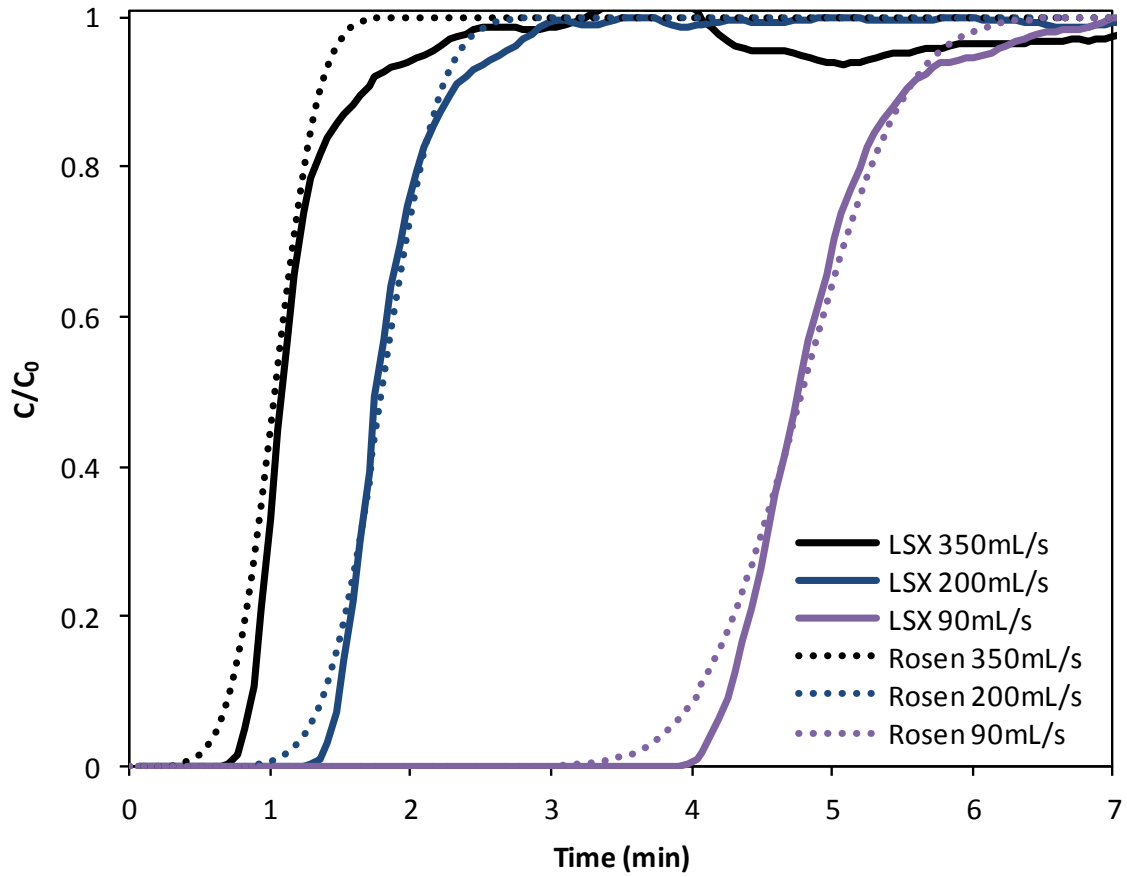

Figure 42 Rosen model fit for LSX at dry flue gas conditions. The model was fit to the average breakthrough capacity of the isotherms and all other parameters were found through independent measurements.

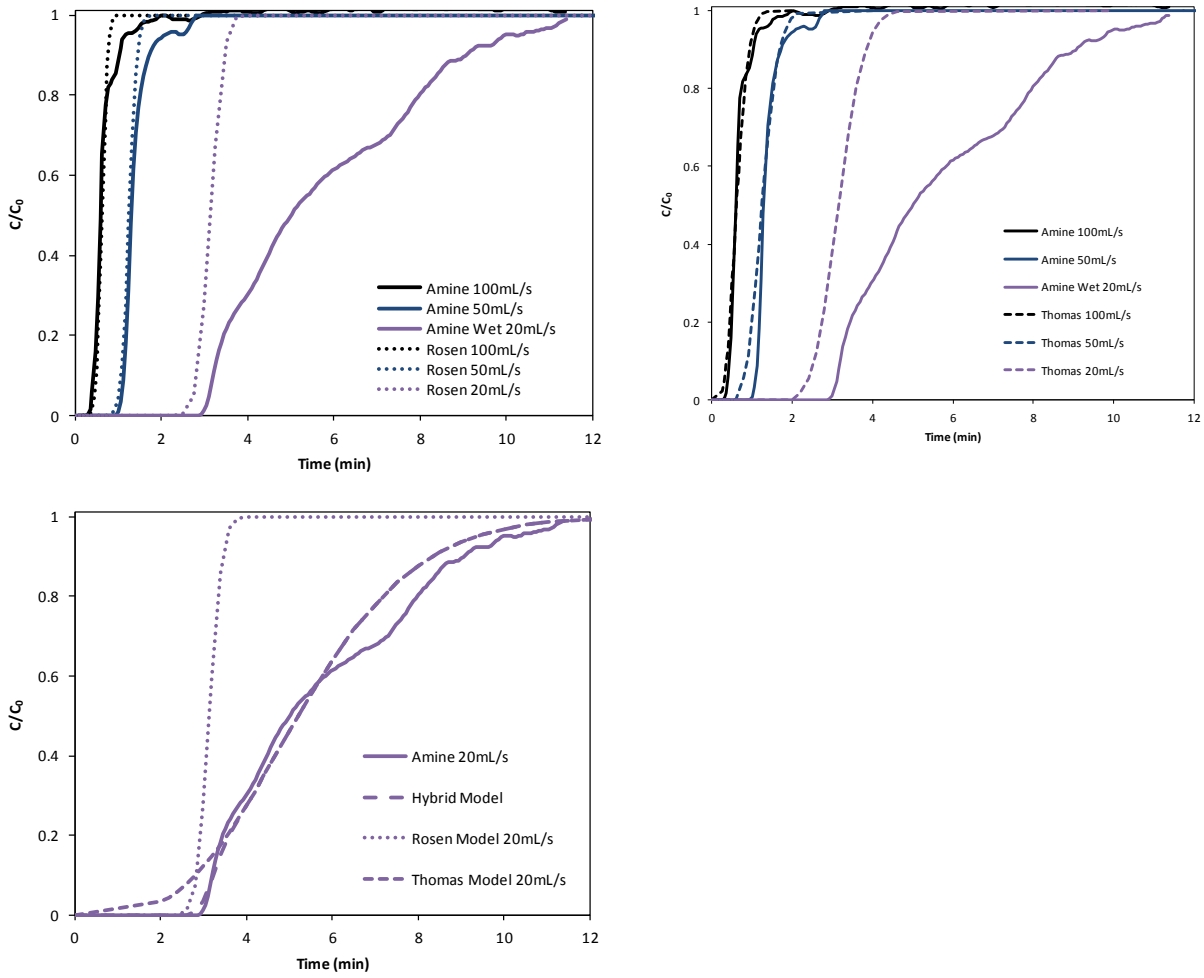

Figure 43 Modeling fit for Amine at flue gas. The models were fit to the average breakthrough capacity of the isotherms for dry conditions and separately for the wet condition. For the Rosen model, all other parameters were found through other measurements, not related to the breakthrough curves. For the Thomas model, k_1/k_2 was fit to the capacity and k_1 was changed to account for dry vs. wet conditions. Models displayed are for dry condition fits for all except the last graph which shows the fit of the Thomas model to wet conditions.

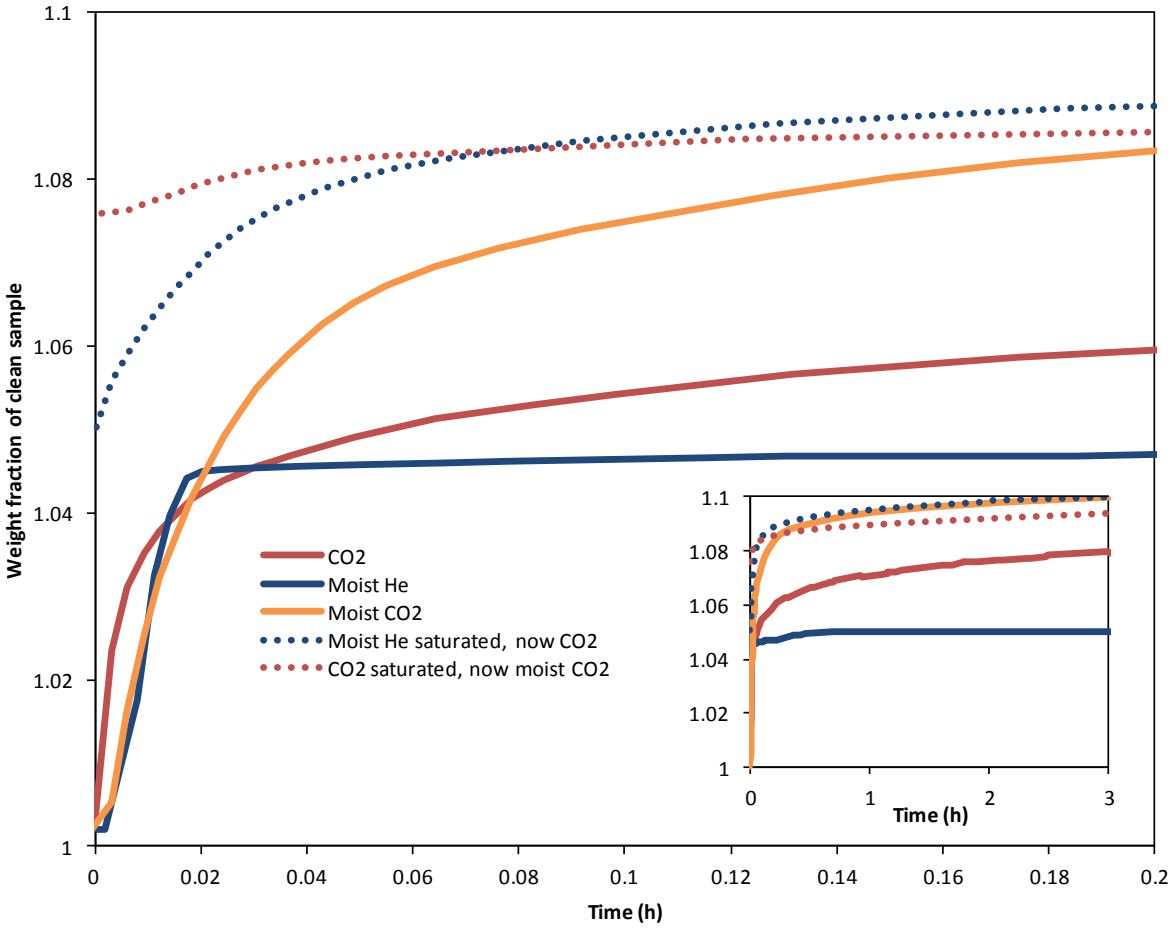

Figure 44 Rate of adsorption data for CO_2, H_2O in He and H_2O in CO_2 at 1atm. R.H. at 70% at 20 °C. Time accuracy is approximately 0.01h. Wt% accuracy is approximately 0.01wt%. Low moisture ability to retard CO_2 adsorption shows that CO_2 adsorption is likely reaction limited rather than diffusion limited.

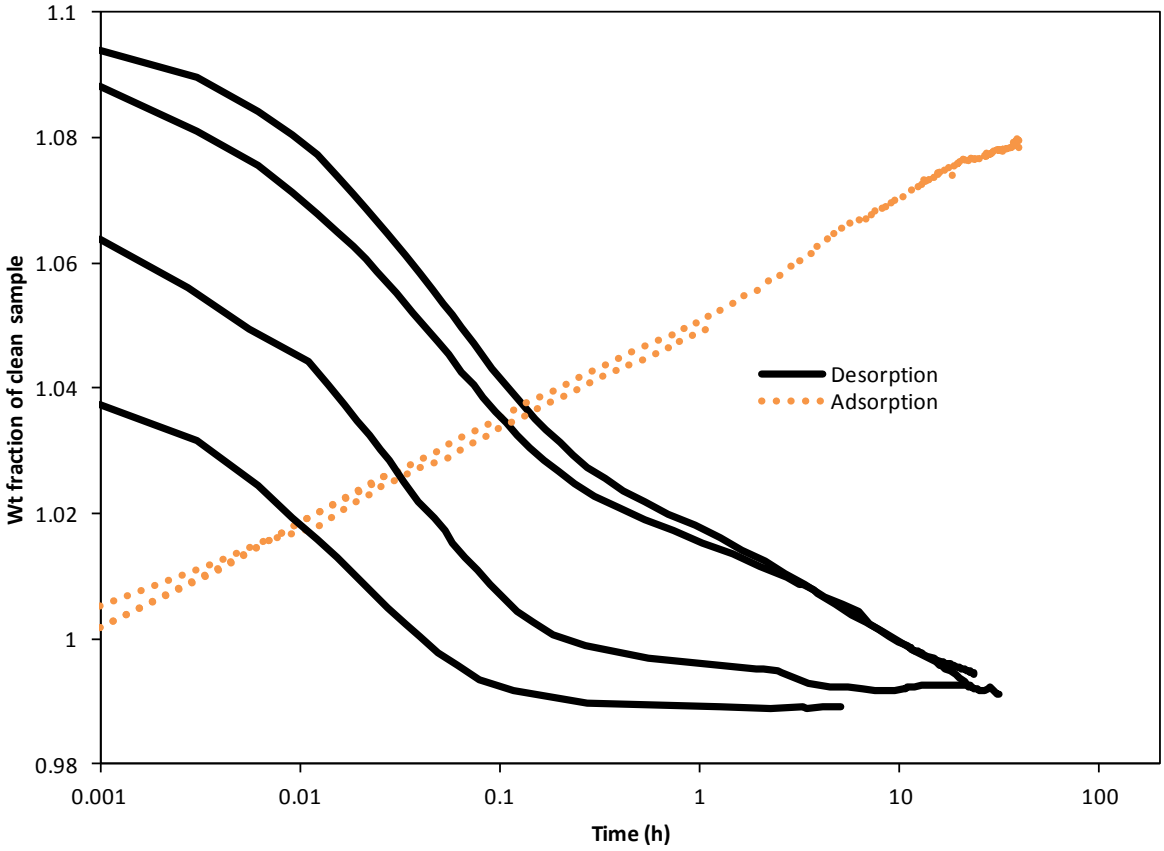

Figure 45 Adsorption rates for for dry CO_2 at 1 atm on a TGA for high capacity amine grafted SBA-15. The orange lines show the adsorption rate of amines over time. The black lines show the desorption rate from amines as changing with respect to total saturation. Time accuracy is approximately 0.01h. Wt% accuracy is approximately 0.01wt%.

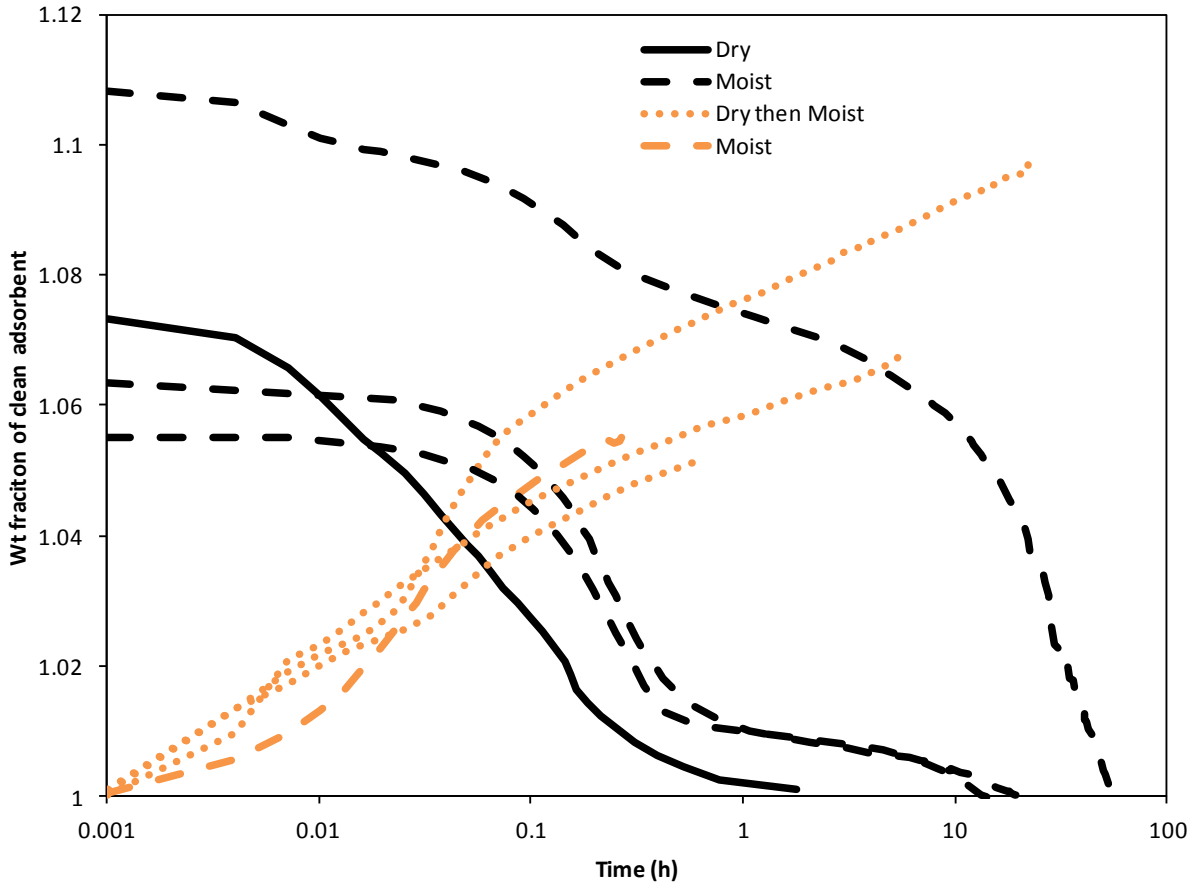

Figure 46 Adsorption rates for moist CO_2 at 1 atm on a TGA for high capacity amine grafted SBA-15. The orange lines show the adsorption rate of amines over time. The dashed orange line is for H_2O in CO_2 and the dotted orange lines show the difference when a switch from H_2O in CO_2 to pure CO_2 and back was introduced. The black lines show the desorption rate of amines as a function of total saturation. Dotted black lines for desorption indicate H_2O in He and the solid black line is for dry He only. Time accuracy is approximately 0.01h. Wt% accuracy is approximately 0.01wt%. Clean sample weight was obtained after long desorption times under moist conditions and cannot be explained at this time.

Appendix A (Supporting Information for Chapter 1)

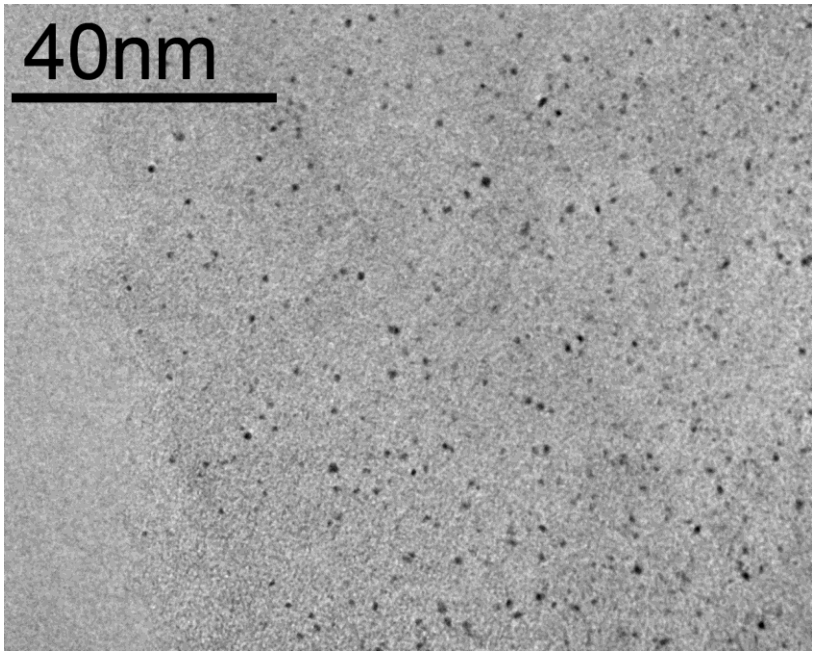

Figure 47. TEM of 6wt% Pt/AX21 using a Pt precursor addition time greater than 10 min.

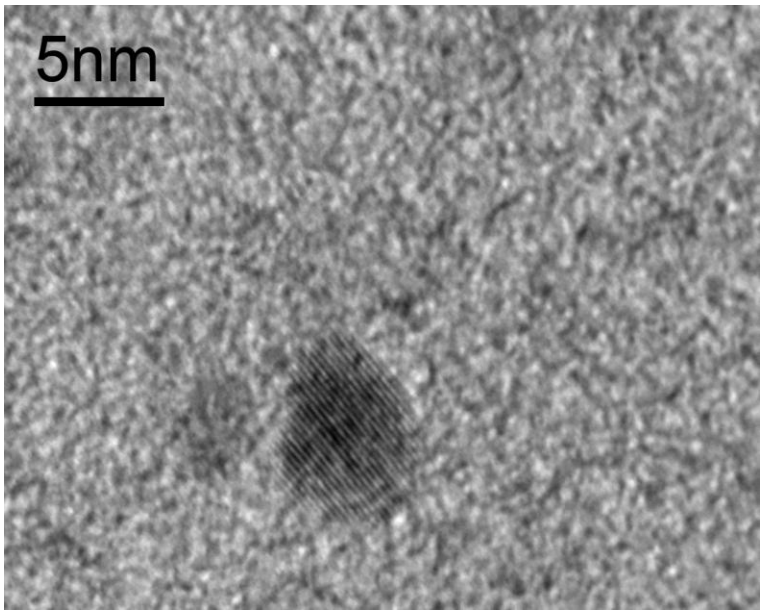

Figure 48. TEM of 6wt% Pt/AX21 using a Pt precursor addition time greater than 10 min. However, even the best samples have large aggregates.

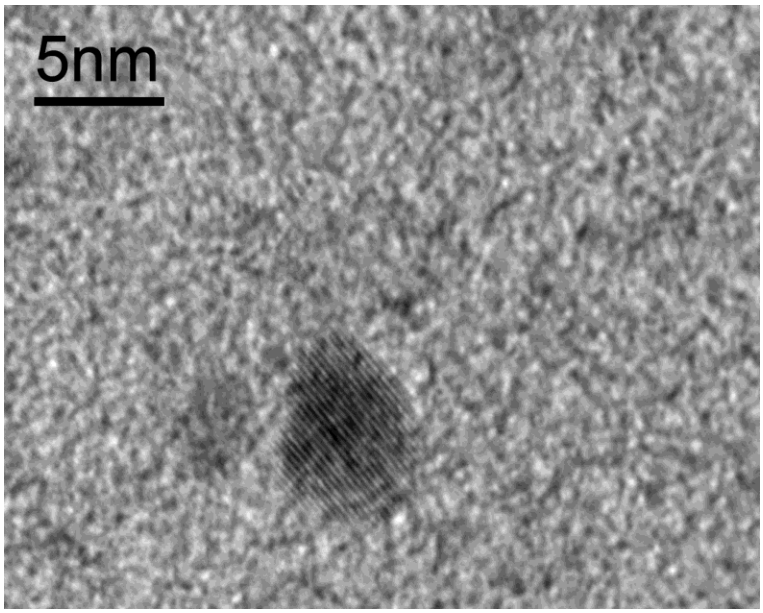

Figure 49. TEM of 6wt% Pt/AX21 using a Pt precursor addition time of 5 min. Larger nanoparticles are more present.

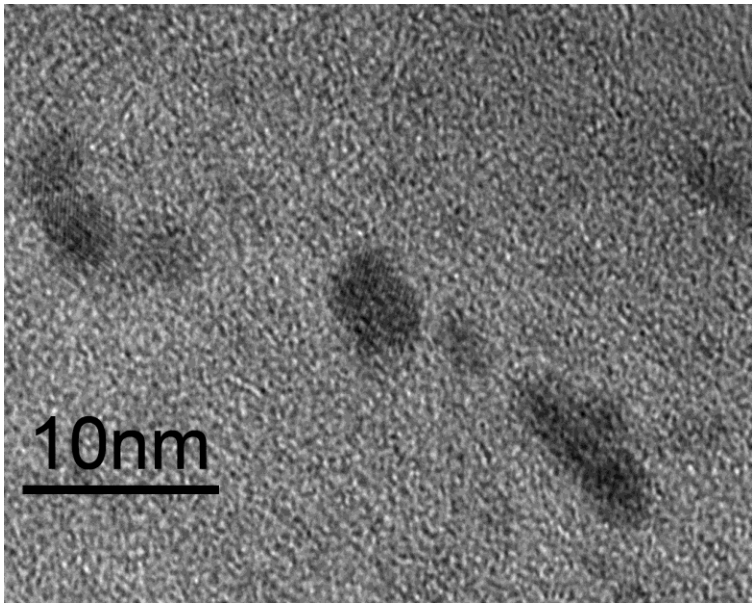

Figure 50. TEM of 6wt% Pt/AX21 using a Pt precursor addition time of 5 min.

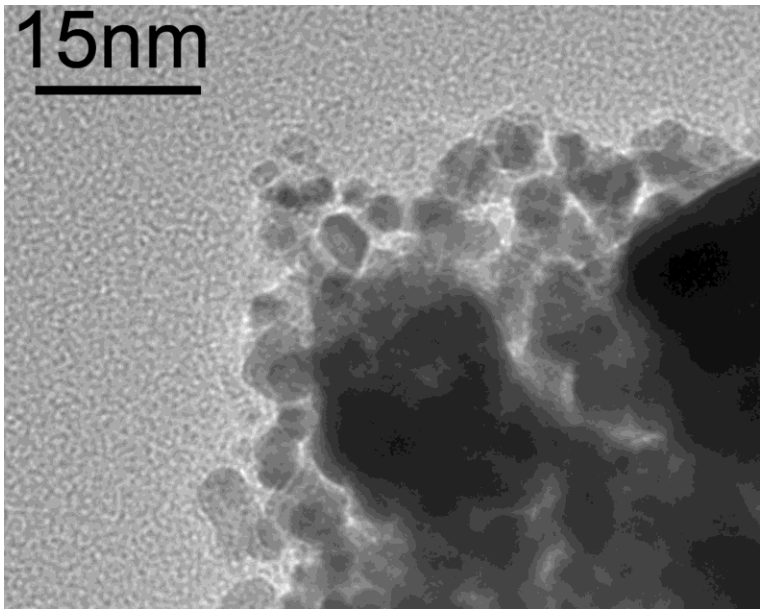

Figure 51. TEM of 6wt% Pt/AX21 using a Pt precursor addition time of 5 min. Even 5-min dosing time resulted in some very large aggregates but in a much lower amount than the fastest dosing rate.

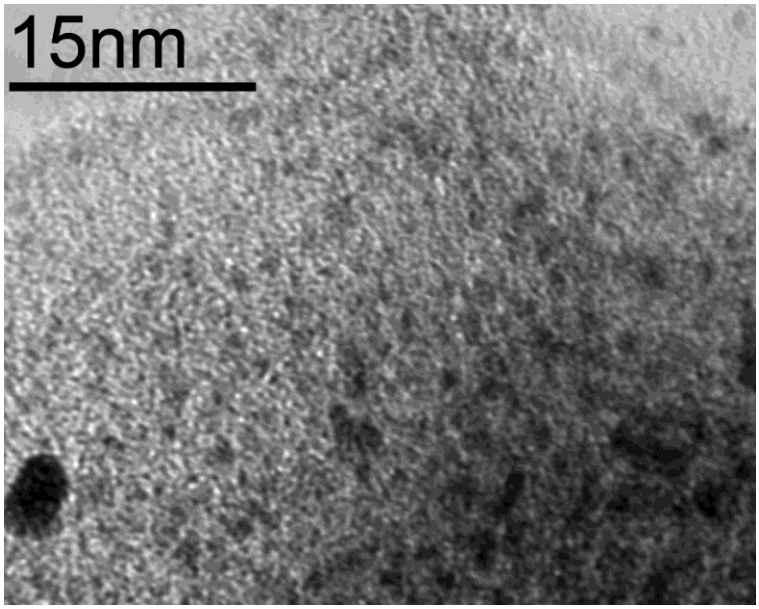

Figure 52. TEM of 6wt% Pt/AX21 using a Pt precursor addition time of 1 min. Fast addition of the Pt precursor lead to Pt aggregates on most particles and no Pt on others. However, 2-nm particles can still be found.

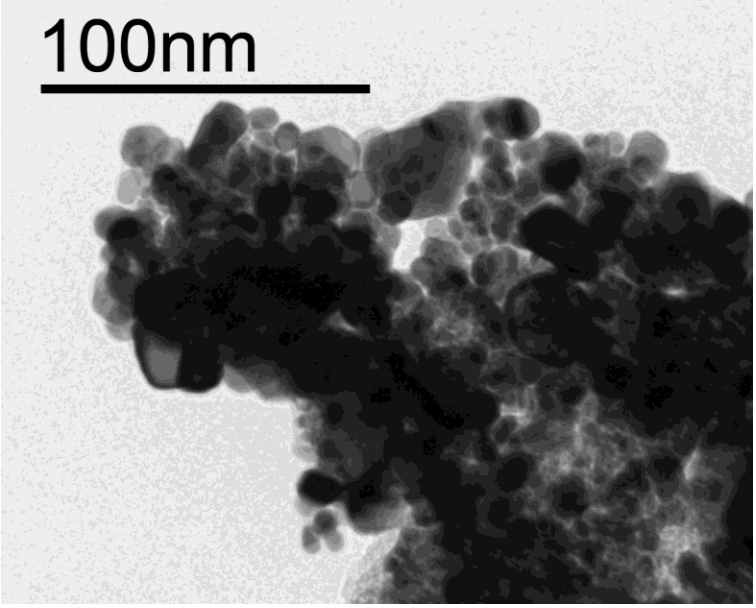

Figure 53. TEM of 6wt% Pt/AX21 using a Pt precursor addition time of 1 min. large aggregates are everywhere while many carbon particles are without Pt.

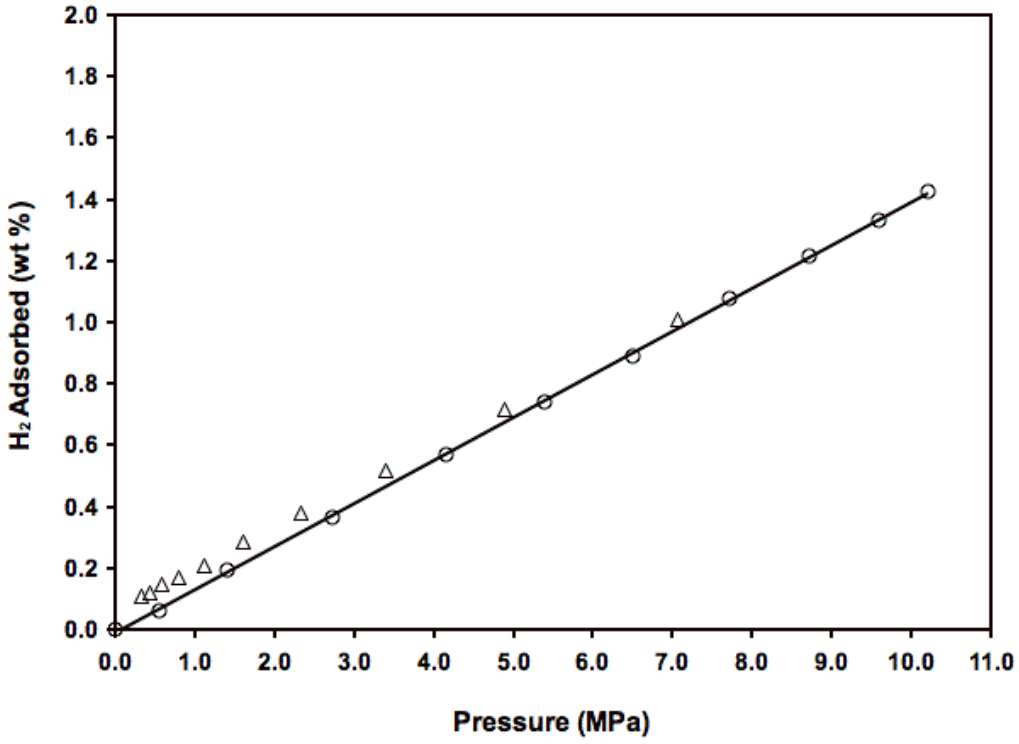

Figure 54. Adsorption/desorption isotherms for a bridged-IRMOF-8 sample. Hysteresis is shown that is known to correspond to spillover enhanced adsorbents. Obtained by Lifeng Wang.

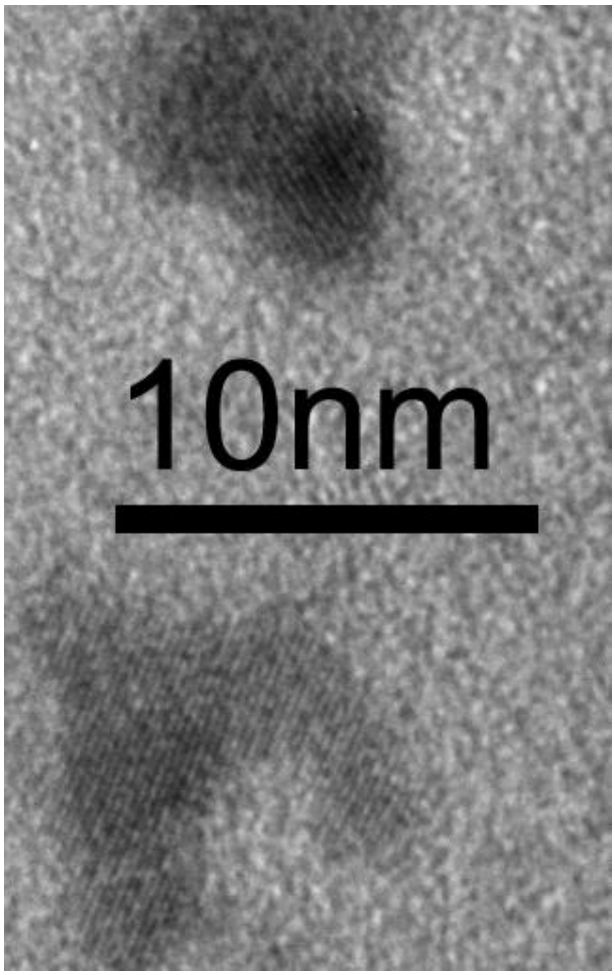

Figure 55. TEM of 6wt% Pt/AX-21 that was not fully passivated before exposure to air. Particle sintering can be clearly seen.

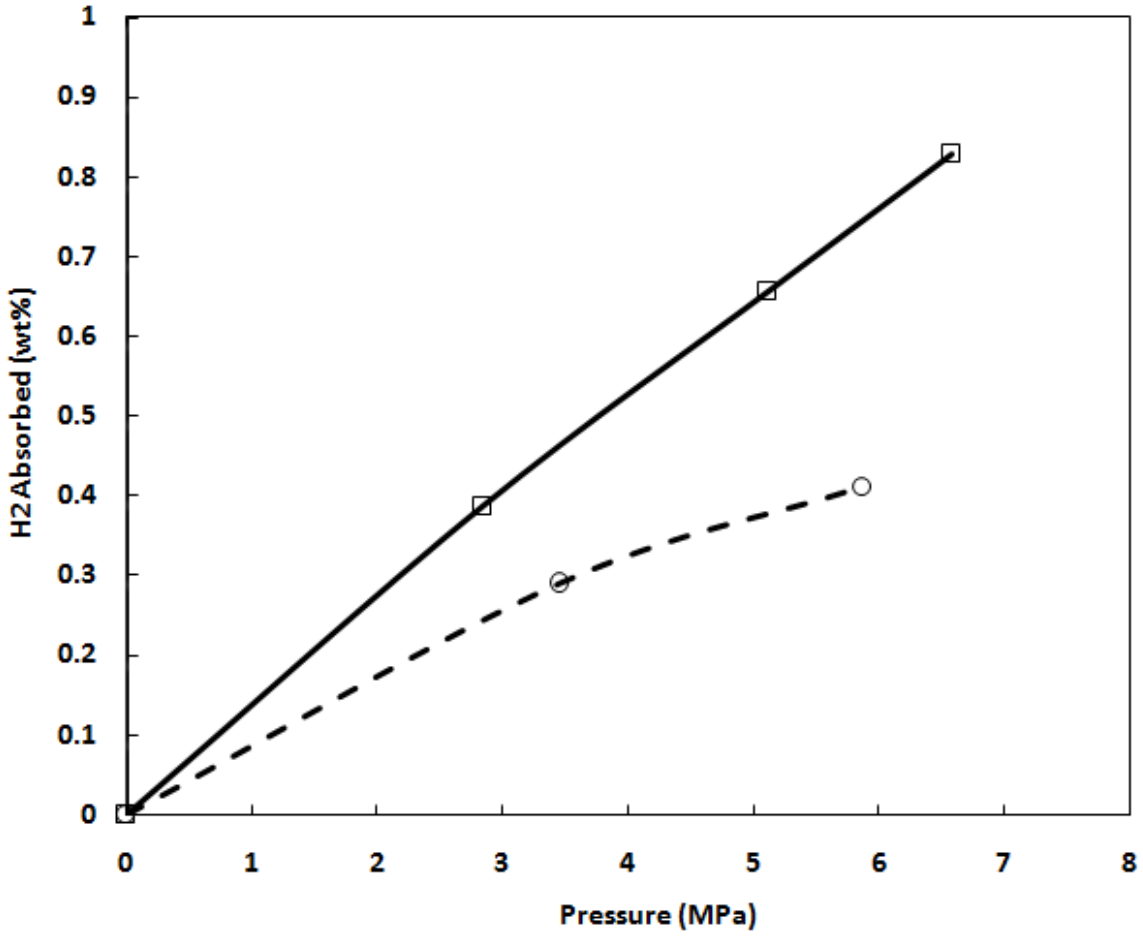

Figure 56. Passivation effect isotherms for 6wt% Pt/AX-21. (☐) fully passivated and (○) not passivated, clearly showing the loss of storage potential when the sample is not fully passivated. Obtained by Lifeng Wang.

For isotherms obtained by Lifeng Wang, it is demonstrated the same instrument used for measurements shows no statistically significant difference between metal doped materials and plain materials, but at a time approximately 4 years after these isotherms were obtained. Additionally plain materials were shown to measure significantly higher adsorption capacity than they are known to have. The cause was determined to be moisture presence in the helium source which had been in operation since 2001. The effects of moisture are already known to be significant for hydrogen adsorption and could potentially be just as significant for helium adsorption.

Appendix B (Supporting Information for Chapter 2)

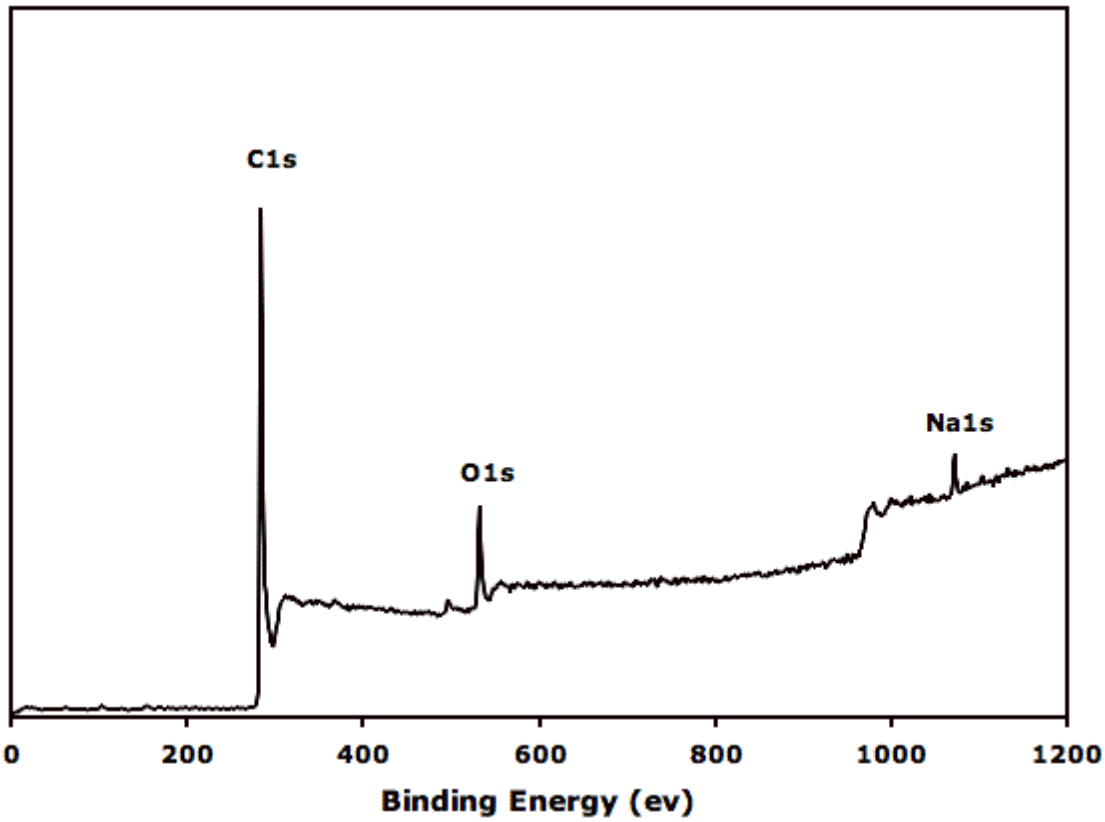

Figure 57. The XPS spectra of graphene. Obtained by Lifeng Wang.

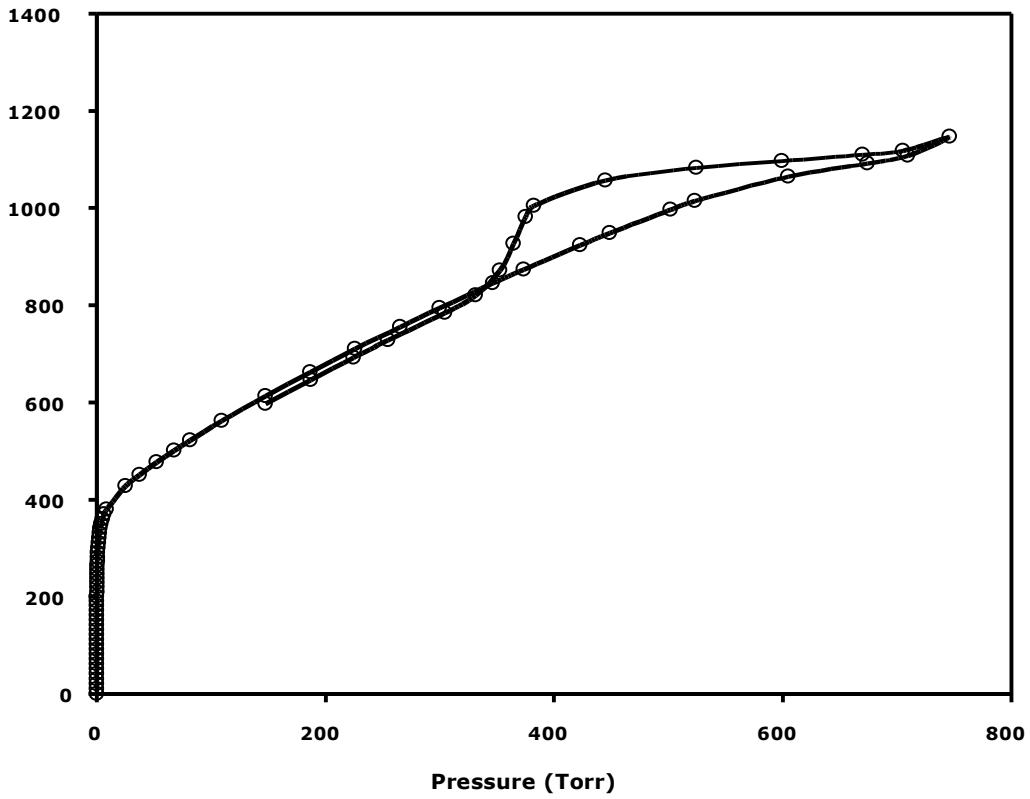

Figure 58. Nitrogen isotherm of graphene at -196 ^{o}C. Obtained by Lifeng Wang.

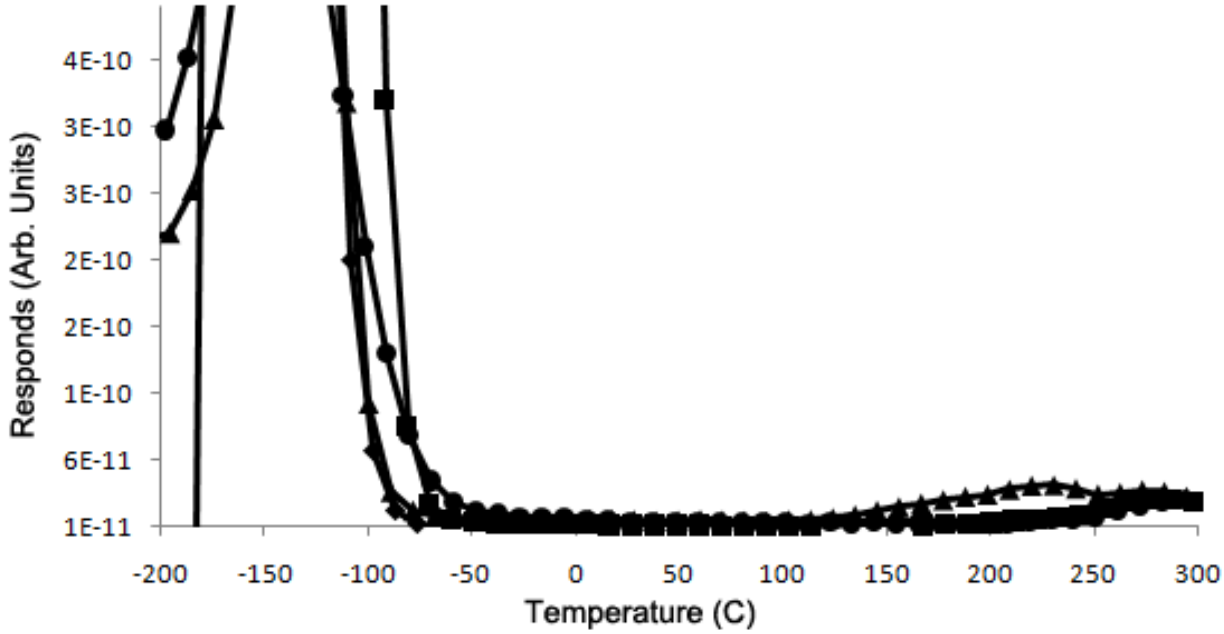

Figure 59. The TPD spectra are shown for H_2 desorption from AX-21 carbon on three separate runs. Dosing was done with only H_2 for 40 min at 25 ^{o}C at 1.6 MPa.

Additionally isotherms measured have the same issue as previously discussed, that none of the isotherms taken from the instrument in question are statistically significant, however the original raw data is not available and cannot be fully analyzed to test for significance.

Appendix C (Supporting Information for Chapter 3)

Additionally isotherms measured have the same issue as previously discussed, that none of the isotherms taken from the instrument in question are statistically significant, however the original raw data is not available and cannot be fully analyzed to test for significance.

Appendix D (Supporting Information for Chapter 4)
Materials and Methods

Reagents and Material Sources. NaY was obtained from STREM Chemicals. NaX was obtained from Sigma Aldrich. NaX pellets were obtained from UOP. Na/K LSX was obtained from Praxair. Li-LSX pellets (~1/40" diameter) were obtained from Praxair. Maxsorb was obtained from Kansai Coke and Chemicals. AX-21 was obtained from Anderson Development Co. LiCl, LiOH, NaOH, NaCl, KOH, KCl, $CaOH_2$, $Ca(NO_3)_2$ were all obtained from sigma aldrich as reagent grade.

Low silica type X zeolite had a silica to alumina ratio of 1, for X this was 1.2 and for Y this was 5.1.

Atmospheric air was compressed directly from outside to a pressure of 125 psi. Dry grade air obtained from Cryogenic Gases Inc. was used when needed, containing less than 1 ppm CO_2. Wet air was prepared via a single pass through a water bubbler and was humidified to 80% RH.

Instruments. Isothermal adsorption was measured using a Micromeritics ASAP 2020. Thermo-gravimetric analysis was done using a Shimadzu TGA-50. Breakthrough was done using a Vaisala GMP 220 with a range setting of 0-1000 ppm, a bed of 3" in length and a pressure gauge with a range from 0-45 psia. Desorption was measured using a Vacuum Technology Incorporated Magnetic Sector Mass Spectrometer.

Adsorption Rates Background. For the rates measured on the Micromeritics ASAP 2020, both the frit and trans-seal were removed before measurements. While this is not critical for analysis (as shown in SI Figure 1), it eliminates all doubt as to the rate determination of the zeolites, and lowers response time from 2 s to less than 200 ms (limited by the pressure gauge response time ~100 ms). This response was determined to be the same across the pressure range 0-0.2 atm.

Ion-Exchange of Zeolites. Ion-exchange for zeolites is the primary method for synthesis of single cation zeolites. The exchange takes place in solution where the starting ions are driven out due to higher concentrations of the new species. This equilibrium data is presented by Sherry.[SI1] Once the ions are exchanged, they penetrate the structure of the zeolite during calcination/water removal. This occurs at 200 °C for sodium and 300 °C for cesium (most difficult cation to exchanged in the D6R cage) [SI1] as demonstrated by Norby et al.[SI2] XRD spectra demonstrating preserved crystalline structure of LSX zeolites is presented in SI Figures 2-4, and a short comparison of shifted peaks demonstrating full cation exchange in SI Figure 5. All others were verified using surface area measurements.

Slurry Bed Preparation. The slurry method for the bed preparation for amine grafted SBA-15 was tested against the pellet method for breakthrough sharpness. The results are shown in SI Figure 6. Pressure drop for a flow rate of 5600/h was decreased from 1.3 psi to 0.2 psi. These clearly indicate that not only does the method provide optimal micro-pore exposure; it also decreases macro-pore diffusion resistance. Stability testing was also performed. The pressure was cycled from 1 psi to 24 psi 5 times and held at each pressure for 5 minutes. A plot of pressure vs. space velocity is shown in SI Figure 7 and clearly demonstrates the stability of this novel bed at these conditions. Images were taken of the bed which appears somewhat like swiss-cheese macroscopically and like a woven fiberglass bed at 300x magnification (SI Figure 8).

Isotherm Fitted Parameters. Shown in SI Table 2 and SI Table 3.

Freundlich equation[32]:

$$n = k\, p^{\frac{1}{t}}$$

Toth equation[46]:

$$n = \frac{ap}{[1 + (bp)^t]^{1/t}}$$

TGA Analysis. For the determination of CO_2 uptake on amines in wet conditions, I refer to other work published on the mechanism for adsorption. [SI3] Amines are known to adsorb through a reaction via two pathways. In dry conditions this is a single step, primary reaction. In wet conditions water adsorption follows second . In wet conditions, the capacity is only doubled when the second pathway is followed. This leads to adsorption slowing due to a more complex route. Thus, wet conditions must be slower or as fast as dry conditions. Variance of this reaction rate has been found for primary, secondary and tertiary amines. Here I use only unhindered primary amines. Additionally, the support only affects diffusion resistance which is not significant until high amine loading is achieved.[SI3]

Adsorption/Breakthrough Apparatus. Shown in SI Figure 9. Heating was observed for desorption at a rate of ~500 °C /min. For bed pretreatment, the heating rate was lowered to 5 °C /min. The heating wire used was 0.37mm nickel chromium wire (obtained from Omega Engineering Inc), wrapped on the inside of the quartz tube, with a spacing of ~3mm. The thermocouple was in an isolated jacket, which ran through the radial center of the bed and contacted the heating wire in the middle of length of the bed. Quartz fiberglass was used as insulation at the top and bottom of the bed, to ensure isothermal conditions of ±3 °C throughout. If the temperature of the bed is not constant, produced CO2 will be adsorbed in the cooler portion of the bed. This will result in less than expected CO2 production above 1 atm and increase the need for a final vacuum step.

TVSA Cycle Shown in SI Figures 10-13

Results and Discussion

Pure Component Isotherms. Zeolites showed the highest capacity for CO_2 and N_2 except below $2x10^{-4}$ atm. For zeolites, the adsorption capacities increased with decreasing cation diameter and increasing charge of the cation. Lower ratios of silica to alumina were shown to increase capacities as well. The cause is the increase in the number of exposed cations. The number of cations exposed for faujasite (i.e., types X and Y zeolites) starts at cation counts of around ~60 per unit cell (alumina to silica ratio of 4).[32] For reference, the zeolite X used in this study had a ratio of 1.2 (cation count of 86), the LSX had a ratio of 1.0 (cation count of 96) and the zeolite type Y had a ratio of 5.1 (cation count of 56). There are six cation sites typically populated SI, SI', SII, SII', SIII and SIII' (listed in order of increasing cation charge). Among these cation sites, only cations located at sites SII, SIII and SIII' are exposed (for adsorption, SI, SI' and SII' are never exposed). These are the cations with the largest positive charge, which is exponentially proportional to heat of adsorption. Nitrogen and CO_2 adsorb based on van der Waals forces, induced dipole moments (i.e., interaction between electric field and induced dipole) and quadrupole moments (i.e., interaction between field gradient and quadrupole). However, the ratio of the quadrupole interaction energy for nitrogen is only half the total interaction energy, while for CO_2, it accounts for almost two thirds.[32] Equation 1 shows the quadrupole interaction energy,[32] and equation 2 shows the induced dipole interaction energy.[32]

$$\phi_Q = -\frac{Qq(3cos^2\theta - 1)}{4r^3(4\pi\varepsilon_0)} \quad (1)$$

Where Q is the linear quadrupole moment of the adsorbate (-1.5 esu for N_2 and -4.3 esu for CO_2), q is the electronic charge of the ion, r is the distance between the centers of the interacting pair, θ is the angle between the field and the quadrupole moment and ε_0 is hte permittivity of a vacuum.

$$\phi_{Ind} = -\frac{\alpha q^2}{2r^4(4\pi\varepsilon_0)^2} \quad (2)$$

Where α is the polarizability (1.74 x 10^{24} cm^3/molec. for N_2 on Na-LSX and 2.91 x 10^{24} cm^3/molec. for CO_2 on Na-LSX), q is the electronic charge of the ion, r is the distance between the centers of the interacting pair and ε_0 is the permittivity of a vacuum.

From this I can predict that nitrogen binding will increase proportionally more rapidly with smaller cations and higher charges than CO_2. This is also what is observed and shown in Table 1. Unfortunately, further prediction is complicated by the change in occupied cation sites when different cations are used, even for constant Si/Al ratios. The heats of adsorption for nitrogen were as expected, almost exactly what is predicted near zero loading. The heats of adsorption for CO_2 are also close to expected at zero loading but were forced to be fitted using a Langmuir isotherm, which contributes significant error (±5 kJ/mol). At atmospheric concentrations of CO_2 , saturation effects are already observed, especially for calcium, which lowered the heat of adsorption observed at 395ppm substantially (Table 1).

Pure silica (SBA-15) was shown to have negligible adsorption capacities for both CO_2 and nitrogen, being relatively inert and non-polar. Heats of adsorption were nearly the same for both (Table 1). When grafted with amine, adsorption of CO_2 was increased greatly and nitrogen was unaffected. Low-concentration CO_2 adsorption was exceptionally high (on a per site basis), making this the most selective adsorbent studied even with the low concentrations of amine (Table 1, Figure 1 and Figure 2). Heat of adsorption for CO_2 on amine was found to be higher than all other tested adsorbents.

The two activated carbons had very low adsorption amounts of CO_2 over the entire isotherm. The only trend observed was that increasing the surface area directly increased the capacity for both CO_2 and nitrogen. However, CO_2 selectivity remained extremely low and capturing CO_2 from the atmosphere would be infeasible. Only results for the activated carbon Maxsorb are shown in SI Table 1.

Desorption Product Purity. The effect of TVSA desorption conditions on the second adsorption cycle are shown in SI Figure 14. The full desorption profile for TSA (with and without a purge) performed with Li-LSX is shown in SI Figure 15.

Cyclic Energy Balance. A basic ideal energy balance is provided for comparison to other technologies.

For CO_2, I assume an ideal gas below 1 atm partial pressure. An isentropic compressor was assumed for the adsorption process. A polytropic compressor was assumed for degas and for CO_2 recompression. A motor efficiency of 0.92 was assumed. For heating, I assume no heat loss to the environment. I assume a 1" thick bed. I assume all adsorbed CO_2 is captured.

Using data presented for pressure drop vs. space velocity, I assume a 7% pressure drop. I assume an atmospheric concentration of CO_2 of 384ppm:

4.2 kW*hr/kg CO_2

For air drying, I assume a 3A adsorbent requiring heat to 240 °C, and 20% weight capacity for moisture at 7% R.H.:

170 W*hr/kg CO_2

For degas:

7.8 W*hr/kg CO_2

For heating, I assume only CO_2 adsorbed (heat of adsorption and heat capacity) and the bed itself need to be accounted for:

2.1 kW*hr/kg CO_2

For CO_2 recompression, I assume all CO_2 adsorbed is recompressed from 0.1 atm to 1 atm:

130 W*hr/kg CO_2

Total energy requirement: 6.6 kW*hr/kg CO_2

	Maxsorb	SBA15	Amine
CO_2 Capacity 395ppm (mmol/g)	0.002	0	0.14
N_2 Capacity 0.8atm (mmol/g)	0.55	0.042	0
CO_2 heat of adsorption 390ppm (-kJ/mol)	5	6	65
CO_2 heat of adsorption zero loading (-kJ/mol)	5	6	65
N_2 heat of adsorption 0.8 atm (-kJ/mol)	15	19	N/A

Table 3. Table showing isotherm values for measured materials.

Adsorbent	Temperature	Freundlich t	Freundlich k	Toth a	Toth b	Toth n
Amine grafted SBA-15	273	0.963646	0.0013617	0.0017686	0.0010311	0.0652835
Ca-LSX	273	2.20584	1.58202	0.796543	0.170586	0.375494
Ca-Y	273	1.83775	0.211026	0.106017	0.135995	0.315187
K-LSX	273	1.06512	0.0178343	0.0137277	0.001109	0.69498
Li-LSX	273	1.55781	0.0884891	0.0253487	0.0128294	0.69069
Na-LSX	273	1.09825	0.0092234	0.0062441	0.0011876	0.746314
Na-LSX	273	1.09027	0.028438	0.0200653	0.001252	0.741707
Na-Y	273	1.0753	0.0166507	0.0121977	0.0012747	0.681236
SBA-15	273	1.02883	0.004475	0.0039745	0.0010376	0.541728
Li-LSX	298	1.35294	0.171966	0.0586348	0.0029782	0.841225

Amine grafted SBA-15	298	0.940261	0.0009034	0.0013769	0.0009919	0.0751448
Ca-LSX	298	1.9172	0.789013	0.320905	0.0975	0.433382
Ca-Y	298	1.59169	0.085792	0.0509997	0.112575	0.286511
K-LSX	298	0.998004	0.0098367	0.0103294	0.0009981	0.464486
Maxsorb	298	1.15027	0.0351844	0.0216321	0.0102005	0.433382
Na-LSX	298	1.04657	0.0128082	0.0109464	0.0011385	0.69069
Na-LSX	298	1.07072	0.014008	0.0105141	0.0011241	0.6996
NaX	298	1.08254	0.0034817	0.0024738	0.0011241	0.716688
Na-Y	298	1.0617	0.0102518	0.0086347	0.0066916	0.390044
SBA-15	298	0.953593	0.0024535	0.0034062	0.0009773	0.0633164
Li-LSX	373	0.983095	0.0009507	0.0010825	0.001018	0.0836445
Amine grafted SBA-15	373	0.947639	0.0002661	0.0003849	0.0010376	0.0704375
Ca-LSX	373	1.29059	0.0483821	0.0431042	0.0825125	0.22321
Ca-Y	373	1.13385	0.0038015	0.0022954	0.00179	0.746314
K-LSX	373	1.59917	0.036117	0.0229345	0.125203	0.253647
Na-LSX	373			0.0059247	0.0033843	0.45056
Na-Y	373	1.01279	0.002595	0.0024357	0.0012889	0.144955
SBA-15	373			0.0007348	0.0009454	0.0240902

Table 4. Table showing fitted parameters for pure component N_2 isotherms. Some isotherms could not converge to parameter fitting and have been excluded.

Adsorbent	Temperature	Freundlich t	Freundlich k	Toth a	Toth b	Toth n
Amine grafted SBA-15	273	3.57784	5.42567	2.19117	0.263199	0.396355
Ca-LSX	273	5.29097	40.0029	34.0775	0.454807	0.569631
Ca-Y	273	3.11896	6.85425	1.57884	0.176013	0.366828
K-LSX	273	6.58173	41.6311	43.1337	0.570491	0.681236
Li-LSX	273	6.67714	10.0477	11.8471	0.630687	0.6636
Na-LSX	273	4.34296	24.8281	28.3018	0.481352	0.534198
NaX	273	4.89173	34.4757	19.0165	0.332209	0.548416
Na-Y	273	3.08275	14.5596	7.67441	0.228096	0.4864
SBA-15	273	1.18705	0.0880468	0.0905699	0.0644	0.156513
Amine grafted SBA-15	298	3.36916	3.73853	1.82955	0.284342	0.375465
AX-21	298	1.31674	0.267544	0.332838	0.11758	0.176404
Ca-LSX	298	4.43523	27.9845	21.5805	0.396583	0.5056
Ca-Y	298	2.98177	4.24607	1.72285	0.226653	0.379724
K-LSX	298	5.39479	6.63213	9.54817	0.637841	0.60102
Li-LSX	298	5.74564	40.3101	32.8394	0.464038	0.58968
Maxsorb	298	1.23567	0.230687	0.100043	0.0015437	0.868725
Na-LSX	298	4.13203	20.0831	27.1856	0.522428	0.495444
Na-LSX	298	4.08516	19.9272	28.1815	0.535005	0.480816
NaX	298	3.74992	20.7038	18.5017	0.364952	0.53088
NaX	298	3.90964	10.8949	9.02479	0.36053	0.530712
NaX	298	3.73139	9.43088	4.91257	0.260029	0.527395

NaX	298	4.55528	12.7579	8.80907	0.371531	0.51516
NaX	298	4.28563	4.49331	3.36325	0.371531	0.51824
Na-Y	298	2.65472	9.19613	1.60793	0.0370944	0.751216
SBA-15	298	1.17306	0.0816044	0.109393	0.0774131	0.141967
SBA-15	298	1.16601	0.0649399	0.0877103	0.0751216	0.138253
Amine grafted SBA-15	343	2.31259	0.755191	0.405658	0.203424	0.337559
Ca-LSX	373	3.06524	8.01795	3.67303	0.230683	0.427392
Ca-Y	373	2.58965	1.38423	0.704908	0.215006	0.381995
K-LSX	373	2.71487	6.15061	3.13338	0.203426	0.450558
Li-LSX	373	2.79516	1.3608	0.697438	0.215006	0.442042
Na-LSX	373	2.5019	3.09609	1.46504	0.201917	0.366828
NaX	373	2.43764	2.21776	0.928164	0.169574	0.40448
Na-Y	373	1.42282	0.360448	0.111317	0.0083115	0.67298

Table 5. Table showing fitted parameters for pure component CO_2 isotherms. Some isotherms could not converge to parameter fitting and have been excluded.

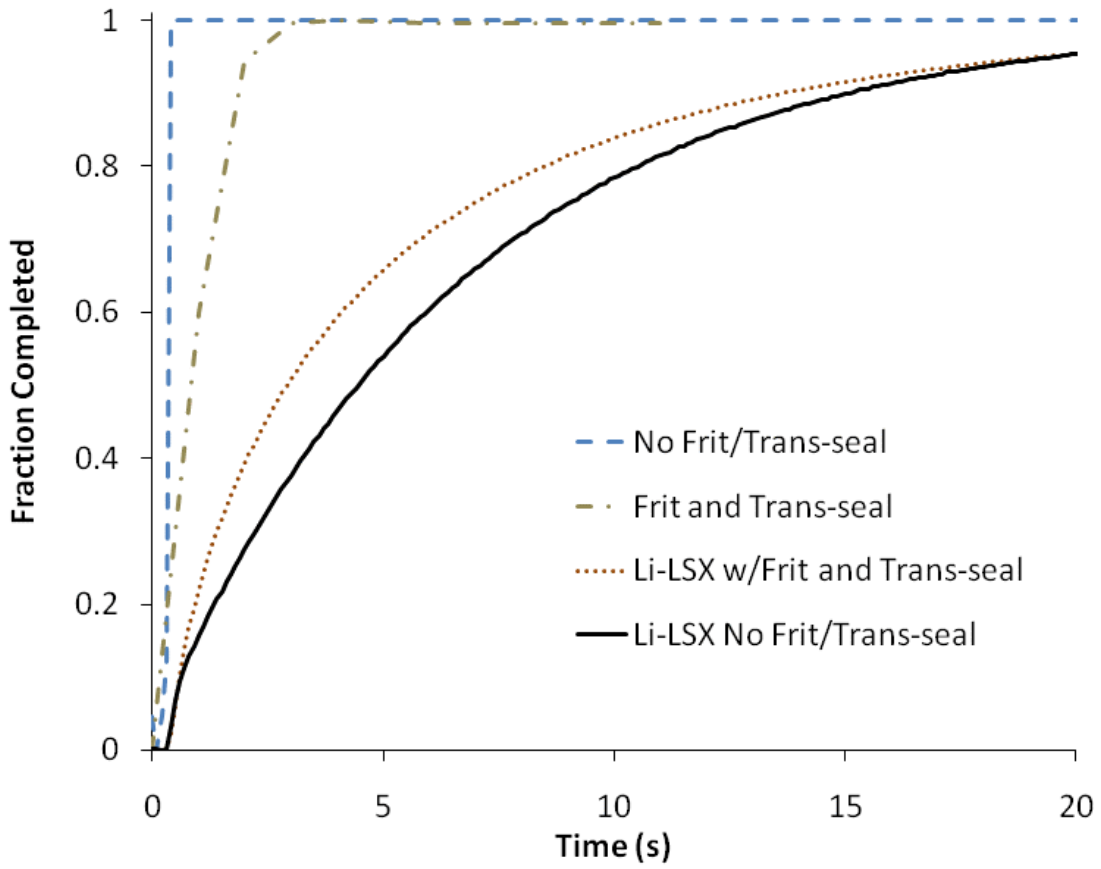

*Figure 60: Effect of frit and trans-seal of measurement of rates of adsorption on zeolite Li-LSX. *Li-LSX without the frit and the trans-seal was not immersed in a water bath. However, this still clearly shows that the frit and trans-seal do not slow adsorption.*

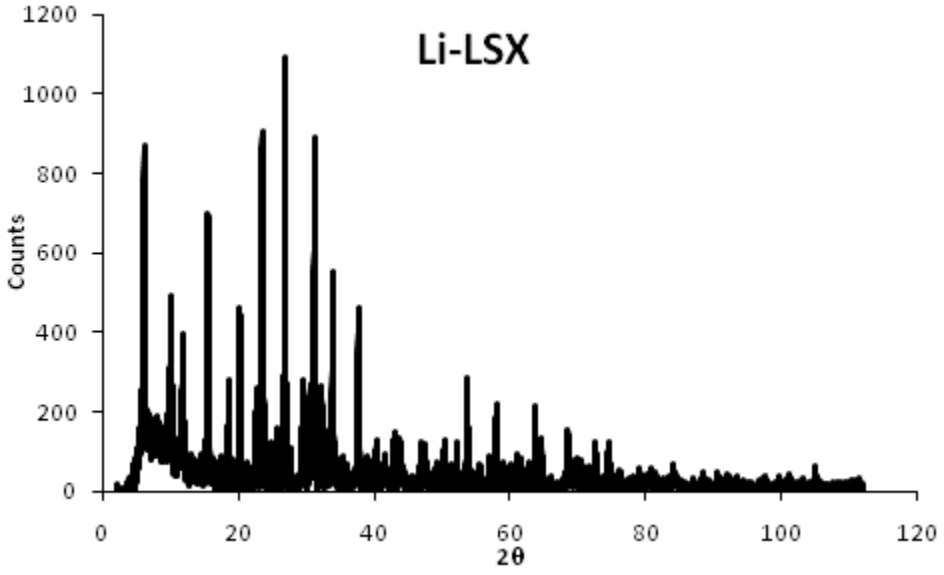

Figure 61. XRD spectra of Li-LSX taken at scan of 1°/min.

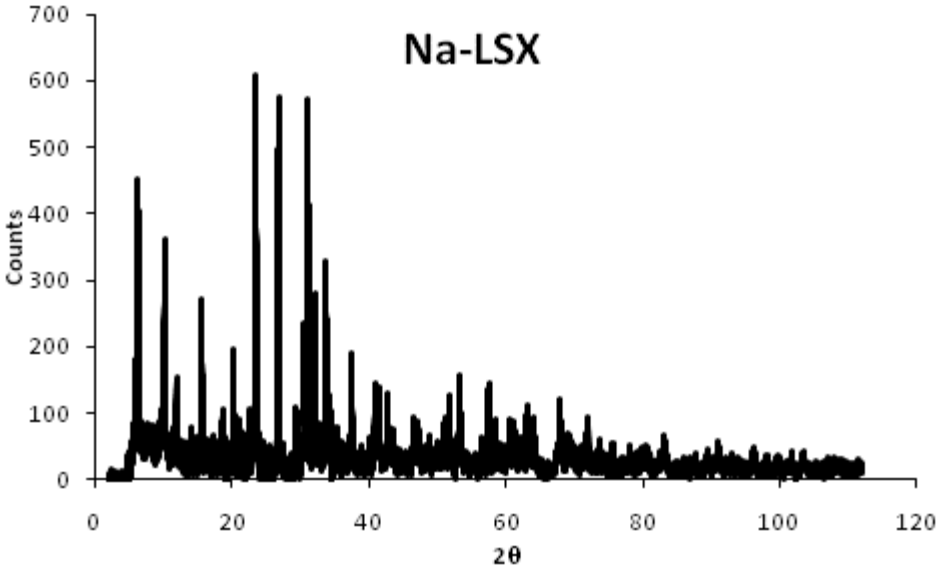

Figure 62. XRD spectra of Na-LSX taken at scan of 1°/min.

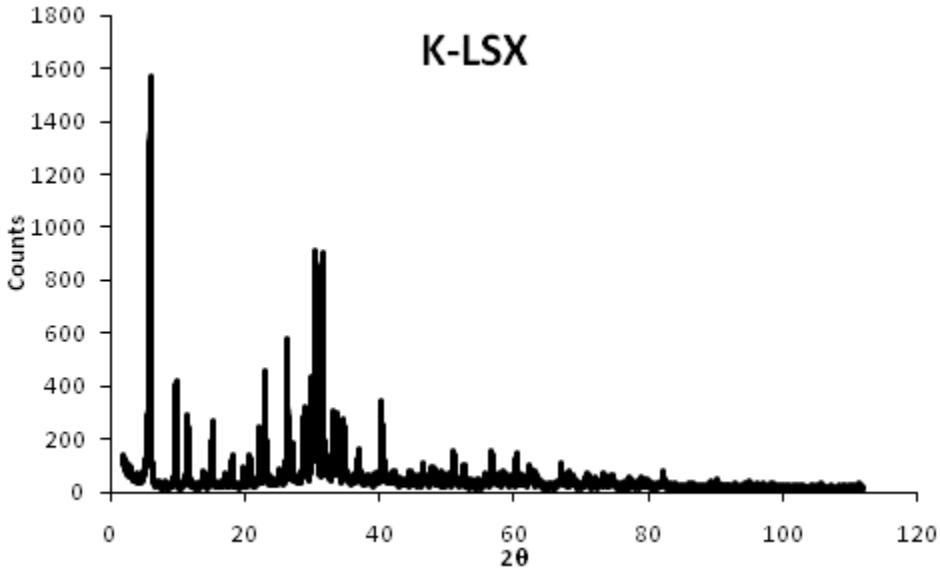

Figure 63. XRD spectra of K-LSX taken at scan of 1°/min.

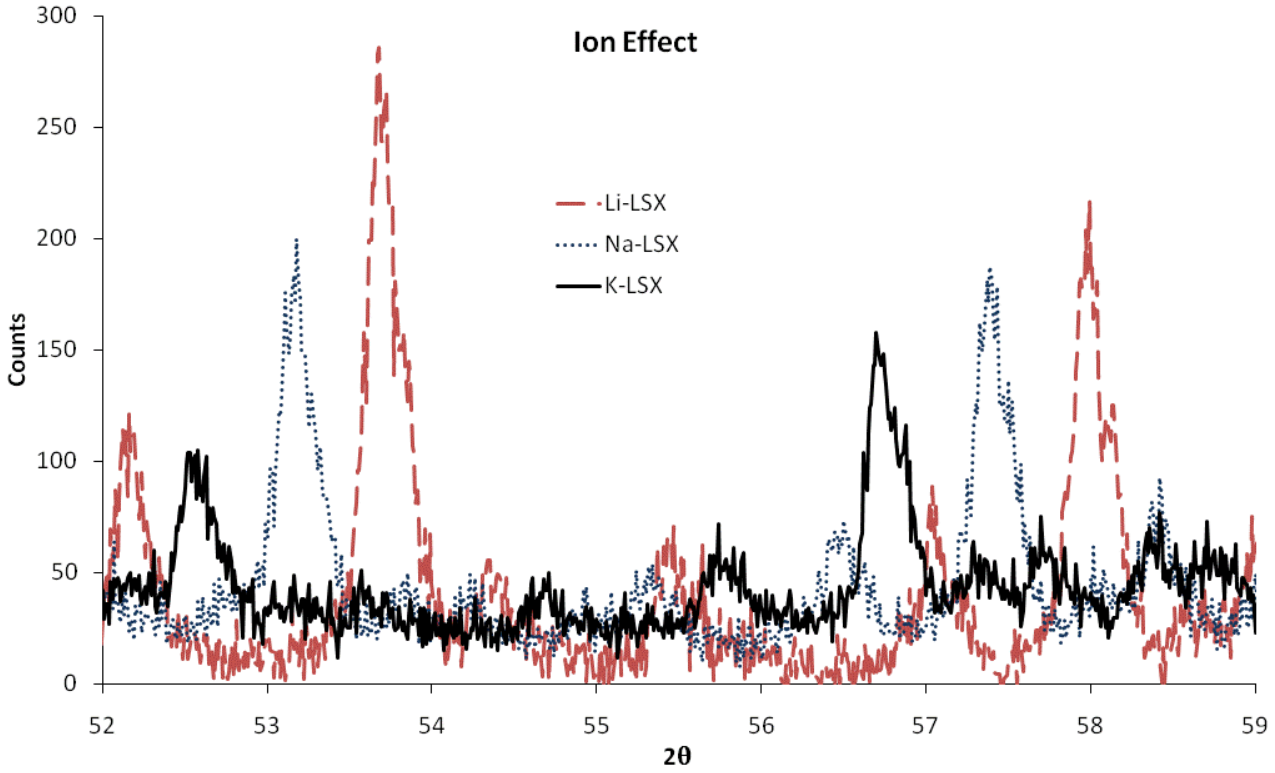

Figure 64. XRD spectra comparison of Li-LSX, Na-LSX and K-LSX.

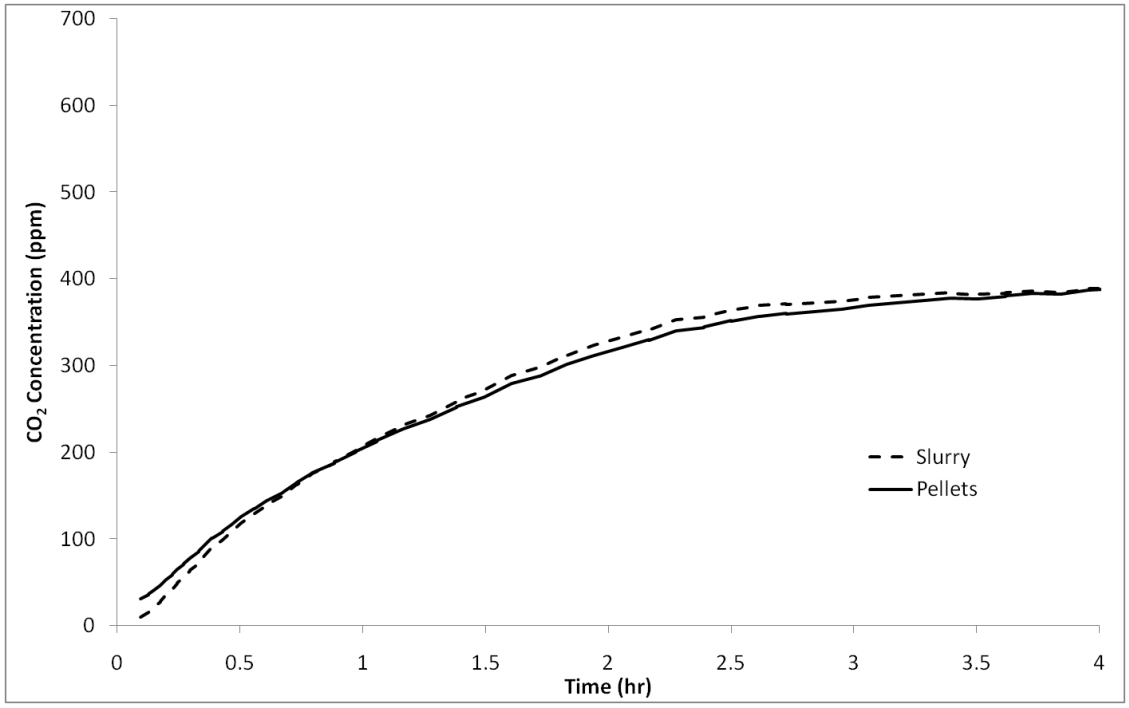

Figure 65. Showing the break-through performance of the novel slurry bed preparation method vs. pellets compacted at 200 atm (20 MPa).

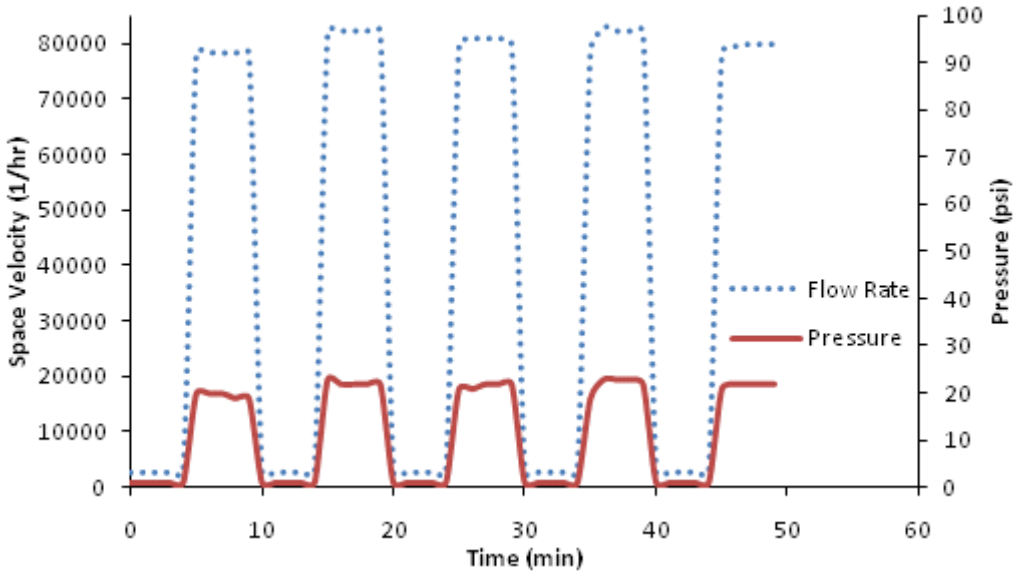

Figure 66. Showing the stability of the novel slurry bed preparation method for silica.

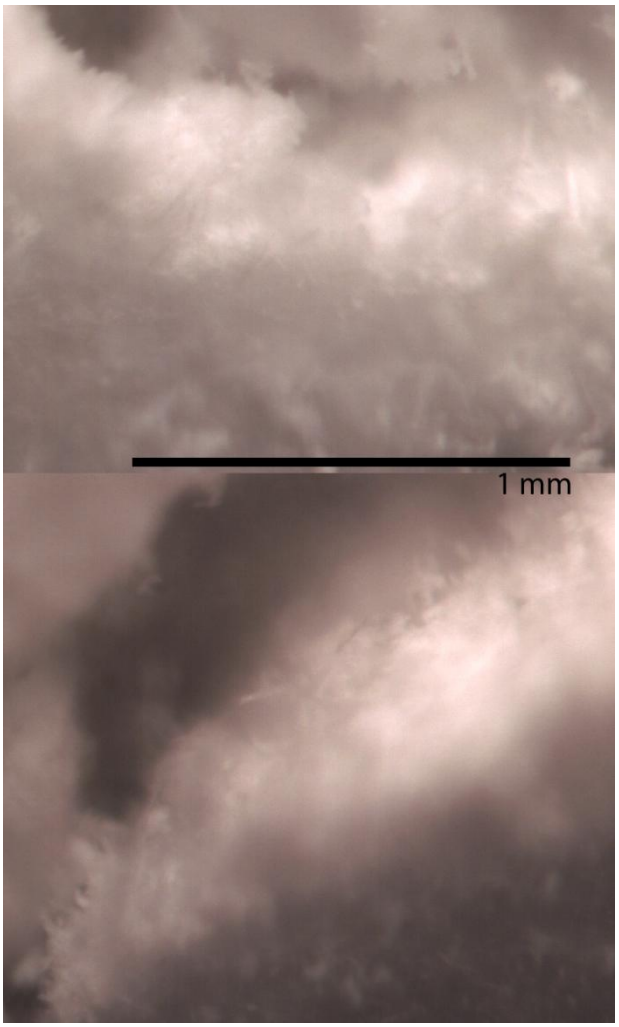

Figure 67. 300x magnification of the slurry bed.

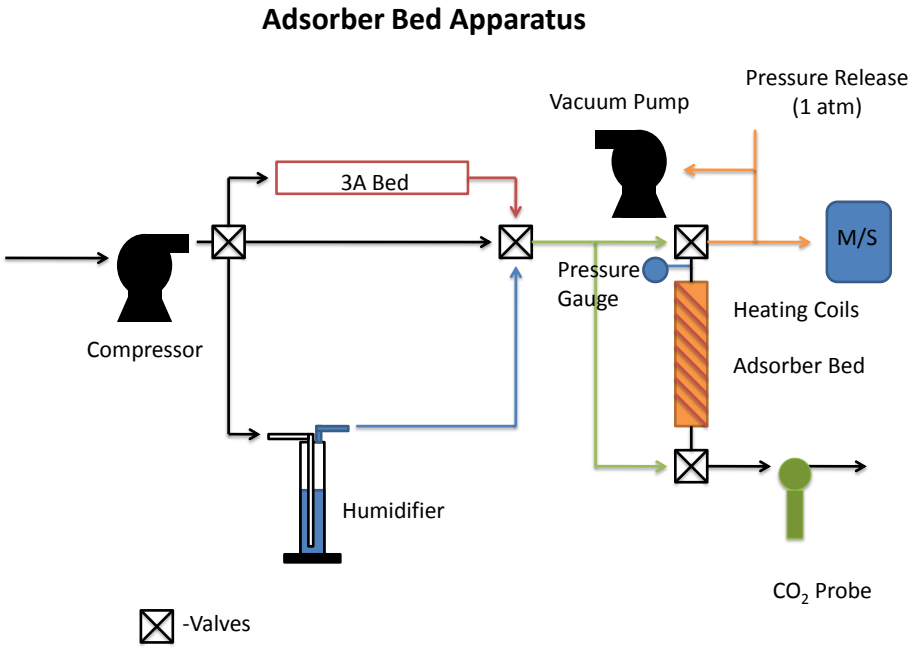

Figure 68. Showing the adsorption and desorption cycle apparatus. Heating coils were on the inside of the adsorber bed as discussed earlier.

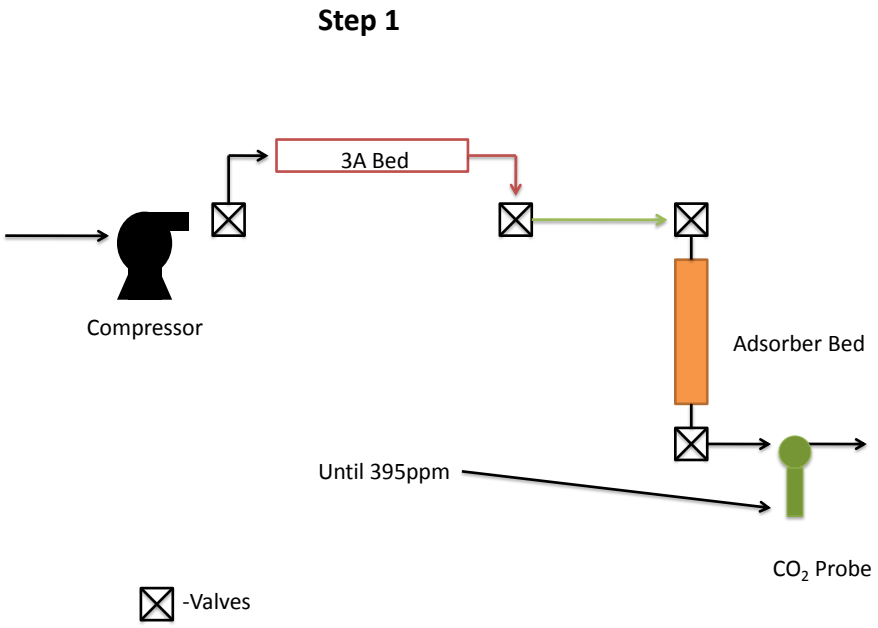

Figure 69. Step one of the TVSA cycle, showing the adsorption step.

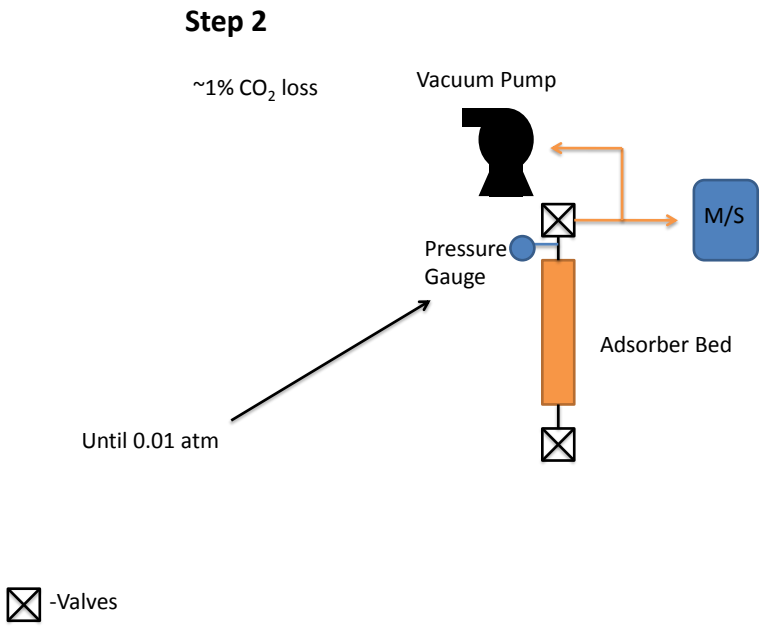

Figure 70. Step two of the TVSA cycle, showing the first desorption step. This consists of drawing down the pressure in the adsorber bed to 0.01 atm at room temperature.

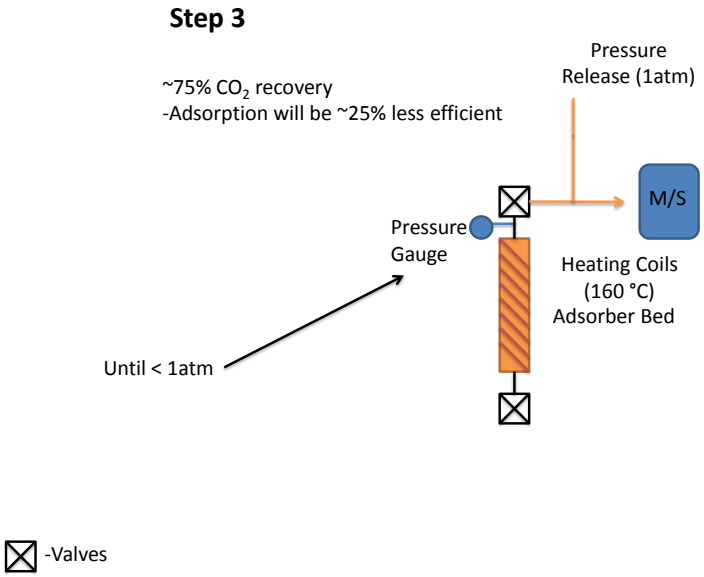

Figure 71. Step three of the TVSA cycle, showing the second desorption step. This consists of heating the bed to 160 °C, and waiting for all gas to naturally release at 1 atm.

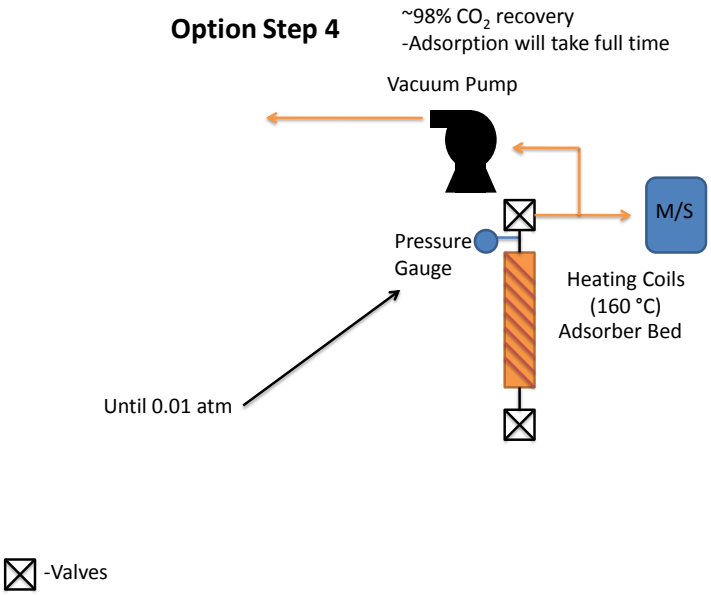

Figure 72. Optional step four of the TVSA cycle, showing the potential third desorption step. This consists of keeping the bed at 160 °C, and drawing down the gas to 0.01 atm. Drawn out gas can be recompressed.

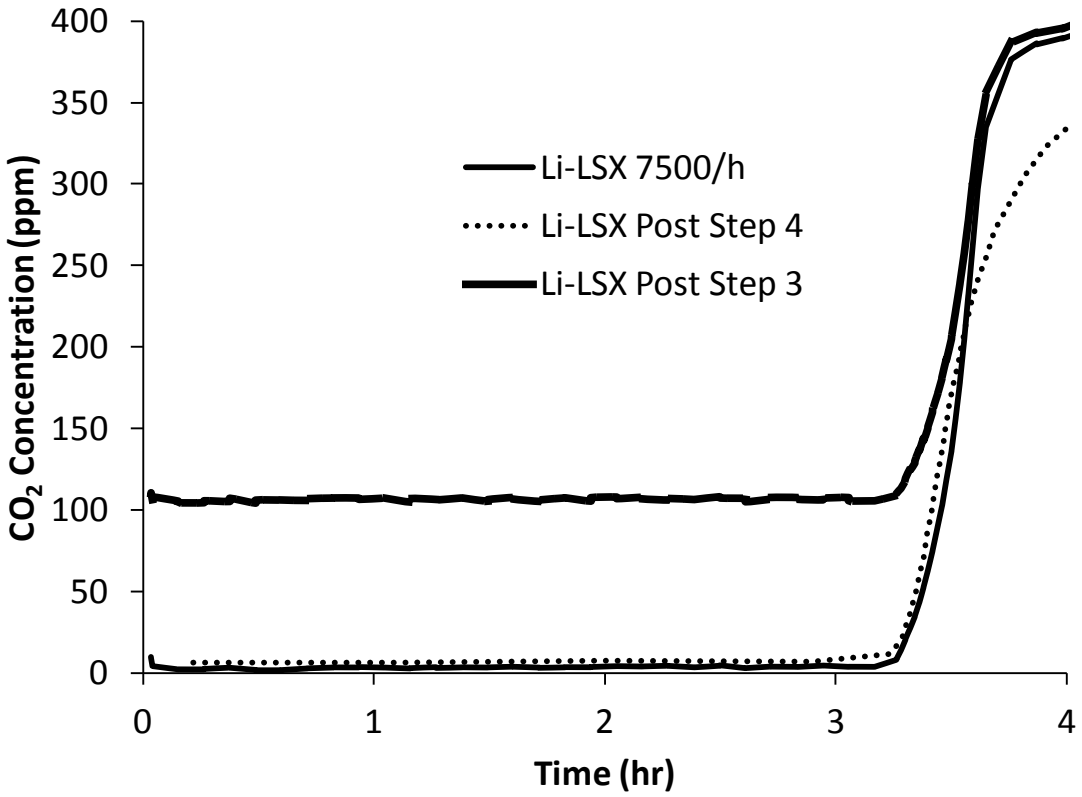

Figure 73. Breakthrough curves at GHSV of 7500/h for Li-LSX showing the effect of the optional fourth step in the TVSA process.

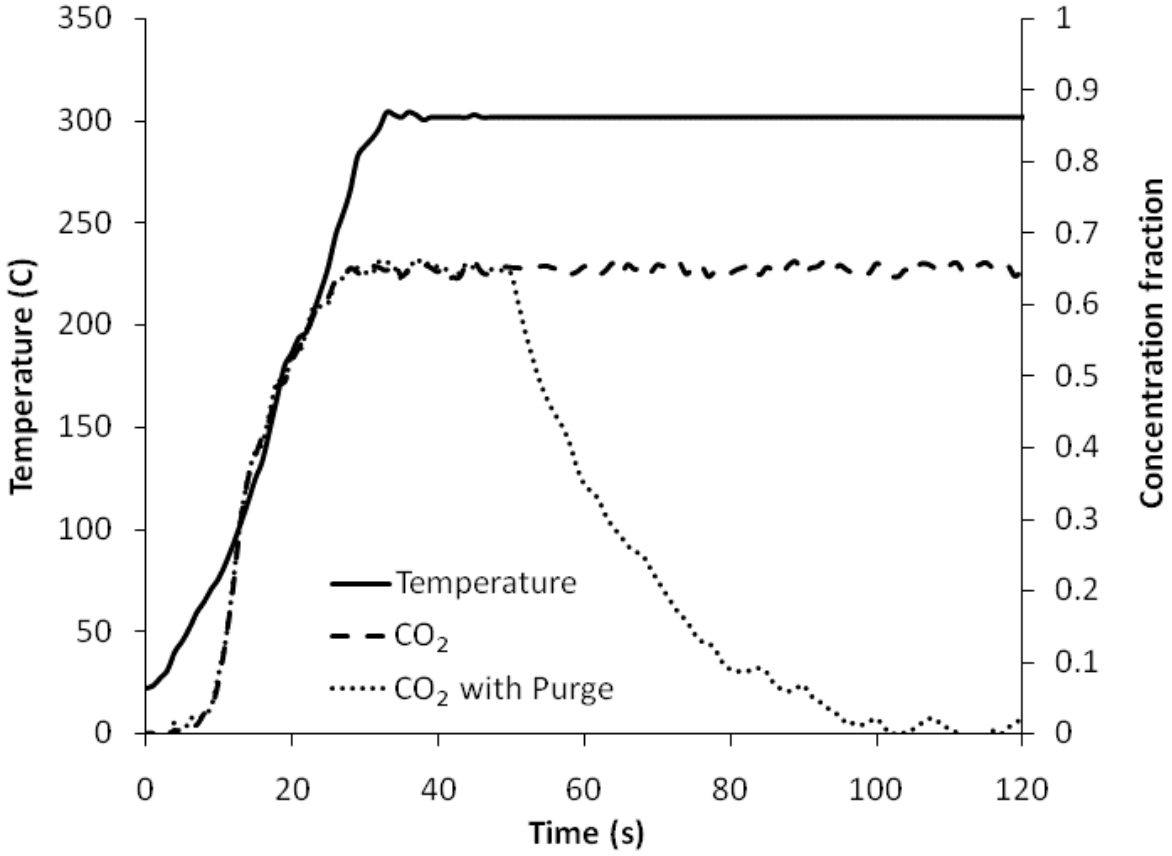

Figure 74: Desorption half-cycle using a single step temperature swing to 240 °C for Li-LSX.

References

SI 1. Sherry, H. The Ion-Exchange Properties of Zeolites. I. Univalent Ion Exchange in Synthetic Faujasite *J. Phys. Chem.*, **1966**, 70 (4), 1158. **DOI:** 10.1021/j100876a031

SI 2. Norby, P.; Poshni, F.I.; Grey, C.P.; Gualtieri, A.F.; Hanson, J.C. Cation migration in zeolites; a combined in-situ synchrotron X-ray powder diffraction and MAS NMR investigation of dehydration of zeolite Cs(Na)-Y. *J. Phys. Chem. B*. **1998**, 102, 839.

SI 3. Vaidya, P. D.; Kenig, E. Y. CO2-Alkanolamine Reaction Kinetics: A Review of Recent Studies. *Chem. Eng. Tech*. **2007**, 30(11), 1467.